Università degli Studi di Ferrara

DOTTORATO DI RICERCA IN
"SCIENZE DELL'INGEGNERIA"

CICLO XXII

COORDINATORE Prof. Trillo Stefano

BEAM AXIAL LOAD IDENTIFICATION USING ONE VIBRATION MODE SHAPE

Settore Scientifico Disciplinare ICAR/09

Dottorando	**Tutori**
Dott. Rebecchi Giovanni	Prof. Tullini Nerio Prof. Laudiero Ferdinando

Anni 2007/2009

Contents

Introduction

Axial load identification of frame members may be required to support restoration project and safety assessments of a structure, or to ascertain how far the structure is to buckling. In the last decades, various methods have been proposed for the experimental evaluation of the axial load acting in structural members, such as tie beams of arches and vaults, stay cables of suspended structures or truss structure elements. Moreover, static and dynamic approaches have been formulated to evaluate critical compressive axial forces and flexural stiffness of end constraints.

In particular, tie-rods beams were often used in ancient monumental masonry buildings to eliminate the lateral load exercised by vaults and arches. As a consequence of foundation settlements, the tensile force on tie-rods can surpass the relatively low yield strength offered by the old-time metallurgy. Also corrosion can play a decisive role in decreasing the strength of ancient tie-rods. For these reasons, it is important to identify the tensile forces in tie-rods of masonry building, especially in the case of evident deformations of arcs and vaults (Bruschi et al. 2004, Candela et al. 2004, Amabili et al. 2010). For the evaluation of tensile forces static and dynamic methods have been proposed.

Static methods make use of displacements and deformations of tie-beams subjected to one or more concentrated loads. For instance, in Briccoli Bati, Puccetti and Tonietti (2002) and in Briccoli Bati and Tonietti (2001) a static force is applied at mid-span and displacements, as well as axial deformations at the two opposite sides of the cross-section, are evaluated at three selected locations giving rise to nine distinct measurements; hence, a unique solution for the tensile force and the bending moments at the end sections is obtained.

In dynamic methods, vice versa, resort is made to vibration tests making use of beam model parameters. In Blasi and Sorace (1994) and in Sorace (1996), an approximate method is proposed, using both static deflections and vibration frequencies to evaluate axial forces in tie-beams. Making use of the first three modal frequencies, a numerical method was suggested (in Lagomarsino and Calderini 2005), which is based on a minimization procedure of a proper error function; hence, the tensile force and the beam bending stiffness are obtained. Making use of a FE model, a weighted least-squares estimation method was presented in Livingston et al. (1995), which alternatively uses the two or three lowest frequencies, or the two lowest frequencies with their corresponding (normalized) mode shapes. Moreover, to determine both plane- and space-frame forces, sensitivity-based methods are used in Park et al. (2006), Greening and Lieven (2003), Bahra and Greening (2006, 2011). An example of multiple identification of axial load patterns using vibration data can be found in Bahra and Greening (2006, 2011). However, these methods make use of finite element formulations coupled with model updating techniques, for which nonuniqueness of estimated parameters may arise.

In Tullini and Laudiero (2008), it is proposed an identification method based on the Euler–Bernoulli beam model in which geometric and elastic properties are assumed as known parameters. Making use of any natural frequency and of three displacement components of the corresponding mode shape, it is shown that both axial loads and stiffness of end flexural springs of a beam subjected to tensile or compression forces can easily be obtained. As for compression resultants, knowledge of flexural constraint stiffness implies that critical loads can analytically be evaluated and compared with actual compression forces so as to give an experimental evaluation of the safety factor. An identification technique which takes into account a more general model is given in Amabili et al. (2010). This technique is based on a frequency-based identification method that allows to minimize the measurement error. In particular, the method makes use of the Timoshenko beam theory and accounts for shear deformations and rotary inertia. Non-uniform rod section is considered since this is often the case for hand-made tie-rods in old buildings. The part of the tie-rod inserted into the masonry wall is also modeled and a simple support is assumed at the extremities in the interior of the walls. The constraints given by the masonry are assumed to be elastic foundations. The unknowns are given by the tensile force and the foundation stiffness. Nonetheless, even in this method nonuniqueness of estimated parameters may arise.

The experimental evaluation of critical compressive forces of beams with unknown boundary conditions was widely investigated as well. In Lurie (1952) reduction of natural frequencies as the value of the compressive force increases is adopted as the ruling parameter and the critical axial load is estimated by assuming a linear relation between the axial load and the square of the natural frequencies. As a matter of fact, approximate formulas of this type need an a-priori estimate of the end constraint stiffness and are quite accurate for known boundary conditions only (Shaker 1975, Plaut and Virgin 1990, Virgin and Plaut 1993). In Baruch (1973), Segall and Baruch (1980) the vibration mode shapes are used to give a kernel approximation for the integral formulation of the (column) elastic stability problem. In Go et al. (1997), the vibration mode shapes are used to formulate a FE model for the critical load estimation. In these last three papers, knowledge of end constraint stiffness is not required; vice versa, in Klein (1957), Jacobson and Wenner (1968), Sweet et al. (1976) stiffness of end constraints of a prismatic column subjected to null axial load are determined first and, then, the critical load is analytically derived. Kjell and Johnson (2009) proposed a method to measure axial forces in rail by means of forced vibration. The longitudinal load in rail caused by thermal expansion must be regularly monitored in order to avoid buckling or rail fracture. The method has the advantage of being independent of the boundary conditions, but requires very accurate measurements, advanced finite element calculations, and sophisticated data analysis.

Due to its flexibility, a stay cable is subjected to pure tension, which provides stability to the overall structure. As a result of their load-carrying efficiency, cable structures are used for many applications, such as: radio towers, power lines, ski lifts and cable bridges. When used as tension members, the cables may take the form of catenary or a simple vertical alignment. As long as dynamic loads do not create large cable displacements, the tension level does not change its magnitude along the cable length. Since vertical cables do not have the complex problem of geometric nonlinearity, the tension correlation for these systems is straightforward. Assuming hinged boundary conditions, the taut string model is employed (Chen and Petro 2005) and the axial force is derived from the knowledge of the first vibration frequency. As for axial tension identification, microwave interferometry has recently emerged as an innovative technology, suitable to the non-contact vibration monitoring of large structures. Indeed, in Gentile (2010) the radar technique is employed to identify the natural frequencies (and the cable tension) and a comparison with the corresponding quantities obtained by using more conventional techniques is proposed. The advantage of this technique is the accuracy and the simplicity of use provided by the microwave remote sensing, as well as its effectiveness in the simultaneous measurement of the dynamic response of all the stay cables under examination. However, alternatively conducted vibration measurements have shown that, due to improper identification of natural frequencies or to the use of over-simple force–frequency relationships, the accuracies achieved sometimes are not very accurate. For instance, in the presence of short cables subjected to high tensile forces, errors up to ±10% can be obtained. The effects of bending stiffness, cable sag and boundary conditions on natural frequencies, are considered in Geier et al. (2006), Kim and Park (2007), Ceballos and Prato (2008), Ren et al. (2008).

Two axial load identification methods are proposed in this work: the first one makes use of static tests and the second one is based on vibration measurement.

The latter is a generalization of the identification algorithm for beams on rigid supports derived in Tullini and Laudiero (2008). It can be applied to any slender structural member, regardless of knowledge of length and boundary conditions. This model adopts the Euler–Bernoulli model and assumes cross section geometry and elastic properties as known constant parameters whereas rotary inertia is neglected. Making use of any natural frequency and of five displacement components of the corresponding mode shape, it is shown that the axial load of a beam either in tension or in compression can be obtained with high accuracy. In fact, validation of this technique was obtained by laboratory tests. Moreover a new formulation of the limit curves derived in Tullini e Laudiero (2008) to bound the admissible data domain is given.

Static procedures are restricted to supported beams and consists in the measure of the displacements of three instrumented sections located at the quarters of the beam and at mid span, due to the application of a transversal static force. Similar to the transcendental equation of the dynamic procedure, an equation irrespective of boundary conditions is obtained, together with other two equations for the evaluation of the flexural end stiffness. Laboratory tests were performed to validate the analytical results.

In particular, in Chapter 1 some fundamental principles necessary to introduce the governing equations are recalled. Moreover, concepts about the dynamic substructuring with finite elements are illustrated, and a brief review of finite element approach by means of dynamic stiffness matrix is given (Leung 1993).

Chapter 2 deals with different kind of condensation method. Firstly, static condensation and Guyan's reduction methods are introduced (Guyan 1964, Hatch 2001); then, the exact dynamic condensation method (Leung 1978) and some examples utilized in Chapter 3 and 4 are illustrated. It is shown that, in order to study the dynamic behaviour of a generic substructure, suitable stiffness condensation matrix is to be assigned to re-establish the global behaviour of the structure without loss of information.

The first part of Chapter 3 runs through the procedure developed by Tullini and Laudiero (2008) again. The new formulation of the admissible data domain has been validated by laboratory tests. The dynamic stiffness matrices of the boundary conditions for different sets of frame configurations have been derived. In the second part of Chapter 3, a new static method for the axial load identification of a slender beam on rigid supports is presented. It is shown that, if bending stiffness and mass per unit length of a beam with constant cross section are known, the axial force and the flexural stiffness of the end constraints can be deduced by three displacements measured along the beam subjected to the application of a transversal static force. Furthermore, the analytical procedure is validated by means of experimental tests.

Finally, in Chapter 4, a dynamic method for the identification of the axial load of a beam on elastic supports is presented, which makes use of any natural frequency and of five displacement components of the corresponding mode shape. The identification method proposed extends the algorithm by Tullini and Laudiero (2008) to the more general problem of a slender beam which presents unknown effective length and elastic end supports. In fact, for generic structures, such as truss structures, the effective length is unknown and the assumption of end rigid supports does not hold anymore. As for the end stiffness parameters, the method does not give an accurate estimation of full condensation matrices, but an estimate of diagonal terms only.

1

Exact stiffness matrix of Euler - Bernoulli beam for dynamic and stability elastic problems

1.1 Introduction

This Chapter provides the necessary background to introduce the governing equations used in the following chapters. Section 1.2 recalls the Hamilton's principles (Reddy 2002), which has been applied to the reference model of beam on elastic supports, subjected to an axial force and a lumped mass in-span. The differential problem obtained and its solution are presented in Section 1.3 (Graf 1975, Low 1999). In order to correctly describe the dynamic behaviour of global structure by means of a generic substructure, concepts about the dynamic substructuring with finite elements are needed. To this end, Section 1.4 reviews the finite element approach adopted to describe the dynamic behaviour of a beam by means of the classical and dynamic stiffness matrix (Leung 1993). In Section 1.5 some examples of dynamic stiffness of beams under different constraint conditions are given.

1.2 Fundamental principles of continuous dynamic system

The principle of virtual work is essentially a statement for the equilibrium definition of the dynamic system. It is also the foundation of the energy approach used for the dynamics of a system. In the following, the virtual work principle is firstly referred to static and later it is extended to the dynamic field, e.g. see Reddy (2002). Further D'Alembert's principle and Hamilton's principle are recalled to derive the equation of interest developed in the next chapters.

1.2.1 The virtual displacements principle

A given configuration κ of a continuous body B of volume $\mathbf{\Omega}$ is considered in equilibrium under body force **f** and surface tractions **t**. Displacements are assigned over portion Γ_u of the boundary and denoted by $\hat{\mathbf{u}}$, whereas tractions are assigned on portion Γ_σ and denoted by $\hat{\mathbf{t}}$. The boundary portions Γ_u and Γ_σ are disjointed and their union gives the total boundary, Γ. Let $\mathbf{u} = (u_1, u_2, u_3)$ denote the displacement vector corresponding to the equilibrium configuration of the body, and let σ_{ij} and ε_{ij} be the associated stress and strain components.

The set of admissible configuration is defined by sufficiently differentiable displacement fields that satisfy the geometric boundary conditions: $\mathbf{u} = \hat{\mathbf{u}}$ on Γ_u. Of all such admissible configuration, the actual one corresponds to the equilibrium configuration with the prescribed loads. In order to determine the displacements field **u** corresponding to the equilibrium configuration, a virtual displacement $\delta\mathbf{u}$ is superimposed to the equilibrium configuration. The principle of virtual displacements state that a continuous body is in equilibrium if and only if the virtual work of all internal and external forces vanishes for any virtual displacement, i.e.:

$$\int_\Omega \left(\mathbf{f} \cdot \delta\mathbf{u} - \boldsymbol{\sigma} \cdot \delta\boldsymbol{\varepsilon}\right) \mathrm{d}\mathbf{x} + \int_{\Gamma_\sigma} \hat{\mathbf{t}} \cdot \delta\mathbf{u} \, \mathrm{d}s = 0 \tag{1.1}$$

The strains $\delta\varepsilon$ are assumed to be compatible in the sense that the strain-displacement relations $\varepsilon_{ij} = 1/2\left(u_{i,j} + u_{j,i}\right)$ are satisfied. Eq. (1.1) is the mathematical statement of the principle of virtual displacements.

1.2.2 D'Alembert's principle

D'Alembert's principle extends the virtual work for static equilibrium into the realm of dynamic equilibrium. It suggests that, since the resultant of the forces **F** acting on the continuous body B results in its acceleration **a**, the application of a fictitious force equal to the inertia force would produce a state of equilibrium. Newton's second law of motion for a continuous body can be written in general terms as

$$\mathbf{F} - m\mathbf{a} = 0 \tag{1.2}$$

where m is the mass, **a** the acceleration vector. An application of D'Alembert's principle allow to consider the body B subjected to the forces **p** equal to the body force **f** increased by the inertia force

$$\mathbf{p} = \mathbf{f} - \rho \frac{\partial^2 \mathbf{u}}{\partial t^2} \tag{1.3}$$

where ρ is the mass density of the medium.

1.2.3 Hamilton's principle for continuous systems

Hamilton's principle is a generalization of the principle of virtual displacements to the dynamic of system of particles, rigid bodies, or deformable solids. The principle assumes that the system under consideration is characterized by two energy functions, a kinetic energy T and a potential energy U. For discrete systems, these energies can be described in terms of finite number of generalized coordinates and their derivatives with respect to time t. For continuous systems, the energies can be expressed in the terms of dependent variables which are functions of positions. The main difference between the former and the latter is the presence of internal energy W_I for deformable bodies. Hamilton's principle reduces to the principle of virtual displacements for systems that are in static equilibrium.

Let **F** denote the resultant of all forces acting on the continuous body B. The actual path $\mathbf{u} = \mathbf{u}(\mathbf{x},t)$ followed by material particle in position **x** in the body is varied, consistent with kinematic (essential) boundary conditions on Γ, to $\mathbf{u} + \delta\mathbf{u}$, where $\delta\mathbf{u}$ is the admissible variation (or virtual displacement) of the path. The varied path differs from the actual path except at initial and final times, t_1 and t_2, respectively. Thus, an admissible variation $\delta\mathbf{u}$ satisfies the conditions,

$$\begin{aligned} &\delta\mathbf{u} = \mathbf{0} \quad \text{on } \Gamma_u \text{ for all } t, \\ &\delta\mathbf{u}(x,t_1) = \delta\mathbf{u}(x,t_2) = \mathbf{0} \quad \text{for all } \mathbf{x} \end{aligned} \tag{1.4}$$

Substituting Eq. (1.3) into the equation on virtual displacements Eq. (1.1) and integrating with respect to time between t_1 and t_2

$$\int_{t_1}^{t_2} \left\{ \int_\Omega \left[\mathbf{f} \cdot \delta\mathbf{u} - \boldsymbol{\sigma} \times \delta\boldsymbol{\varepsilon} - \rho \frac{\partial^2 \mathbf{u}}{\partial t^2} \delta\mathbf{u} \right] \mathrm{d}\mathbf{x} + \int_{\Gamma_\sigma} \hat{\mathbf{t}} \cdot \delta\mathbf{u} \, \mathrm{d}s \right\} \mathrm{d}t = 0 \tag{1.5}$$

Integrating-by-parts the force inertia force term,

$$\int_{t_1}^{t_2} \left\{ \left[\int_\Omega \rho \frac{\partial \mathbf{u}}{\partial t} \frac{\partial \delta\mathbf{u}}{\partial t} + \mathbf{f} \cdot \delta\mathbf{u} - \boldsymbol{\sigma} \times \delta\boldsymbol{\varepsilon} \right] \mathrm{d}\mathbf{x} + \int_{\Gamma_\sigma} \hat{\mathbf{t}} \cdot \delta\mathbf{u} \, \mathrm{d}s \right\} \mathrm{d}t = 0 \tag{1.6}$$

Eq. (1.6) is known as the general form of *Hamilton's principle* for a continuous medium.
For an ideal elastic body a strain energy density function $U_0 = U_0(\varepsilon)$ exists so that

$$\sigma_{ij} = \frac{\partial U_0}{\partial \varepsilon_{ij}} \tag{1.7}$$

If **f** and $\hat{\mathbf{t}}$ are conservative forces,

$$\delta V = -\left(\int_{\Omega} \mathbf{f} \cdot \delta \mathbf{u} \, \mathrm{d}\mathbf{x} + \int_{\Gamma_\sigma} \hat{\mathbf{t}} \cdot \delta \mathbf{u} \, \mathrm{d}s \right) \tag{1.8}$$

where V is the external forces potential equal to the opposite of external work done by the forces **f** and $\hat{\mathbf{t}}$. Substituting Eq. (1.7) and (1.8) into Eq. (1.6),

$$\delta \int_{t_1}^{t_2} \left[T - (U + V) \right] \mathrm{d}t = 0 \tag{1.9}$$

where T and U are the kinetic and strain energies:

$$T = \int_{\Omega} \frac{\rho}{2} \frac{\partial \mathbf{u}}{\partial t} \cdot \frac{\partial \mathbf{u}}{\partial t} \, \mathrm{d}\mathbf{x}, \qquad U = \int_{\Omega} U_0 \, \mathrm{d}\mathbf{x} \tag{1.10}$$

Eq. (1.9) represents Hamilton's principle for an elastic body and states that of all such an admissible motion, the one that takes place makes minimum the *Hamiltonian action* I,:

$$I = \int_{t_1}^{t_2} \left[T - (U + V) \right] \mathrm{d}t \tag{1.11}$$

$$\delta I = \delta \int_{t_1}^{t_2} L \, \mathrm{d}t = 0 \tag{1.12}$$

The function $L = T - (U + V)$ is called *Lagrangian*. Recall that the sum of the strain energy and potential energy of external forces, $U+V$, is called *total potential energy* of the body Π. For bodies involving no motion (i.e. forces are applied sufficiently slowly so that the motion is independent from time and the inertia forces are negligible), Hamilton's principle reduces to the principle of virtual displacements. Eq. (1.9) may be viewed as the dynamics version of the principle of virtual displacements.

1.3 Equations of the reference model

In this section the equations of motion of an Euler-Bernoulli beam under general constraint and load conditions are derived. These equations are further used to describe its dynamic behaviour and to define the dynamic stiffness matrix. The analysis starts with the more general case of a beam on elastic supports carrying a lumped mass-in-span and subjected to an axial load. These models are used in the next chapters to develop an analytical procedure for the identification of the axial stress from the results of dynamic tests.

1.3.1 General formulation of the problem

A prismatic beam of length L is shown in Figure 1.1. A mass $\bar{m}$ is attached in its span through a rigid link of length l. The beam is subjected to an axial load N, positive sign is assigned to tensile forces, and to time-varying shear forces and bending moments acting on their end sections, $T_{0,1}(t)$ and $M_{0,1}(t)$. The cross section, the second moment of area, the elastic modulus and the specific weight, which are assumed as constant along the beam, are indicated, respectively, with A, J, E and ρ.

In order to consider general boundary conditions, the beam is supposed to be joined to a set of time dependent elastic springs, which can be grouped into two matrices, one for each beam end.

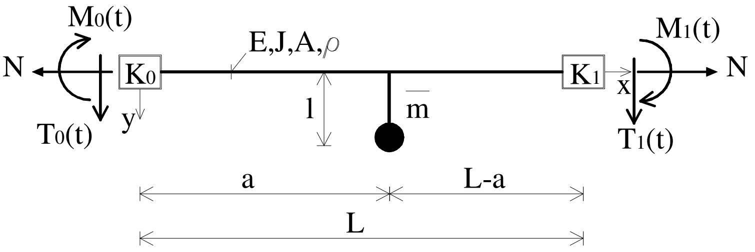

Figure 1.1 – Reference beam model

$$\mathbf{K}_0 = \begin{bmatrix} k_v^0 & k_{v\varphi}^0 \\ k_{v\varphi}^0 & k_\varphi^0 \end{bmatrix} \qquad \mathbf{K}_1 = \begin{bmatrix} k_v^1 & k_{v\varphi}^1 \\ k_{v\varphi}^1 & k_\varphi^1 \end{bmatrix} \tag{1.13}$$

The stiffness matrix of constraints contains translational springs k_v^0, k_v^1, rotational springs k_φ^0, k_φ^1, and mixed springs $k_{v\varphi}^0$, $k_{v\varphi}^1$, which simulate the coupling between the vertical displacement v and the bending moment or rotation φ and the shear force. These conditions enables to model an isolated beam belonging to a generic structure and exactly simulate the conditions on its connection to the rest of the structure.

In Euler-Bernoulli beam theory, shear deformations are neglected and beam cross section remains plane and perpendicular to the beam axes after the deformation, Figure 1.2.

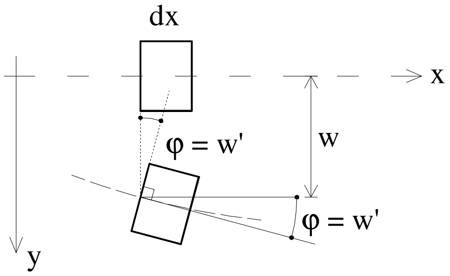

Figure 1.2 - Kinematic of a section of an Euler-Bernoulli beam

Consequently, the following displacements field has to be assumed:

$$S_x(x,y,t) = \varphi(x,t)\,y = -\frac{\partial w(x,t)}{\partial x}\,y \qquad S_y(x,y,t) = w(x,t) \tag{1.14}$$

where S_x and S_y are the axial and vertical displacements, respectively, whereas $w(x,t)$ and $\varphi(x,t) = -\,\partial w(x,t)/\partial x$ are transverse deflection and rotation of the cross. From displacements field (1.14) the only non-zero strain component is:

$$\varepsilon_x = \frac{\partial S_x(x,y,t)}{\partial x} = -y\,\frac{\partial^2 w(x,t)}{\partial x^2} \tag{1.15}$$

In order to derive the equation of motion by means of Hamilton's principle Eqs. (1.10) and (1.8) have to be employed. The kinetic energy T of all masses which experiment motion takes the form

$$\begin{aligned} T = {} & \frac{1}{2}\left[\int_0^L \rho A\left(\frac{\partial w(x,t)}{\partial t}\right)^2 + \rho J\left(\frac{\partial^2 w(x,t)}{\partial x\,\partial t}\right)^2\right]\mathrm{d}x + \\ & + \frac{1}{2}\bar{m}\left(\frac{\partial w(a,t)}{\partial t}\right)^2 + \frac{1}{2}\bar{m}l^2\left(\frac{\partial^2 w(a,t)}{\partial x\,\partial t}\right)^2 \end{aligned} \tag{1.16}$$

The four terms in Eq. (1.16) represent, respectively, the kinetic energy of the continuous beam in its transverse motion, the correspondently rotary inertia and the kinetic energies of the translational and rotational motion of the lumped mass around the section $x = a$.

The total strain energy U is the sum of the strain energy of the beam deformation U_b, due to the deflection and axial deformation, and the strain energy of the springs U_s

$$\begin{aligned}
&U = U_b + U_s \\
&U_b = \frac{1}{2}\int_0^{\mathrm{L}} EJ\left(\frac{\partial^2 w(x,t)}{\partial x^2}\right)^2 \mathrm{d}x \\
&U_s = \frac{1}{2}\begin{bmatrix} w(0,t) & \dfrac{\partial w(0,t)}{\partial x}\end{bmatrix}\begin{bmatrix} k_v^0 & k_{v\varphi}^0 \\ k_{v\varphi}^0 & k_\varphi^0\end{bmatrix}\begin{bmatrix} w(0,t) \\ \dfrac{\partial w(0,t)}{\partial x}\end{bmatrix} + \\
&+\frac{1}{2}\begin{bmatrix} w(L,t) & \dfrac{\partial w(L,t)}{\partial x}\end{bmatrix}\begin{bmatrix} k_v^1 & k_{v\varphi}^1 \\ k_{v\varphi}^1 & k_\varphi^1\end{bmatrix}\begin{bmatrix} w(L,t) \\ \dfrac{\partial w(L,t)}{\partial x}\end{bmatrix} = \\
&= \frac{1}{2}k_v^0\left(w(0,t)\right)^2 + \frac{1}{2}k_\varphi^0\left(\frac{\partial w(0,t)}{\partial x}\right)^2 + k_{v\varphi}^0 w(0,t)\frac{\partial w(0,t)}{\partial x} + \\
&+\frac{1}{2}k_v^1\left(w(L,t)\right)^2 + \frac{1}{2}k_\varphi^1\left(\frac{\partial w(L,t)}{\partial x}\right)^2 + k_{v\varphi}^1 w(L,t)\frac{\partial w(L,t)}{\partial x}
\end{aligned} \tag{1.17}$$

Finally the potential of external work V consists in the opposite of the work done by the forces acting at the beam ends for the boundary displacements

$$V = -\left[T_0\, w(0,t) + M_0\frac{\partial w(0,t)}{\partial x} + M_1\frac{\partial w(L,t)}{\partial x} + T_1 w(L,t) - \frac{1}{2}\int_0^L N\left(\frac{\partial w(x,t)}{\partial x}\right)^2 \mathrm{d}x\right] \tag{1.18}$$

Introducing Eq. (1.16), (1.17), (1.18) into Eq. (1.12) and separating the integration before and after $x = a$, the Hamilton's Principle

$$\delta I = \delta\int_{t_1}^{t_2} L\, dt = \delta\int_{t_1}^{t_2}\left[T - (U+V)\right] dt = \int_{t_1}^{t_2}\left[\delta T - (\delta U + \delta V)\right] dt = 0 \tag{1.19}$$

take the form

$$\begin{aligned}
&\delta\int_{t_1}^{t_2}\Bigg\{\int_0^{a^-}\left[\frac{1}{2}\rho A\left(\frac{\partial w(x,t)}{\partial t}\right)^2+\frac{1}{2}\rho J\left(\frac{\partial^2 w(x,t)}{\partial x\,\partial t}\right)^2-\frac{1}{2}EJ\left(\frac{\partial^2 w(x,t)}{\partial x^2}\right)^2-\frac{1}{2}N\left(\frac{\partial w(x,t)}{\partial x}\right)^2\right]\mathrm{d}x+\\
&+\int_{a^+}^{L}\left[\frac{1}{2}\rho A\left(\frac{\partial w(x,t)}{\partial t}\right)^2+\frac{1}{2}\rho J\left(\frac{\partial^2 w(x,t)}{\partial x\,\partial t}\right)^2-\frac{1}{2}EJ\left(\frac{\partial^2 w(x,t)}{\partial x^2}\right)^2-\frac{1}{2}N\left(\frac{\partial w(x,t)}{\partial x}\right)^2\right]\mathrm{d}x+\\
&+\frac{1}{2}\overline{m}\left(\frac{\partial w(a,t)}{\partial t}\right)^2+\frac{1}{2}\overline{m}l^2\left(\frac{\partial^2 w(a,t)}{\partial x\,\partial t}\right)^2+\\
&-\frac{1}{2}k_v^0\left(w(0,t)\right)^2-\frac{1}{2}k_\varphi^0\left(\frac{\partial w(0,t)}{\partial x}\right)^2-k_{v\varphi}^0 w(0,t)\frac{\partial w(0,t)}{\partial x}+\\
&-\frac{1}{2}k_v^1\left(w(L,t)\right)^2-\frac{1}{2}k_\varphi^1\left(\frac{\partial w(L,t)}{\partial x}\right)^2-k_{v\varphi}^1 w(L,t)\frac{\partial w(L,t)}{\partial x}+\\
&+T_0(t)\,w(0,t)+M_0(t)\frac{\partial w(0,t)}{\partial x}+T_1(t)\,w(L,t)+M_1(t)\frac{\partial w(L,t)}{\partial x}\Bigg\}\mathrm{d}t=0
\end{aligned} \tag{1.20}$$

Considering the fundamental rules of the variational calculus:

$$\begin{aligned}
&\delta f'=\delta\frac{\partial f}{\partial x}=\frac{\partial}{\partial x}\delta f=(\delta f)'\\
&\delta f''=\delta\frac{\partial^2 f}{\partial x^2}=\frac{\partial}{\partial x}\left(\delta\frac{\partial f}{\partial x}\right)=\frac{\partial}{\partial x}(\delta f)'=(\delta f')'\\
&\delta(f\cdot g')=\delta f\cdot g'+\delta g'\cdot f
\end{aligned} \tag{1.21}$$

and indicating with prime the spatial derivative and with point the temporal derivative, Eq. (1.20) becomes

$$\begin{aligned}
&\int_{t_1}^{t_2}\Bigg\{\int_0^{a^-}\left[\rho A\dot{w}\delta\dot{w}+\rho J\,\dot{w}'\delta\dot{w}'-EJ\,w''\delta w''-N\,w'\delta w'\right]\mathrm{d}x+\\
&+\int_{a^+}^{L}\left[\rho A\dot{w}\delta\dot{w}+\rho J\,\dot{w}'\delta\dot{w}'-EJ\,w''\delta w''-N\,w'\delta w'\right]\mathrm{d}x+\\
&+\overline{m}\dot{w}(a)\delta\dot{w}(a)+\overline{m}l^2\dot{w}'(a)\delta\dot{w}'(a)+\\
&-\delta w(0)\left[k_v^0 w(0)+k_{v\varphi}^0 w'(0)-T_0\right]+\\
&-\delta w(L)\left[k_v^1 w(L)+k_{v\varphi}^1 w'(L)-T_1\right]+\\
&-\delta w'(0)\left[k_\varphi^0 w'(0)+k_{v\varphi}^0 w(0)-M_0\right]+\\
&-\delta w'(L)\left[k_\varphi^1 w'(L)+k_{v\varphi}^1 w(L)-M_1\right]\Bigg\}\mathrm{d}x=0
\end{aligned} \tag{1.22}$$

The following terms are integrated-by-parts:

$$
\begin{aligned}
&\int_{t_1}^{t_2}\left\{\int_{0,a^+}^{a^-,L} \rho A\dot{w}\delta\dot{w}\,\mathrm{d}x\right\}\mathrm{d}t=-\int_{t_1}^{t_2}\left\{\int_{0,a^+}^{a^-,L} \rho A\ddot{w}\delta w\,\mathrm{d}x\right\}\mathrm{d}t\\
&\int_{t_1}^{t_2}\left\{\int_{0,a^+}^{a^-,L} \rho J\,\dot{w}'\delta\dot{w}'\,\mathrm{d}x\right\}\mathrm{d}t=-\int_{t_1}^{t_2}\left\{\left[\rho J\,\ddot{w}'\delta w\right]_{0,a^+}^{a^-,L}-\int_{0,a^-}^{a^-,L} \rho J\,\ddot{w}''\delta w\,\mathrm{d}x\right\}\mathrm{d}t\\
&\int_{t_1}^{t_2}\left\{\int_{0,a^+}^{a^-,L} EJ\,w''\delta w''\,\mathrm{d}x\right\}\mathrm{d}t=\int_{t_1}^{t_2}\left\{\left[EJ\,w''\delta w'-EJ\,w'''\delta w\right]_{0,a^+}^{a^-,L}-\int_{0,a^+}^{a^-,L} EJ\,w''''\delta w\,\mathrm{d}x\right\}\mathrm{d}t\\
&\int_{t_1}^{t_2}\left\{\int_{0,a^+}^{a^-,L} N\,w'\delta w'\,\mathrm{d}x\right\}\mathrm{d}t=\int_{t_1}^{t_2}\left\{\left[N\,w'\delta w\right]_{0,a^+}^{a^-,L}-\int_{0,a^+}^{a^-,L} N\,w''\delta w\,\mathrm{d}x\right\}\mathrm{d}t\\
&\int_{t_1}^{t_2}\overline{m}\dot{w}(a)\,\delta\dot{w}(a)\,\mathrm{d}t=-\int_{t_1}^{t_2}\overline{M}\,\ddot{w}(a)\,\delta w(a)\,\mathrm{d}t\\
&\int_{t_1}^{t_2}\overline{m}l^2\,\dot{w}'(a)\,\delta\dot{w}'(a)\,\mathrm{d}t=-\int_{t_1}^{t_2}\overline{m}l^2\,\ddot{w}'(a)\,\delta w'(a)\,\mathrm{d}t
\end{aligned}
\tag{1.23}
$$

In deriving Eqs. (1.23), the conditions reported in Eqs. (1.4) have been used, for which the extreme configurations at t_1 and t_2 are assigned, so that for all x $\delta w(x,t_1)=\delta w(x,t_2)=\delta w'(x,\ t_1)=\delta w'(x,\ t_2)=0$. After integration-by-parts, the stationary conditions of Hamiltonian action becomes

$$
\begin{aligned}
&\int_{t_1}^{t_2}\left\{\int_{0}^{a^-}-\delta w\left[\rho A\ddot{w}-\rho J\,\ddot{w}''+EJ\,w''''-N\,w''\right]\mathrm{d}x\right.\\
&+\int_{a^+}^{L}-\delta w\left[\rho A\ddot{w}-\rho J\,\ddot{w}''+EJ\,w''''-N\,w''\right]\mathrm{d}x+\\
&+\delta w(0)\left[-EJ\,w'''(0)+\rho J\,\ddot{w}'(0)+N\,w'(0)-k_v^0\,w(0)-k_{v\varphi}^0 w'(0)+T_0\right]+\\
&+\delta w(a)\Big[EJ\,w'''(a^-)-\overline{m}\ddot{w}(a)\,\cancel{-N\,w'(a^-)}\,\cancel{-\rho J\,\ddot{w}'(a^-)}+\\
&\qquad -EJ\,w'''(a^+)\,\cancel{+N\,w'(a^+)}\,\cancel{+\rho J\,\ddot{w}'(a^+)}\Big]\\
&\qquad +\delta w(L)\left[EJ\,w'''(L)-\rho J\,\ddot{w}'(L)-N\,w'(L)-k_v^1\,w(L)-k_{v\varphi}^1 w'(L)+T_1\right]+\\
&\qquad +\delta w'(0)\left[EJ\,w''(0)-k_\varphi^0 w'(0)-k_{v\varphi}^0 w(0)+M_0\right]+\\
&\qquad +\delta w'(a)\left[-EJ\,w''(a^-)+EJ\,w''(a^+)-\overline{m}l^2\,\ddot{w}'(a)\right]+\\
&\qquad +\delta w'(L)\left[-EJ\,w''(L)-k_\varphi^1\,w'(L)-k_{v\varphi}^1 w(L)+M_1\right]=0
\end{aligned}
\tag{1.24}
$$

The rotation functions w' and its acceleration $\ddot{w}'$ have to be continuous and integrable; hence conditions $w'(a^+)=w'(a^-)$ and $\ddot{w}'(a^+)=\ddot{w}'(a^-)$ are adopted in Eq. (1.24).

Because of the arbitrariness of δw, the bracketed expressions in the first two lines in Eq. (1.24) have to vanish. Therefore, the field equation is valid in $0 \le x \le L$:

$$\rho A \frac{\partial^2 w(x,t)}{\partial t^2} - \rho J \frac{\partial^4 w(x,t)}{\partial t^2 \partial x^2} + EJ \frac{\partial^2 w(x,t)}{\partial x^2} - N \frac{\partial w(x,t)}{\partial x} = 0 \tag{1.25}$$

If δw and $\delta w'$ are zero at $x = 0$, $x = a$ or $x = L$, essential (geometric) boundary conditions are assigned. Alternately, natural (static) boundary conditions in $x = 0$, L and internal conditions in $x = a$ are specified.

$$\begin{cases} EJ \dfrac{\partial^3 w(0,t)}{\partial x^3} - \rho J \dfrac{\partial^3 w(0,t)}{\partial x \, \partial t^2} + k_v^0 w(0,t) - \left(N - k_{v\varphi}^0\right) \dfrac{\partial w(0,t)}{\partial x} - T_0(t) = 0 \\ EJ \dfrac{\partial^2 w(0,t)}{\partial x^2} - k_\varphi^0 \dfrac{\partial w(0,t)}{\partial x} - k_{v\varphi}^0 w(0,t) + M_0(t) = 0 \\ EJ \dfrac{\partial^3 w(L,t)}{\partial x^3} - \rho J \dfrac{\partial^3 w(L,t)}{\partial x \, \partial t^2} - k_v^1 w(0,t) - \left(N + k_{v\varphi}^1\right) \dfrac{\partial w(L,t)}{\partial x} + T_1(t) = 0 \\ EJ \dfrac{\partial^2 w(L,t)}{\partial x^2} + k_\varphi^1 \dfrac{\partial w(L,t)}{\partial x} - k_{v\varphi}^1 w(L,t) - M_1(t) = 0 \end{cases} \tag{1.26}$$

$$\begin{cases} EJ \dfrac{\partial^3 w(a^-,t)}{\partial x^3} - EJ \dfrac{\partial^3 w(a^+,t)}{\partial x^3} - \bar{m} \dfrac{\partial^2 w(a,t)}{\partial t^2} = 0 \\ EJ \dfrac{\partial^2 w(a^-,t)}{\partial x^2} - EJ \dfrac{\partial^2 w(a^+,t)}{\partial x^2} + \bar{m} l^2 \dfrac{\partial^3 w(a,t)}{\partial x \, \partial t^2} = 0 \end{cases} \tag{1.27}$$

In addition to Eqs. (1.27) two more equations representing the displacement's and rotation's continuity at section $x = a$ have to be be written

$$\begin{cases} w(0,a^-) - w(0,a^+) = 0 \\ \dfrac{\partial w(a^-,t)}{\partial x} - \dfrac{\partial w(a^+,t)}{\partial x} = 0 \end{cases} \tag{1.28}$$

Eqs. (1.25), (1.26), (1.27) and (1.28) define the governing equations for the vibration of Euler-Bernoulli beam on elastic support, carrying a mass-in-span, subjected to axial load, shears and bending moments on its end sections, and taking into account rotary inertia.

1.3.2 Solution of the problem

At low vibration frequencies and for slender beams, the contribution of rotary inertia can be neglected. In this case the Eqs. (1.25) – (1.26) reduce to the following:

$$\rho A \frac{\partial^2 w(x,t)}{\partial t^2} + EJ \frac{\partial^2 w(x,t)}{\partial x^2} - N \frac{\partial w(x,t)}{\partial x} = 0 \tag{1.29}$$

$$\begin{cases} EJ \dfrac{\partial^3 w(0,t)}{\partial x^3} + k_v^0 w(0,t) - \left(N - k_{v\varphi}^0\right) \dfrac{\partial w(0,t)}{\partial x} - T_0(t) = 0 \\ EJ \dfrac{\partial^2 w(0,t)}{\partial x^2} - k_\varphi^0 \dfrac{\partial w(0,t)}{\partial x} - k_{v\varphi}^0 w(0,t) + M_0(t) = 0 \\ EJ \dfrac{\partial^3 w(L,t)}{\partial x^3} - k_v^1 w(0,t) - \left(N + k_{v\varphi}^1\right) \dfrac{\partial w(L,t)}{\partial x} + T_1(t) = 0 \\ EJ \dfrac{\partial^2 w(L,t)}{\partial x^2} + k_\varphi^1 \dfrac{\partial w(L,t)}{\partial x} - k_{v\varphi}^1 w(L,t) - M_1(t) = 0 \end{cases} \tag{1.30}$$

with the internal conditions (1.27) and (1.28).

To solve the partial differential equation (1.25), the method of separation of variables is employed (Graff, 1975)

$$w(x,t) = v(x)\, g(t) \tag{1.31}$$

where the *shape function* $v(x)$ is expressed in terms of x along the beam, and the *time function* $g(t)$ is related to the time t. Substituting Eq. (1.31) into Eq. (1.25) and then separating variables leads to

$$\frac{EJ}{\rho A} \frac{d^4 v(x)/dx^4}{v(x)} - N \frac{d^2 v(x)/dx^2}{v(x)} = -\frac{d^2 g(t)/dt^2}{g(t)} \tag{1.32}$$

Since v and g are depending on x and t, respectively, Eq. (1.32) must be equal to a constant, say ω^2. Thus, assuming a dimensionless coordinate $z = x/L$ and indicating with $m = \rho A$ the weight per unit length, the equation of normal modes and the equation of harmonic motions are

$$v''''(z) - n v''(z) - \lambda^4 v(z) = 0 \tag{1.33}$$

$$\ddot{g}(t) + \omega^2 g(t) = 0 \tag{1.34}$$

where these notations have been introduced

$$n = \frac{NL^2}{EJ} \qquad \lambda^4 = \frac{mL^4\omega^2}{EJ} \tag{1.35}$$

Let the solution of Eq. (1.33) be $v(x) = \mathrm{e}^{rx}$, then the characteristic equation is given by

$$r^4 - nr^2 - \lambda^4 = 0 \tag{1.36}$$

whose roots are

$$\begin{aligned} r_1 &= \mathrm{i}\, q_1^2 = \mathrm{i}\frac{1}{2}\left(\sqrt{n^2 + 4\lambda^4} - n\right) \\ r_2 &= -\mathrm{i}\, q_1^2 = -\mathrm{i}\frac{1}{2}\left(\sqrt{n^2 + 4\lambda^4} - n\right) \\ r_3 &= q_2^2 = \frac{1}{2}\left(\sqrt{n^2 + 4\lambda^4} + n\right) \\ r_4 &= -q_1^2 = -\frac{1}{2}\left(\sqrt{n^2 + 4\lambda^4} + n\right) \end{aligned} \tag{1.37}$$

Therefore, solution of Eq. (1.33) admits the representation

$$v(z) = C_1 \cos q_1 z + C_2 \sin q_1 z + C_3 \cosh q_2 z + C_4 \sinh q_2 z \tag{1.38}$$

where

$$q_1^2 = \frac{1}{2}\left(\sqrt{n^2 + 4\lambda^4} - n\right) \qquad q_2^2 = \frac{1}{2}\left(\sqrt{n^2 + 4\lambda^4} + n\right) \tag{1.39}$$

The constants C_1, …, C_4 can be determined using the boundary conditions of the member and characterize its *modal form of vibration*.

Similarly, the general solution of Eq. (1.34) is

$$g(t) = G_1 \cos \omega t + G_2 \sin \omega t \tag{1.40}$$

where the constants G_1 and G_2 should be determined from the initial conditions of displacement and velocity at given time.

The parameter ω assumes the meaning of *natural pulsations* of the vibration motion of the beam. Natural pulsation are the roots of the *frequency equation*, which are obtained by vanishing the determinant of the coefficient matrix of the boundary condition system. The generic solution of (1.29) can be written as

$$w(z,t)=\sum_{\mathrm{n=1}}^{\infty} v_n(z)\cdot\left(G_{1,n}\cos\omega_n t+G_{2,n}\sin\omega_n t\right) \tag{1.41}$$

where $v_n(z)$ represents the n-th mode shape

$$v_n(z)=C_{1,n}\cos\left[q_1(\omega_n)\,z\right]+C_{2,n}\sin\left[q_1(\omega_n)\,z\right]+C_{3,n}\cosh\left[q_2(\omega_n)\,z\right]+C_{4,n}\sinh\left[q_2(\omega_n)\,z\right] \tag{1.42}$$

Making use of Eq. (1.31), boundary and internal conditions (1.26), (1.27) and (1.28) reduce to

$$\text{Boundary conditions}\qquad \begin{cases} v'''(0)+\eta_0 v(0)+(n-\varsigma_0)\,v'(0)-\bar{T}_0=0\\ v''(0)-\beta_0 v'(0)-\varsigma_0 v(0)+\bar{M}_0=0\\ v'''(1)-\eta_1 v(1)+(n+\varsigma_1)\,v'(1)+\bar{T}_1=0\\ v''(1)+\beta_1 v'(1)-\varsigma_1 v(1)-\bar{M}_1=0 \end{cases} \tag{1.43}$$

$$\text{Internal conditions}\qquad \begin{cases} v'''(\alpha^-)-v'''(\alpha^+)+\mu\lambda^4 v(\alpha)=0\\ v'(\alpha^-)-v'(\alpha^+)-l^2/L^2\,\mu\lambda^4 v'(\alpha)=0\\ v(\alpha^-)-v(\alpha^+)=0\\ v'(\alpha^-,t)-v'(\alpha^+,t)=0 \end{cases} \tag{1.44}$$

where the following dimensionless parameters have been introduced

$$\begin{array}{lll} \eta_{0,1}=\dfrac{k_v^{0,1}L^3}{EJ} & \beta_{0,1}=\dfrac{k_\varphi^{0,1}L}{EJ} & \varsigma_{0,1}=\dfrac{k_{v\varphi}^{0,1}L^2}{EJ}\\ \bar{T}_{0,1}=\dfrac{T_{0,1}L^3}{EJ} & \bar{M}_{0,1}=\dfrac{M_{0,1}L}{EJ} & \mu=\dfrac{\bar{m}}{mL} \end{array} \tag{1.45}$$

1.4 Finite elements approaches

The solution of the governing equation (1.29) in the whole domain is generally untreatable for complex practical problems; consequently, it is useful to reduce the problem in smaller subdomains. The finite element discretization implies a division of the total volume into subdomains denoting finite elements. The function chosen to represent approximate displacement and stress field are specified within each element, and condition imposed on certain parameters at interelement boundaries provide the necessary continuity requirement of field functions.

In dynamic analysis, the shape functions for each beam element can be either frequency independent or frequency dependent. In the first case the shape functions satisfy the static governing equation, so yielding exact results in the finite element nodes, but in the dynamic case approximate frequencies and mode shapes are obtained. In the second case, the shape functions are the frequency-dependent solutions of the governing equation (1.29). In this case, the assembled stiffness matrix can be used to accurately predict an infinite number of frequencies and mode shapes with a minimum number of elements. In the following a brief introduction of both finite element approaches are given, e.g. see Leung (1993).

1.4.1 Classical finite element approach

A typical finite element is shown in Figure 1.3, such an element is a particular case of the more general problem presented in Section 1.3.1., where lumped mass and end springs are neglected. The beam is subjected to an axial force N, vertical displacements v_i, v_j and rotations θ_i, θ_j at the element ends i and j, their associated end moments and shears are denoted by M_i, M_j, and T_i, T_j.

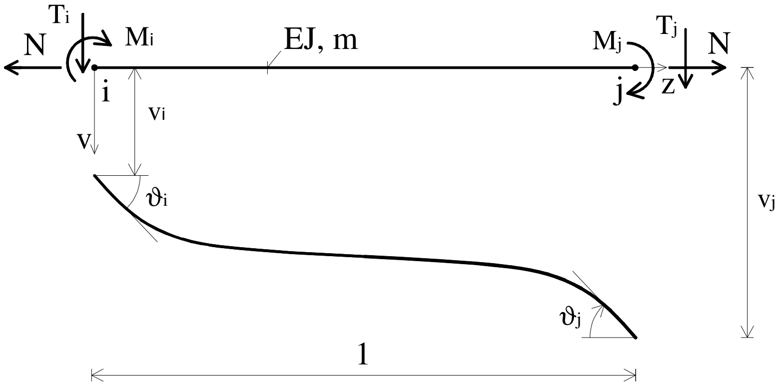

Figure 1.3 - Typical finite element

For an beam element with two nodes, the displacement field $w(z,t)$ is given by

$$\begin{aligned} w(z,t) &= \mathrm{N}_1(z)v_i(t)+\mathrm{N}_2(z)\theta_i(t)+\mathrm{N}_3(z)v_j(t)+\mathrm{N}_4(z)\theta_j(t) \\ &= \left(1-3z^2+2z^3\right)v_i(t)+\left(-z+3z^2-z^3\right)\theta_i(t)+ \\ &+\left(3z^2-2z^3+2z^3\right)v_j(t)+\left(z^2-z^3\right)\theta_j(t) \end{aligned} \tag{1.46}$$

where $\mathrm{N}_i = \mathrm{N}_i(z)$ represent the Hermite polynomials, collected into the shape functions matrix $\mathbf{N} = [\mathrm{N}_1, \mathrm{N}_2, \mathrm{N}_3, \mathrm{N}_4]^{\mathrm{T}}$, the nodal displacements are collected into the vector $\mathbf{u} = [v_i, \theta_j, v_i, \theta_j]^{\mathrm{T}}$.

The kinetic energy of the beam, Eq. (1.10), can be expressed by

$$T=\frac{1}{2}\int_0^L m\frac{\partial w}{\partial t}\frac{\partial w}{\partial t}\mathrm{d}x=\dot{\mathbf{u}}^T\left(\frac{1}{2}\int_0^L \mathbf{N}\,m\,\mathbf{N}^{\mathrm{T}}\mathrm{d}x\right)\dot{\mathbf{u}}=\frac{1}{2}\dot{\mathbf{u}}^{\mathrm{T}}\mathbf{M}\,\dot{\mathbf{u}} \tag{1.47}$$

where the term inside the brackets is called *mass matrix* of the element

$$\mathbf{M}=\frac{1}{2}\int_0^L \mathbf{N}\,m\,\mathbf{N}^{\mathrm{T}}\mathrm{d}x \tag{1.48}$$

The strain energy becomes

$$U=\frac{1}{2}\int_0^{\mathrm{L}} EJ\left(\frac{\partial^2 w(x,t)}{\partial x^2}\right)^2\mathrm{d}x=\dot{\mathbf{u}}^T\left(\frac{1}{2}\int_0^L \mathbf{N}''\,m\,\mathbf{N}''^{\mathrm{T}}\mathrm{d}x\right)\dot{\mathbf{u}}=\frac{1}{2}\dot{\mathbf{u}}^{\mathrm{T}}\mathbf{K}_E\,\dot{\mathbf{u}} \tag{1.49}$$

where $\mathbf{K}_E$ is the *stiffness matrix* of the element

$$\mathbf{K}_E=\frac{1}{2}\int_0^L \mathbf{N}''\,EJ\,\mathbf{N}''^{T}\mathrm{d}x \tag{1.50}$$

Considering the work done by the axial force, the potential of external work takes form

$$V=-\frac{1}{2}\int_0^{\mathrm{L}} N\left(\frac{\partial w(x,t)}{\partial x}\right)^2\mathrm{d}x=-\mathbf{u}^{\mathrm{T}}N\left(\frac{1}{2}\int_0^L \mathbf{N}'\,\mathbf{N}'^{\mathrm{T}}\mathrm{d}x\right)\mathbf{u}=-\frac{1}{2}\dot{\mathbf{u}}^{\mathrm{T}}\left(N\mathbf{K}_G\right)\dot{\mathbf{u}} \tag{1.51}$$

where $\mathbf{K}_G$ is the *geometric stiffness matrix* of the element

$$\mathbf{K}_G = \frac{1}{2}\int_0^L \mathbf{N}'\mathbf{N}'^{\mathrm{T}}\mathrm{d}x \tag{1.52}$$

The substitution of Eqs. (1.47), (1.49) and (1.51) into the Hamilton's principle yields

$$\mathbf{M}\,\ddot{\mathbf{u}}(t) + [\mathbf{K}_E + \mathbf{K}_G]\mathbf{u}(t) = \mathbf{F}(t) \tag{1.53}$$

where **F**(t) is the vector of generalized forces. For free vibration **F**(t) is zero, and Eq. (1.53) reduces to

$$\left[\mathbf{K}_{\mathrm{T}} - \omega^2\mathbf{M}\right]\mathbf{u} = \mathbf{0} \tag{1.54}$$

where $\mathbf{K}_{\mathrm{T}} = \mathbf{K}_E + \mathbf{K}_{\mathrm{G}}$ is the total stiffness matrix. Making use of Eqs. (1.50), (1.48) and (1.52) the stiffness matrix $\mathbf{K}_E$, consistent mass matrix **M** and geometric matrix $\mathbf{K}_G$ take the well known forms

$$\mathbf{K}_E = \frac{EJ}{L^3}\begin{bmatrix} 12 & 6L & -12 & 6L \\ & 4L^2 & -6L & 2L^2 \\ & & 12 & -6L \\ \text{sym} & & & 4L^2 \end{bmatrix} \quad (1.55) \quad \mathbf{M} = \frac{mL}{420}\begin{bmatrix} 156 & 22L & 54 & -13L \\ & 4L^2 & 13L & -3L^2 \\ & & 156 & -22L \\ \text{sym} & & & 4L^2 \end{bmatrix} \quad (1.56)$$

$$\mathbf{K}_G = \frac{N}{36L}\begin{bmatrix} 36 & 3L & -36 & 3L \\ & 4L^2 & -3L & -L^2 \\ & & 36 & -3L \\ \text{sym} & & & 4L^2 \end{bmatrix} \tag{1.57}$$

Since the Hermite polynomials do not satisfy the spatial differential equation (1.33), the solution of the vibration problem is approximate and mesh-dependent.

1.4.2 Dynamic stiffness matrix of the Euler-Bernoulli beam element

Unlike the classical element method, where the mass and stiffness matrix are obtained separately in order to solve the structural vibration problems, the dynamic stiffness matrix method offers a better alternative because it provides more accurate results, obtained from a matrix defined by exact theoretical methods.

The spatial governing equation is reported in Eq. (1.33), from which the shape functions are derived. The mode shape (1.38) can be represented in term of nodal displacements. Indicating with **C** the vector of unknowns C_1,.., C_4 and with $\boldsymbol{\varphi}(z)$ the vector of elementary functions, Eq. (1.38) can be written as

$$\begin{aligned} v &= C_1 \cos q_1 z + C_2 \sin q_1 z + C_3 \cosh q_2 z + C_4 \sinh q_2 z \\ &= \begin{bmatrix} \cos q_1 z & \sin q_1 z & \cosh q_2 z & \sinh q_2 z \end{bmatrix} \begin{bmatrix} C_1 \\ C_2 \\ C_3 \\ C_4 \end{bmatrix} = \boldsymbol{\varphi}^T (z) \mathbf{C} \end{aligned} \tag{1.58}$$

The four constants C_1,.., C_4 can be obtained in terms of nodal displacements of the beam:

$$\begin{cases} v_1(0) = v_i \\ v_1'(0) = \theta_i \\ v_2(1) = v_j \\ v_2'(1) = \theta_j \end{cases} \Leftrightarrow \begin{cases} C_1 + C_3 = v_i \\ q_1 C_2 + q_2 C_4 = \theta_i \\ C_1 \cos q_1 + C_2 \sin q_1 + C_3 \cosh q_2 + C_4 \sinh q_2 = v_j \\ -C_1 q_1 \sin q_1 + C_2 q_1 \cos q_1 + C_3 q_2 \sinh q_2 + C_4 q_2 \cosh q_2 = \theta_j \end{cases} \tag{1.59}$$

$$\Leftrightarrow \mathbf{\Phi C} = \mathbf{u}$$

where $\mathbf{\Phi}$ collects the coefficients of the linear system (1.59), whose resolution is:

$$\boldsymbol{\alpha} = \mathbf{\Phi}^{-1}\mathbf{u} \tag{1.60}$$

Using Eq. (1.60), the displacement field (1.58) can be written as

$$v = \boldsymbol{\varphi}(x)\boldsymbol{\alpha} = \boldsymbol{\varphi}(x)\mathbf{\Phi}^{-1}\mathbf{u} = \mathbf{N}(x,\omega)\mathbf{u} \tag{1.61}$$

where $\mathbf{N}(x, \omega) = \boldsymbol{\varphi}(x)\, \mathbf{\Phi}^{-1}$ collects the shape functions. They are frequency dependent because are function of the constants coefficients q_1, q_2 of Eq. (1.39), in turn function of natural frequency ω. The shape function matrix **N** is given in Leung (1993). The dynamic stiffness matrix $\mathbf{D}(\omega)$ relates the end-shears and moments to the end displacements in which the end-forces are

$$\begin{cases} \bar{T}_i = v'''(0) - nv'(0) \\ \bar{M}_j = -v''(0) \\ \bar{T}_j = -v'''(1) + nv'(1) \\ \bar{M}_j = v''(1) \end{cases} \tag{1.62}$$

which are derived from boundary conditions (1.43). Therefore by carrying out appropriate differentiations of the shape functions,

$$\begin{bmatrix} T_i \\ M_i \\ T_j \\ M_j \end{bmatrix} = \frac{EJ}{\chi L^3} \begin{bmatrix} F_6 & F_4 L & F_5 & F_3 L \\ & F_2 L^2 & -F_3 L & F_1 L^2 \\ & & F_6 & -F_4 L \\ \text{sym} & & & F_2 L^2 \end{bmatrix} \mathbf{u} = \mathbf{D}(\omega)\,\mathbf{u} \tag{1.63}$$

where $\mathbf{D}(\omega)$ is the dynamic stiffness matrix of the reference beam, which has both properties of stiffness and mass of the element combined in it. Indeed the elements of the matrix express the dynamic stiffness of the beam with a uniformly distribute mass. The generic term of the matrix represents the rising action when it undergoes a unitary displacement with time-varying harmonic law and with the other d.o.f clamped. Its elements are the following ones:

$$\begin{aligned} F_1 &= \left(q_1^2 + q_2^2\right)\left(q_2 \sin q_1 - q_1 \sinh q_2\right) \\ F_2 &= -\left(q_1 \cos q_1 \sinh q_2 - q_2 \sin q_1 \cosh q_2\right) \\ F_3 &= q_1 q_2 \left(q_1^2 + q_2^2\right)\left(\cos q_1 - \cosh q_2\right) \\ F_4 &= q_1 q_2 \left(\left(q_2^2 - q_1^2\right)\left(\cos q_1 \cosh q_2 - 1\right) + 2 q_1 q_2 \sin q_1 \sinh q_2\right) \\ F_5 &= q_1 q_2 \left(q_1^2 + q_2^2\right)\left(q_1 \sin q_1 + q_2 \sinh q_2\right) \\ F_6 &= q_1 q_2 \left(q_1^2 + q_2^2\right)\left(q_1 \sin q_1 \cosh q_2 + q_2 \cos q_1 \sinh q_2\right) \\ \chi &= -2 q_1 q_2 \left(\cos q_1 \cosh q_2 - 1\right) - \left(q_1^2 - q_2^2\right) \sin q_1 \sinh q_2 \end{aligned} \tag{1.64}$$

As shown in the previous section, the stiffness matrix **K**, the mass matrix **M** and the geometric matrix **G** admit the following representation:

$$\begin{aligned}
\mathbf{K}(\omega,N) &= \int_0^L EJ\,\mathbf{N}''^T(\omega,N,x)\,\mathbf{N}''(\omega,N,x)\,\mathrm{d}x \\
\mathbf{M}(\omega,N) &= \int_0^L m\mathbf{N}^T(\omega,N,x)\,\mathbf{N}(\omega,N,x)\,\mathrm{d}x \\
\mathbf{G}(\omega,N) &= \int_0^L \mathbf{N}'^T(\omega,N,x)\,\mathbf{N}'(\omega,N,x)\,\mathrm{d}x
\end{aligned} \tag{1.65}$$

The dynamic stiffness matrix of a system which vibrates harmonically at frequency ω relates the amplitudes of the response displacements to those of exciting forces. Let the beam be excited by a system of nodal forces $\mathbf{F}e^{i\omega t}$, the steady response is $\mathbf{u}e^{i\omega t}$; hence

$$\mathbf{D}(\omega)\mathbf{u} = \mathbf{F} \tag{1.66}$$

The **K** and **M** matrices in Eqs. (1.55), (1.56) are now rewritten using the classical normal modes as shape functions. Let introduce them into Eq. (1.54) and consider the case of free vibration, $\mathbf{F} = \mathbf{0}$:

$$\left[\mathbf{K}(\omega) - \omega^2\mathbf{M}(\omega)\right]\mathbf{u} = \mathbf{0} \tag{1.67}$$

and by comparing with Eq. (1.66)

$$\mathbf{D}(\omega) = \mathbf{K}(\omega) - \omega^2\mathbf{M}(\omega) \tag{1.68}$$

Furthermore it can be proved that the mass matrix is related to the dynamic stiffness matrix by Leung's theorem (Leung, 1978, Simpson, 1984)

$$\mathbf{M}(\omega) = -\frac{\partial \mathbf{D}(\omega)}{\partial \omega^2} \tag{1.69}$$

In other words the exact mass matrix can be obtained simply by differentiating the dynamic stiffness matrix with respect to the square of frequency.

If $\mathbf{D}(\omega)$ is expanded in Taylor series up to first order at $\omega = 0$ respect to ω^2, making use of (1.68) and (1.69), gives

$$\begin{aligned}\mathbf{D}(\omega) &= \mathbf{D}(0) + \omega^2 \left.\frac{\partial \mathbf{D}(\omega)}{\partial \omega^2}\right|_{\omega=0} + \sum_{i=2}^{\infty} \frac{(\omega^2)^n}{n!} \left.\frac{\partial^n \mathbf{D}(\omega)}{\partial (\omega^2)^n}\right|_{\omega=0} \\ &\cong \mathbf{K}(0) - \omega^2 \mathbf{M}(0) = \mathbf{K} - \omega^2 \mathbf{M}\end{aligned} \tag{1.70}$$

where **K** and **M** are the classical stiffness and mass matrix presented in the Eq. (1.55) using Hermite polynomials as shape function (Paz, 1990). Therefore, employing the classical static matrices for the vibration problem of the Euler-Bernoulli beam represents a first order approximation of the exact method of the dynamic stiffness matrix.

Eqs. (1.67) and (1.68) suggest that the dynamic stiffness matrix of a structure is useful to finding its natural modes of vibration. Indeed the vanishing of its determinant correspond to the frequency characteristic equation related to the eigenvalues problem, Eq. (1.54):

$$\mathrm{Det}\left[\mathbf{D}(\omega)\right] = \mathrm{Det}\left[\mathbf{K}(\omega) - \omega^2 \mathbf{M}(\omega)\right] \cong \mathrm{Det}\left[\mathbf{K} - \omega^2 \mathbf{M}\right] = 0 \tag{1.71}$$

Since the shape functions with which the matrix **D** is built are mathematically exact solutions of the governing equation for the free beam vibration, its elements can be used to predict an infinite number of modes with a minimum number of elements.

1.4.3 Dynamic stiffness matrix of the reference model

The model considered in this section consists in the beam analyzed previously with a lumped mass-in-span. This particular case, together with the previous one, is the analytical reference for the interpretation of the experimental test presented in the next chapters.

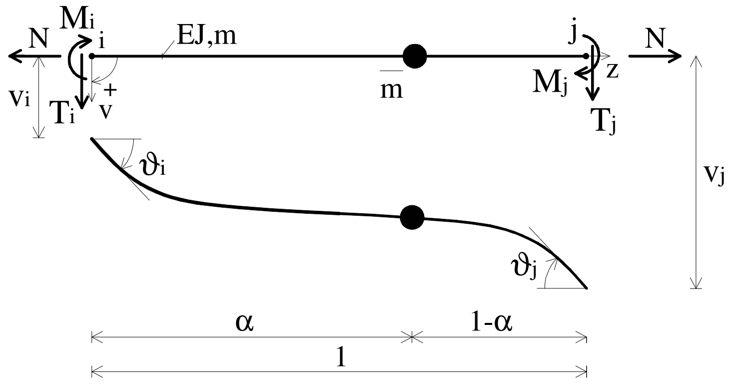

Figure 1.4 - Typical finite element

In order to construct the dynamic stiffness matrix of the reference element, it is necessary to subdivide the length into two subintervals, one before the lumped mass and an another after it. Consequently the two solutions of the field equation are:

$$\begin{array}{ll} v_1(z) = C_1 \cos q_1 z + C_2 \sin q_1 z + C_3 \cosh q_2 z + C_4 \sinh q_2 z & 0 \le z \le \alpha \\ v_2(z) = C_5 \cos q_1 z + C_6 \sin q_1 z + C_7 \cosh q_2 z + C_8 \sinh q_2 z & \alpha \le z \le 1 \end{array} \tag{1.72}$$

The eight constants can be obtained in terms of nodal displacements using the boundary and internal conditions

$$\text{End deformations} \qquad \begin{cases} v_1(0) = v_i \\ v_1'(0) = \theta_i \\ v_2(1) = v_j \\ v_2'(1) = \theta_j \end{cases} \tag{1.73}$$

$$\text{Internal conditions} \qquad \begin{cases} v_1(\alpha) - v_2(\alpha) = 0 \\ v_1'(\alpha) - v_2'(\alpha) = 0 \\ v_1'''(\alpha) - v_2'''(\alpha) + \mu\lambda^4 v_1(\alpha) = 0 \\ v_1''(\alpha) - v_2''(\alpha) = 0 \end{cases} \tag{1.74}$$

Solving the system (1.74) and introducing the constants into Eq. (1.62), the stiffness matrix of the element can be derived as sum of the stiffness matrix of the simple element derived in the previous section, Eq. (1.64), and that related to the lumped mass. In particular, for lumped mass placed in the midspan, $\alpha = 1/2$:

$$\mathbf{D}(\omega) = \frac{EJ}{\chi L^3} \begin{bmatrix} \bar{F}_6 & \bar{F}_4 L & \bar{F}_5 & \bar{F}_3 L \\ & \bar{F}_2 L^2 & -\bar{F}_3 L & \bar{F}_1 L^2 \\ & & \bar{F}_6 & -\bar{F}_4 L \\ \text{sym} & & & \bar{F}_2 L^2 \end{bmatrix} \tag{1.75}$$

where

$$
\begin{aligned}
\bar{F}_1 &= -\left(q_1^2+q_2^2\right)\left[2q_1q_2F_1+\mu\lambda^4F_1^M\right]\\
\bar{F}_2 &= \left(q_1^2+q_2^2\right)\left[2q_1q_2F_2+\mu\lambda^4F_2^M\right]\\
\bar{F}_3 &= -2q_1q_2\left(q_1^2+q_2^2\right)\left[F_3+\mu\lambda^4F_3^M\right]\\
\bar{F}_4 &= q_1q_2\left[2\left(q_1^2+q_2^2\right)F_4+\mu\lambda^4F_4^M\right]\\
\bar{F}_5 &= -q_1q_2\left(q_1^2+q_2^2\right)\left[2F_5+\mu\lambda^4F_5^M\right]\\
\bar{F}_6 &= q_1q_2\left(q_1^2+q_2^2\right)\left[2F_6+\mu\lambda^4F_6^M\right]\\
\bar{\chi} &= 2q_1q_2\left(q_1^2+q_2^2\right)\chi+\mu\lambda^4\chi^M
\end{aligned}
\tag{1.76}
$$

$$
\begin{aligned}
F_1^M &= q_1^2\left(1-\cosh q_2\right)-q_2^2\left(1-\cos q_1\right)+4q_1q_2\left(2\sin q_1/2\sinh q_2/2-\sin q_1\sinh q_2\right)\\
F_2^M &= q_1^2\cos q_1\left(1-\cosh q_2\right)-q_2^2\cosh q_2\left(1-\cos q_1\right)+\\
&\quad -2q_1q_2\left(2\sin q_1/2\sinh q_2/2-\sin q_1\sinh q_2\right)\\
F_3^M &= \left(\cos q_1/2-\cosh q_2/2\right)\left(q_1\sinh q_2/2-q_2\sin q_1/2\right)\\
F_4^M &= q_2\left(q_2^2-3q_1^2\right)\left(2\cosh q_2/2\sin q_1/2-\cosh q_2\sin q_1\right)+\\
&\quad +q_1\left(q_1^2-3q_2^2\right)\left(2\cos q_1/2\sinh q_2/2-\cos q_1\sinh q_2\right)\\
F_5^M &= q_1q_2F_6^M=\left(q_1^2-q_2^2\right)\left(\sin q_1\sinh q_2\right)+q_1q_2\left(\cos q_1\left(2\cosh q_2+1\right)+\right.\\
&\quad \left.-4\cos q_1/2\cosh q_2/2+\cosh q_2\right)\\
\chi^M &= \left(2q_1q_2\left(\cos q_1/2\cosh q_2/2-1\right)+\left(q_1^2-q_2^2\right)\sin q_1/2\sinh q_2/2\right)\cdot\\
&\quad \cdot 4\left(q_2\cosh q_2/2\sin q_1/2-q_1\cos q_1/2\sinh q_2/2\right)
\end{aligned}
\tag{1.77}
$$

Parameters F_1,.., F_6 and χ are given in Eq. (1.64). Eqs. (1.76) suggest that if the mass-in-span vanishes then the same stiffness coefficients given in equations (1.64) are obtained. Alternative formulation of Eq. (1.75) is given in Karnovsky (2000).

1.5 Dynamic stiffness of beams under different constraint conditions

In this section the stiffness coefficients of some remarkable cases of beams under various boundary conditions are derived. These results are used in the next chapter in order to derive the stiffness of substructures by means of exact dynamic condensation.

1.5.1 Clamped beam, translation of an end section

For the beam shown in Figure 1.5, the stiffness coefficient for the translation of an end section is simply provided by the (1,1) or (3,3) element of the dynamic stiffness matrix **D**(ω) (Eq. (1.75)):

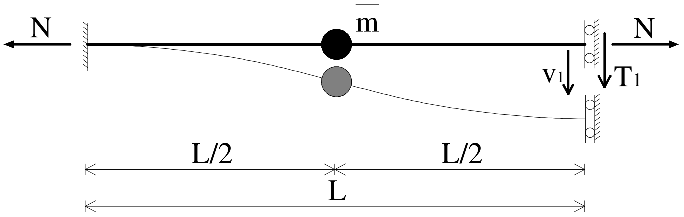

Figure 1.5 - Clamped-clamped beam

$$K^{M} = D_{v_i v_i} = D_{v_j v_j} = \frac{T_1}{v_1} = \frac{EJ}{L^3}\frac{\overline{F}_6}{\overline{\chi}} \tag{1.78}$$

Apex "*M*" indicates that the stiffness coefficient takes into account the lumped mass-in-span. Expanding $\overline{F}_6$, Eqs.(1.78) takes the form

$$K^{M} = \frac{EJ}{L^3}\frac{q_1 q_2\left(q_1^2+q_2^2\right)\left[2F_6+\mu\lambda^4 F_6^M\right]}{2q_1 q_2\left(q_1^2+q_2^2\right)\chi+\mu\lambda^4\chi^M} \tag{1.79}$$

Neglecting the presence of lumped mass-in-span, Eq. (1.79) becomes

$$K = \frac{EJ}{L^3}\frac{q_1 q_2\left(q_1^2+q_2^2\right)\left(q_1\cos q_1\cosh q_2+q_2\cos q_1\sinh q_2\right)}{\left(q_2^2-q_1^2\right)\sin q_1\sinh q_2-2q_1 q_2\left(\cos q_1\cosh q_2-1\right)} \tag{1.80}$$

Moreover, for $\overline{\mu},n,\lambda \to 0$, the dynamic stiffness of the model considered reduce to the well known static stiffness:

$$\lim_{\mu,n,\lambda\to 0} K^{M} = \frac{12EJ}{L^3} \tag{1.81}$$

1.5.2 Clamped-pinned beam, moment in one end section

For the beam depicted in Figure 1.6, the stiffness coefficient for the end rotation is simply provided by the (2,2) or (4,4) element of the dynamic stiffness matrix **D**(ω), Eq. (1.75)

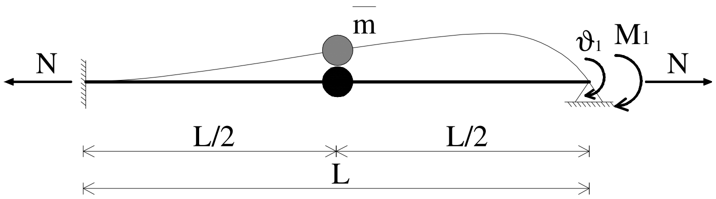

Figure 1.6 - Clamped - support beam

$$K^M = D_{\theta_i\theta_i} = D_{\theta_j\theta_j} = \frac{M_1}{\theta_1} = \frac{EJ}{L}\frac{\overline{F}_2}{\overline{\chi}} \tag{1.82}$$

From Eqs. (1.76) and (1.77), K^M takes the form

$$K^M = \frac{EJ}{L}\frac{\left(q_1^2+q_2^2\right)\left[2q_1q_2F_2+\mu\lambda^4F_2^M\right]}{2q_1q_2\left(q_1^2+q_2^2\right)\chi+\mu\lambda^4\chi^M} \tag{1.83}$$

Neglecting the presence of lumped mass-in-span, Eq. (1.83) reduces to

$$K = \frac{EJ}{L}\frac{\left(q_1^2+q_2^2\right)\left(q_1\cos q_1\sinh q_2 - q_2\sin q_1\cosh q_2\right)}{\left(q_1^2-q_2^2\right)\sin q_1\sinh q_2 + 2q_1q_2\left(\cos q_1\cosh q_2 - 1\right)} \tag{1.84}$$

Moreover, for $\overline{\mu},\mathrm{n},\lambda \rightarrow 0$, the dynamic stiffness of the model considered reduce to the well known static stiffness:

$$\lim_{\mu,\mathrm{n},\lambda\rightarrow 0} K^M = \frac{4EJ}{L} \tag{1.85}$$

1.5.3 Simply supported beam, rotation of an end section

A simple supported beam subjected to an axial force and carrying a mass-in-span located at the middle of the span as shown in Figure 1.7 is now considered.

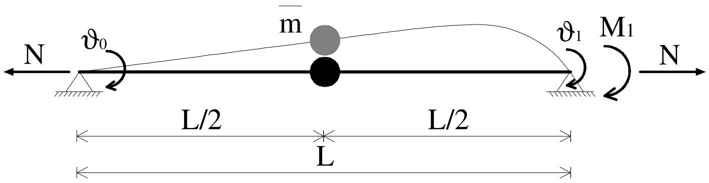

Figure 1.7 – Pinned-pinned beam, moment in one end section

The formulation of the dynamic equilibrium of the structure is

$$\mathbf{D}(\omega)\mathbf{u}=\mathbf{F} \qquad \frac{EJ}{\overline{\chi}L^3}\begin{bmatrix}\overline{F}_2L^2 & \overline{F}_1L^2\\ \overline{F}_1L^2 & \overline{F}_2L^2\end{bmatrix}\begin{bmatrix}\theta_0\\ \theta_1\end{bmatrix}=\begin{bmatrix}0\\ M_1\end{bmatrix} \tag{1.86}$$

Obtaining θ_0 from the first equation of the system in Eq. (1.86) and substituting it in the second one, the stiffness coefficient K^M is given by

$$\begin{aligned}K^M &= \frac{M_1}{\theta_1}=\frac{EJ}{\overline{\chi}L}\left[\frac{\overline{F}_2^2-\overline{F}_1^2}{\overline{F}_2^2}\right]\\ &=\frac{EJ}{L}\frac{\left(2F_2q_1q_2\left(q_1^2+q_2^2\right)+F_2^M\lambda^4\mu\right)^2-\left(F_1^M\lambda^4\mu-2F_1q_1q_2\left(q_1^2+q_2^2\right)^2\right)}{\left(2\chi q_1q_2\left(q_1^2+q_2^2\right)+\chi^{\mathrm{M}}\lambda^4\mu\right)\left(2F_2q_1q_2\left(q_1^2+q_2^2\right)+F_2^M\lambda^4\mu\right)}\end{aligned} \tag{1.87}$$

where F_i, ${F^M}_{i,}$ χ and χ^M are given in Eqs. (1.64) and (1.77). Neglecting the presence of lumped mass-in-span, Eq. (1.87) becomes

$$K=\frac{EJ}{L}\frac{\left(q_1^2+q_2^2\right)\sin q_1\sinh q_2}{q_2\sin q_1\cosh q_2-q_1\cos q_1\sinh q_2} \tag{1.88}$$

Moreover, for $\overline{\mu},\mathrm{n},\lambda\to 0$, the dynamic stiffness of the model considered reduce to the well known static stiffness:

$$\lim_{\mu,\mathrm{n},\lambda\to 0} K^M=\frac{3EJ}{L} \tag{1.89}$$

1.5.4 Simply supported beam, symmetric rotations

The same beam of the previous section is now subjected to two symmetric bending moments of its end sections, as shown in Figure 1.8.

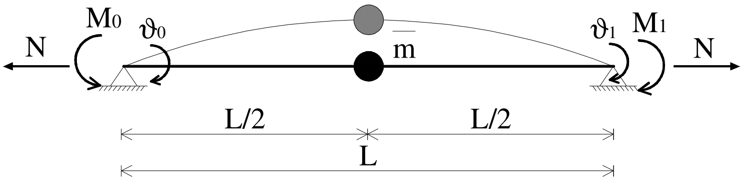

Figure 1.8 – Pinned-pined beam, symmetric rotations

The formulation of the dynamic equilibrium of the structure is

$$\frac{EJ}{\chi L^3}\begin{bmatrix}\bar{F}_2L^2 & \bar{F}_1L^2\\ \bar{F}_1L^2 & \bar{F}_2L^2\end{bmatrix}\begin{bmatrix}\theta_0\\ \theta_1\end{bmatrix}=\begin{bmatrix}M_0\\ M_1\end{bmatrix} \tag{1.90}$$

Because of the symmetry of the system: $\theta_0 = - \theta_1 = \theta$ and $M_0 = - M_1 = M$. Equating the sum of the two equations in Eq. (1.90), the stiffness coefficient is obtained

$$\begin{aligned}K^M &= \frac{M}{\theta} = \frac{EJ}{\chi L}\left[\bar{F}_2 - \bar{F}_1\right]\\ &= \frac{\left(q_1^2+q_2^2\right)\left(2q_1q_2\left(F_1+F_2\right)+\mu\lambda^4\left(F_1^M+F_2^M\right)\right)}{2q_1q_2\left(q_1^2+q_2^2\right)\chi+\mu\lambda^4\chi^{\mathrm{M}}}\end{aligned} \tag{1.91}$$

Neglecting the presence of lumped mass-in-span, Eq. (1.91) becomes

$$K=\frac{EJ}{L}\frac{\left(q_1^2+q_2^2\right)\left(q_1\sinh q_2\left(1+\cos q_1\right)-q_2\sin q_1\left(1+\cosh q_2\right)\right)}{2q_1q_2\left(\cos q_1\cosh q_2-1\right)+\left(q_1^2-q_2^2\right)\sin q_1\sinh q_2} \tag{1.92}$$

Moreover, for $\bar{\mu},\mathrm{n},\lambda \to 0$, the dynamic stiffness of the model considered reduce to the well known static stiffness:

$$\lim_{\mu,\mathrm{n},\lambda\to 0} K^M = \frac{2EJ}{L} \tag{1.93}$$

1.5.5 Simply supported beam, asymmetric rotations

For the same model of the previous section, asymmetric rotations are now considered, Figure 1.9.

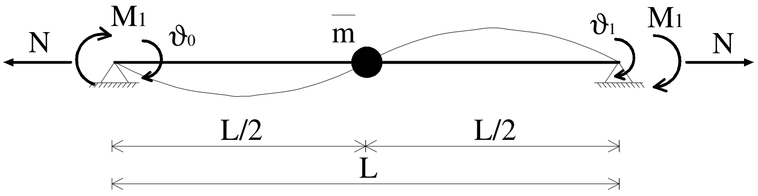

Figure 1.9 – Pinned-pined beam, asymmetric rotations

The formulation of the dynamic equilibrium of the structure is

$$\frac{EJ}{\bar{\chi}L^3}\begin{bmatrix}\bar{F}_2L^2 & \bar{F}_1L^2\\ \bar{F}_1L^2 & \bar{F}_2L^2\end{bmatrix}\begin{bmatrix}\theta_0\\ \theta_1\end{bmatrix}=\begin{bmatrix}M_0\\ M_1\end{bmatrix} \tag{1.94}$$

Because of the asymmetry of the system: $\theta_0 = \theta_1 = \theta$ and $M_0 = M_1 = M$. Equating the sum of the two equations in Eq. (1.94), the stiffness coefficient is obtained

$$\begin{aligned} K^M &= \frac{M}{\theta} = \frac{EJ}{\bar{\chi}L}\left[\bar{F}_1 + \bar{F}_2\right] \\ &= \frac{\left(q_1^2+q_2^2\right)\left(2q_1q_2\left(F_2-F_1\right)+\mu\lambda^4\left(F_2^M-F_1^M\right)\right)}{2q_1q_2\left(q_1^2+q_2^2\right)\chi+\mu\lambda^4\chi^{\mathrm{M}}} \end{aligned} \tag{1.95}$$

Neglecting the presence of lumped mass-in-span, the dynamic stiffness becomes

$$K = \frac{EJ}{L}\frac{\left(q_1^2+q_2^2\right)\left(q_1\sinh q_2\left(\cos q_1-1\right)+q_2\sin q_1\left(1-\cosh q_2\right)\right)}{2q_1q_2\left(\cos q_1\cosh q_2-1\right)+\left(q_1^2-q_2^2\right)\sin q_1\sinh q_2} \tag{1.96}$$

Moreover, for $\bar{\mu},\mathrm{n},\lambda \to 0$, the dynamic stiffness of the model considered reduce to the well known static stiffness:

$$\lim_{\mu,\mathrm{n},\lambda\to 0} K^M = \frac{6EJ}{L} \tag{1.97}$$

1.5.6 Cantilever beam, moment at free end

For the cantilever beam in Figure 1.10, the formulation of the dynamic equilibrium is

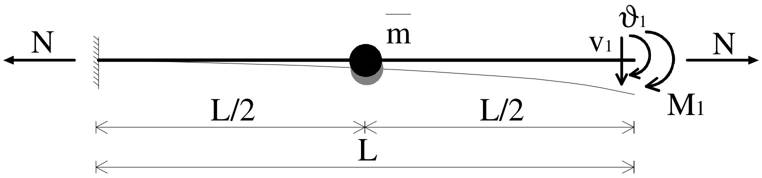

Figure 1.10 - Cantilever beam, moment at free end

$$\frac{EJ}{\chi L^3}\begin{bmatrix} \overline{F}_6 & -\overline{F}_4 L \\ -\overline{F}_4 L & \overline{F}_2 L^2 \end{bmatrix}\begin{bmatrix} v_1 \\ \theta_1 \end{bmatrix}=\begin{bmatrix} 0 \\ M_1 \end{bmatrix} \tag{1.98}$$

Solving for v_1 the first equation of the system in Eq. (1.98) and substituting it to the second one, the sought stiffness coefficient is

$$K^M=\frac{M_1}{\theta_1}=\frac{EJ}{\chi L}\left[\frac{\overline{F}_2\overline{F}_6-\overline{F}_4^2}{\overline{F}_6}\right] \tag{1.99}$$

The explicit formulas are too complicated to be exposed.
Moreover, for $\overline{\mu},n,\lambda \to 0$, the dynamic stiffness of the model considered reduces to the well known static stiffness:

$$\lim_{\mu,n,\lambda\to 0} K^M=\frac{EJ}{L} \tag{1.100}$$

1.5.7 Cantilever beam, shear force at free end

For the cantilever beam in Figure 1.11, the formulation of the dynamic equilibrium is

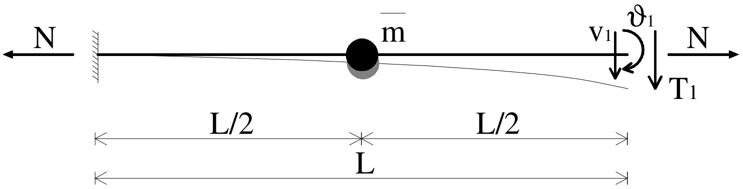

Figure 1.11 - Cantilever beam, shear force at free end

$$\frac{EJ}{\chi L^3}\begin{bmatrix} \bar{F}_6 & -\bar{F}_4 L \\ -\bar{F}_4 L & \bar{F}_2 L^2 \end{bmatrix}\begin{bmatrix} v_1 \\ \theta_1 \end{bmatrix}=\begin{bmatrix} T_1 \\ 0 \end{bmatrix} \tag{1.101}$$

Solving for θ_1 the second equation of the system in Eq. (1.101) and substituting it to the first one, the dynamic stiffness is given by

$$K^M=\frac{T_1}{v_1}=\frac{EJ}{\chi L^3}\left[\frac{\bar{F}_2\bar{F}_6-\bar{F}_4^2}{\bar{F}_2}\right] \tag{1.102}$$

The explicit formulas are too complicated to be exposed.
Moreover, for $\bar{\mu},n,\lambda \to 0$, the dynamic stiffness of the model considered reduces to the well known static stiffness:

$$\lim_{\mu,n,\lambda\to 0} K^M=\frac{3EJ}{L^3} \tag{1.103}$$

1.5.8 Pinned beam at one end and only translation allowed at the other end

For the beam in Figure 1.12, the formulation of the dynamic equilibrium is

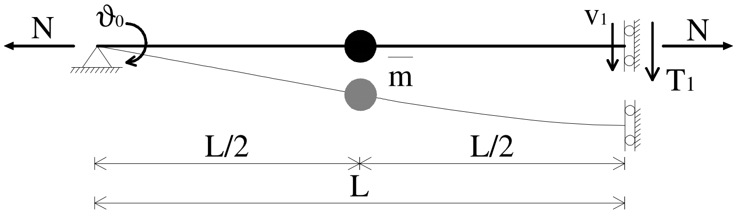

Figure 1.12 - Pinned beam at one end and only translation allowed at the other end

$$\frac{EJ}{\chi L^3}\begin{bmatrix} \bar{F}_2 L^2 & -\bar{F}_3 L \\ -\bar{F}_3 L & \bar{F}_6 \end{bmatrix}\begin{bmatrix} \theta_0 \\ v_1 \end{bmatrix}=\begin{bmatrix} 0 \\ T_1 \end{bmatrix} \tag{1.104}$$

Solving for θ_0 the second equation of the system in Eq. (1.101) and substituting it to the first one, the dynamic stiffness is given by

$$K^M=\frac{T_1}{v_1}=\frac{EJ}{\chi L^2}\left[\frac{\bar{F}_2\bar{F}_6-\bar{F}_3^2}{\bar{F}_3}\right] \tag{1.105}$$

Neglecting the presence of lumped mass-in-span, the dynamic stiffness becomes

$$K = \frac{EJ}{L^2} \frac{\left(q_1^2 + q_2^2\right) \cos q_1 \cosh q_2}{\cosh q_2 - \cos q_1} \tag{1.106}$$

Moreover, for $\bar{\mu}, n, \lambda \to 0$, the dynamic stiffness of the model considered reduce to the well known static stiffness:

$$\lim_{\mu, n, \lambda \to 0} K^M = \frac{2EJ}{L^2} \tag{1.107}$$

1.6 Conclusions

Making use of Hamilton's principle, the governing equations of the vibration problem of a Euler-Bernoulli beam carrying a mass-in-span have been obtained. In particular, general constraint for beam on elastic supports, subjected to axial load, shears and bending moments on its end sections, have been obtained. Since a correct description of the dynamic behaviour of a structure by means of a substructure needs the use of the dynamic stiffness matrix, exact finite element are adopted. Correspondingly, the shape functions are frequency-dependent solutions of the governing equations; hence, the assembled stiffness matrix can be used to accurately predict an infinite number of frequencies and mode shapes with a minimum number of elements.

Finally, the stiffness coefficients of some remarkable cases of beams under various boundary have been derived. Indeed, the dynamic stiffness matrix characterizes the basis of the substructuring method, which is introduced in the following chapter.

2

Exact dynamic condensation of frames using the dynamic stiffness matrix

2.1 Introduction

In this chapter it is shown that, in order to study the dynamic behaviour of a simple substructure extracted from a generic structure, exact dynamic condensation method is required. This technique allows to derive the stiffness condensation parameters which are to be assigned to the substructure to re-establish the global behaviour of the structure without loss of information.

Firstly static and Guyan’s reduction methods are introduced, in Section 2.2 and 2.3, respectively (Guyan 1964, Hatch 2001). Both methods require the selection of a limited number of degree of freedom, (master dof), which capture the essential physical behaviour of the structure. It will be shown that, under specific conditions, static condensation can be defined as an exact method, whereas Guyan’s reduction method gives only approximate results. Indeed this procedure makes use of classical stiffness and mass matrices, which inevitably provides a mesh-dependent result.

Moreover, making use of the dynamic stiffness matrix introduced in Chapter 1, Section 2.4 shows that exact dynamic condensation provides the exact parameters to be used as boundary conditions for the substructure, with a minimum number of finite element (Leung 1978). Therefore it will be used to formulate the reduced model of the structure of interest for the experimental tests of Chapter 3 and 4.

Finally, in Sections 2.5-2.6-2.7, some examples utilized in Chapter 3 and 4 are carried out.

2.2 Static condensation

Static condensation involves the separation of the degrees of freedom (dof) into master and slave components. If master dofs are chosen so as to include all dof where forces/moments are applied and also dof where displacements are desired, the resulting solution is exact. In the opposite case, an approximate solution only is obtained. For dynamic problems, master dof are typically chosen as displacements and rotations corresponding to the higher masses and mass moments. Hence, the first step is to rearrange the dof (rows and columns of the stiffness matrix) into independent (master) displacements $\mathbf{u}_\mathrm{m}$ and dependent (slave) displacements $\mathbf{u}_\mathrm{s}$ to be reduced (Hatch, 2001):

$$\mathbf{K}\mathbf{u} = \mathbf{F} \tag{2.1}$$

$$\left[\begin{array}{c:c} \mathbf{K}_\mathrm{ss} & \mathbf{K}_\mathrm{sm} \\ \hdashline \mathbf{K}_\mathrm{ms} & \mathbf{K}_\mathrm{mm} \end{array}\right] \left[\begin{array}{c} \mathbf{u}_\mathrm{s} \\ \hdashline \mathbf{u}_\mathrm{m} \end{array}\right] = \left[\begin{array}{c} \mathbf{F}_\mathrm{s} \\ \hdashline \mathbf{F}_\mathrm{m} \end{array}\right] \tag{2.2}$$

The first matrix equation:

$$\mathbf{K}_\mathrm{ss}\mathbf{u}_\mathrm{s} + \mathbf{K}_\mathrm{sm}\mathbf{u}_\mathrm{sm} = \mathbf{F}_\mathrm{s} \tag{2.3}$$

can be solved for $\mathbf{u}_\mathrm{s}$ giving

$$\mathbf{u}_\mathrm{s} = \mathbf{K}_\mathrm{ss}^{-1}\left(\mathbf{F}_s - \mathbf{K}_\mathrm{sm}\mathbf{u}_\mathrm{sm}\right) \tag{2.4}$$

or

$$\mathbf{u}_\mathrm{s} = -\mathbf{K}_\mathrm{ss}^{-1}\mathbf{K}_\mathrm{sm}\mathbf{u}_\mathrm{m} \tag{2.5}$$

if no forces (moments) are applied at the dependent (slave) dof ($\mathbf{F}_\mathrm{s} = \mathbf{0}$). Rewriting the displacement vector in terms of $\mathbf{u}_\mathrm{m}$ only:

$$\mathbf{u} = \left[\begin{array}{c} \mathbf{u}_\mathrm{s} \\ \hdashline \mathbf{u}_\mathrm{m} \end{array}\right] = \left[\begin{array}{c} -\mathbf{K}_\mathrm{ss}^{-1}\mathbf{K}_\mathrm{sm} \\ \hdashline \mathbf{I} \end{array}\right] \mathbf{u}_\mathrm{m} = \left[\begin{array}{c} -\mathbf{K}_\mathrm{ss}^{-1}\mathbf{K}_\mathrm{sm}\mathbf{u}_\mathrm{m} \\ \hdashline \mathbf{u}_\mathrm{m} \end{array}\right] \tag{2.6}$$

and defining a transformation matrix for brevity

$$\mathbf{u} = \left[\begin{array}{c} \mathbf{u}_{\mathrm{s}} \\ \hdashline \mathbf{u}_{\mathrm{m}} \end{array}\right] = \left[\begin{array}{c} -\mathbf{K}_{\mathrm{ss}}^{-1}\mathbf{K}_{\mathrm{sm}} \\ \hdashline \mathbf{I} \end{array}\right] \mathbf{u}_{\mathrm{m}} = \left[\begin{array}{c} \mathbf{T}_{\mathrm{sm}} \\ \hdashline \mathbf{I} \end{array}\right] \mathbf{u}_{\mathrm{m}} = \mathbf{T}\mathbf{u}_{\mathrm{m}} \tag{2.7}$$

where

$$\mathbf{T}_{\mathrm{sm}} = -\mathbf{K}_{\mathrm{ss}}^{-1}\mathbf{K}_{\mathrm{sm}} \qquad \text{and} \qquad \mathbf{T} = \left[\begin{array}{c} \mathbf{T}_{\mathrm{sm}} \\ \hdashline \mathbf{I} \end{array}\right] \tag{2.8}$$

the original static equilibrium equation takes the form

$$\mathbf{K}\,\mathbf{u} = \mathbf{K}\left(\mathbf{T}\,\mathbf{u}_{\mathrm{m}}\right) = \mathbf{F} \tag{2.9}$$

Multiplying both sides by $\mathbf{T}^{\mathrm{T}}$ to reduce the number of degrees of freedom from (s + m) to (m)

$$\left(\mathbf{T}^{\mathrm{T}}\,\mathbf{K}\,\mathbf{T}\right)\mathbf{u}_{\mathrm{m}} = \mathbf{T}^{\mathrm{T}}\mathbf{F} \tag{2.10}$$

the term in parentheses above is redefined to be $\mathbf{K}^{*}_{\mathrm{mm}}$

$$\begin{aligned} \mathbf{K}^{*}_{\mathrm{mm}} &= \mathbf{T}^{\mathrm{T}}\mathbf{K}\,\mathbf{T} = \left[\begin{array}{c:c} \mathbf{T}_{\mathrm{sm}}^{\mathrm{T}} & \mathbf{I} \end{array}\right] \left[\begin{array}{c:c} \mathbf{K}_{\mathrm{ss}} & \mathbf{K}_{\mathrm{sm}} \\ \hdashline \mathbf{K}_{\mathrm{ms}} & \mathbf{K}_{\mathrm{mm}} \end{array}\right] \left[\begin{array}{c} \mathbf{T}_{\mathrm{sm}} \\ \hdashline \mathbf{I} \end{array}\right] \\ &= \mathbf{K}_{\mathrm{mm}} - \mathbf{K}_{\mathrm{ms}}\mathbf{K}_{\mathrm{ss}}^{-1}\mathbf{K}_{\mathrm{sm}} \end{aligned} \tag{2.11}$$

where

$$\mathbf{T}_{\mathrm{sm}} = -\mathbf{K}_{\mathrm{ss}}^{-1}\mathbf{K}_{\mathrm{sm}} \quad \text{and} \quad \mathbf{T}_{\mathrm{sm}}^{\mathrm{T}} = -\mathbf{K}_{\mathrm{ms}}\mathbf{K}_{\mathrm{ss}}^{-1} \tag{2.12}$$

Hence, the original (m + s) dof problem now can be transformed to an (m) dof problem by partitioning into dependent and independent dof, and solving for the reduced stiffness matrix $\mathbf{K}^{*}_{\mathrm{mm}}$ and force vector $\mathbf{F}_{\mathrm{m}}$:

$$\begin{aligned}\mathbf{F}_\mathrm{m}^* &= \mathbf{T}^\mathrm{T}\mathbf{F} \\ &= \left[\mathbf{T}_\mathrm{sm}^\mathrm{T} \;\vdots\; \mathbf{I}\right]\left[\begin{array}{c}\mathbf{F}_\mathrm{s} \\ \hline \mathbf{F}_\mathrm{m}\end{array}\right] = \mathbf{T}_\mathrm{ms}\mathbf{F}_\mathrm{s} + \mathbf{F}_\mathrm{m} \\ &= \mathbf{F}_\mathrm{m} - \mathbf{K}_\mathrm{ms}\mathbf{K}_\mathrm{ss}^{-1}\mathbf{F}_\mathrm{s}\end{aligned} \tag{2.13}$$

Then the reduced problem becomes:

$$\mathbf{K}_\mathrm{mm}^* \mathbf{u}_\mathrm{m} = \mathbf{F}_\mathrm{m}^* \tag{2.14}$$

After the $\mathbf{u}_\mathrm{m}$ dofs are known, the $\mathbf{u}_\mathrm{s}$ dofs can be expanded from the master $\mathbf{u}_\mathrm{m}$ using, if $\mathbf{F}_\mathrm{s} = \mathbf{0}$, Eq. (2.5).

2.3 Dynamic condensation: Guyan's reduction method

In a large-scale structural analysis, not all the nodes are subjected to external forces, nor all the nodal displacements are of interest. Substructure methods of dynamic analysis have been developed, which reduces the number of coordinates of a complex structures. The terms *master* and *slave* refer to the interface coordinates and internal coordinates of a substructure, respectively. The category of substructure method of interest is based on the elimination of the slaves in the dynamic stiffness relations.

Guyan's reduction is a method of decreasing the number of degrees of freedom in a dynamics problem, similar to the process of static condensation. Unlike static condensation, however, Guyan's reduction introduces errors due to an approximation, as shown in the following. The magnitude of the errors introduced depends upon the choice of the dof to be reduced (Hatch, 2001).

Consider the undamped equations of motion

$$\mathbf{M}\ddot{\mathbf{u}} + \mathbf{K}\mathbf{u} = \mathbf{F} \tag{2.15}$$

Is it possible to rearrange and partition Eq. (2.15) into displacements to be reduced, $\mathbf{u}_\mathrm{s}$, and independent displacements, $\mathbf{u}_\mathrm{m}$

$$\left[\begin{array}{c|c}\mathbf{M}_\mathrm{ss} & \mathbf{M}_\mathrm{sm} \\ \hline \mathbf{M}_\mathrm{ms} & \mathbf{M}_\mathrm{mm}\end{array}\right]\left[\begin{array}{c}\ddot{\mathbf{u}}_\mathrm{s} \\ \hline \ddot{\mathbf{u}}_\mathrm{m}\end{array}\right] + \left[\begin{array}{c|c}\mathbf{K}_\mathrm{ss} & \mathbf{K}_\mathrm{sm} \\ \hline \mathbf{K}_\mathrm{ms} & \mathbf{K}_\mathrm{mm}\end{array}\right]\left[\begin{array}{c}\mathbf{u}_\mathrm{s} \\ \hline \mathbf{u}_\mathrm{m}\end{array}\right] = \left[\begin{array}{c}\mathbf{F}_\mathrm{s} \\ \hline \mathbf{F}_\mathrm{m}\end{array}\right] \tag{2.16}$$

The first equation of the system in Eq. (2.16)

$$\mathbf{M}_{ss}\ddot{\mathbf{u}}_s + \mathbf{M}_{sm}\ddot{\mathbf{u}}_m + \mathbf{K}_{ss}\mathbf{u}_s + \mathbf{K}_{sm}\mathbf{u}_m = \mathbf{F}_s \tag{2.17}$$

can be solved for $\mathbf{u}_s$

$$\begin{aligned} \mathbf{u}_s &= \mathbf{K}_{ss}^{-1}\left(\mathbf{F}_s - \mathbf{K}_{sm}\mathbf{u}_m - \mathbf{M}_{ss}\ddot{\mathbf{u}}_s - \mathbf{M}_{sm}\ddot{\mathbf{u}}_m\right) \\ &= -\mathbf{K}_{ss}^{-1}\mathbf{K}_{sm}\mathbf{u}_m + \mathbf{K}_{ss}^{-1}\left(\mathbf{F}_s - \mathbf{M}_{ss}\ddot{\mathbf{u}}_s - \mathbf{M}_{sm}\ddot{\mathbf{u}}_m\right) \end{aligned} \tag{2.18}$$

Instead of letting $\mathbf{u}_s$ depend upon the entire right-end side of Eq. (2.18), the following approximation of static equilibrium is introduced

$$\mathbf{u}_s = -\mathbf{K}_{ss}^{-1}\mathbf{K}_{sm}\mathbf{u}_m \tag{2.19}$$

Typically the choice of degrees of freedom to be reduced does not include any degrees of freedom to which forces are applied, thus $\mathbf{F}_s = \mathbf{0}$. The static equilibrium approximation basically sets the term in brackets in Eq. (2.18) to zero. Setting $\mathbf{F}_s = \mathbf{0}$ and using the second derivative of Eq. (2.19), the form of $\mathbf{M}_{sm}$ is

$$\begin{aligned} \mathbf{0} &= \mathbf{F}_s - \mathbf{M}_{ss}\ddot{\mathbf{u}}_s - \mathbf{M}_{sm}\ddot{\mathbf{u}}_m \\ &= -\mathbf{M}_{ss}\ddot{\mathbf{u}}_s - \mathbf{M}_{sm}\ddot{\mathbf{u}}_m \\ &= -\mathbf{M}_{ss}\left(-\mathbf{K}_{ss}^{-1}\mathbf{K}_{sm}\ddot{\mathbf{u}}_m\right) - \mathbf{M}_{sm}\ddot{\mathbf{u}}_m \\ &= \mathbf{M}_{ss}\mathbf{K}_{ss}^{-1}\mathbf{K}_{sm} - \mathbf{M}_{sm} \end{aligned} \tag{2.20}$$

$$\mathbf{M}_{sm} = \mathbf{M}_{ss}\mathbf{K}_{ss}^{-1}\mathbf{K}_{sm} \tag{2.21}$$

It is assumed that the $\mathbf{M}_{ss}\ddot{\mathbf{u}}_s$ terms are zero and that $\mathbf{M}_{ss}$ and $\mathbf{M}_{sm}$ are related as in (2.20) . The force transmission between the $\ddot{\mathbf{u}}_s$ and $\ddot{\mathbf{u}}_m$ dof is related only to the stiffnesses as denoted in Eq. (2.20), which is equivalent to the “static equilibrium” approximation.
Assuming Eq. (2.19) holds, the displacements vector $\mathbf{u}$ can be written in terms of $\mathbf{u}_m$ only

$$\mathbf{u} = \begin{bmatrix} \mathbf{u}_s \\ \hdashline \mathbf{u}_m \end{bmatrix} = \begin{bmatrix} -\mathbf{K}_{ss}^{-1}\mathbf{K}_{sm} \\ \hdashline \mathbf{I}_m \end{bmatrix} \mathbf{u}_m = \begin{bmatrix} \mathbf{T}_{sm} \\ \hdashline \mathbf{I} \end{bmatrix} \mathbf{u}_m = \mathbf{T}\mathbf{u}_m \tag{2.22}$$

Substitution of Eq.(2.22), with derivatives, into (2.15) yields

$$\mathbf{M}\,\mathbf{T}\,\ddot{\mathbf{u}}_{\mathrm{m}} + \mathbf{K}\,\mathbf{T}\,\mathbf{u}_{\mathrm{m}} = \mathbf{F} \tag{2.23}$$

Equation (2.23) still contains (s + m) dof, so premultiplication by $\mathbf{T}^{\mathrm{T}}$ is required to reduce to (m) dof and to return symmetry to the reduced mass and stiffness matrices

$$\left(\mathbf{T}^{\mathrm{T}}\mathbf{M}\,\mathbf{T}\right)\ddot{\mathbf{u}}_{\mathrm{m}} + \left(\mathbf{T}^{\mathrm{T}}\mathbf{K}\,\mathbf{T}\right)\mathbf{u}_{\mathrm{m}} = \mathbf{T}^{\mathrm{T}}\mathbf{F} \tag{2.24}$$

Rewriting Eq. (2.24) in a more compact form

$$\mathbf{M}^{*}\,\ddot{\mathbf{u}}_{\mathrm{m}} + \mathbf{K}^{*}\,\mathbf{u}_{\mathrm{m}} = \mathbf{F}^{*}_{\mathrm{m}} \tag{2.25}$$

Equation (2.25) is the final reduced equation of motion which can be solved for the displacements of type (m). Displacements of type (s), assuming static equilibrium, can then be solved for using Eq. (2.19).

$\mathbf{K}^{*}$ can be shown to be the same as that derived in the static condensation, Eq. (2.11)

$$\begin{aligned}\mathbf{K}^{*} &= \mathbf{T}^{\mathrm{T}}\mathbf{K}\ \mathbf{T}\\ &= \left[\left(\mathbf{T}^{\mathrm{T}}_{\mathrm{sm}}\mathbf{K}_{\mathrm{ss}} + \mathbf{k}_{\mathrm{ms}}\right) \;\vdots\; \left(\mathbf{T}^{\mathrm{T}}_{\mathrm{sm}}\mathbf{K}_{\mathrm{sm}} + \mathbf{K}_{\mathrm{mm}}\right)\right]\left[\begin{array}{c}\mathbf{T}_{\mathrm{sm}}\\ \hdashline \mathbf{I}\end{array}\right]\\ &= \mathbf{K}_{\mathrm{mm}} - \mathbf{K}_{\mathrm{ms}}\mathbf{K}^{-1}_{\mathrm{ss}}\mathbf{K}_{\mathrm{sm}}\end{aligned} \tag{2.26}$$

The reduced mass matrix becomes

$$\begin{aligned}\mathbf{M}^{*} &= \mathbf{T}^{\mathrm{T}}\mathbf{M}\ \mathbf{T}\\ &= \mathbf{M}_{\mathrm{mm}} - \mathbf{K}_{\mathrm{ms}}\mathbf{K}^{-1}_{\mathrm{ss}}\mathbf{M}_{\mathrm{sm}} - \mathbf{M}_{\mathrm{ms}}\mathbf{K}^{-1}_{\mathrm{ss}}\mathbf{K}_{\mathrm{sm}} + \mathbf{K}_{\mathrm{ms}}\mathbf{K}^{-1}_{\mathrm{ss}}\mathbf{M}_{\mathrm{ss}}\mathbf{K}^{-1}_{\mathrm{ss}}\mathbf{K}_{\mathrm{sm}}\end{aligned} \tag{2.27}$$

In the case of the reduced stiffness matrix, none of the structural complexity is lost since all elements of the original stiffness matrix contribute. However, in the reduced mass matrix, combinations of stiffness and mass elements appear. The results is that the eigenvalue problem is closely but not exactly preserved (Guyan, 1964).

2.4 Exact dynamic condensation

As shown in Section 1.4.2, the following equation results from a finite element analysis of linear system undergoing forced harmonic oscillations

$$\mathbf{D}(\omega)\mathbf{u} = \mathbf{F} \tag{2.28}$$

where

$$\mathbf{D}(\omega) = \mathbf{K} - \omega^2\mathbf{M} \tag{2.29}$$

D is the dynamic stiffness matrix, **K** and **M** are the stiffness and mass matrices, respectively.

These matrices may be functions of frequency depending on the method of analysis. $\mathbf{F}e^{i\omega t}$ and $\mathbf{u}e^{i\omega t}$ are the force excitation and displacement response vectors respectively. A system may be referred to an element, a substructure or to the overall system. Upon choosing a set of masters and slaves so that the slave coordinates are not subjected to driving forces, Eq. (2.28) is partitioned as

$$\left[\begin{array}{c|c} \mathbf{D}_{\mathrm{mm}} & \mathbf{D}_{\mathrm{ms}} \\ \hline \mathbf{D}_{\mathrm{sm}} & \mathbf{D}_{\mathrm{ss}} \end{array}\right] \left[\begin{array}{c} \mathbf{u}_{\mathrm{m}} \\ \hline \mathbf{u}_{\mathrm{s}} \end{array}\right] = \left[\begin{array}{c} \mathbf{F}_{\mathrm{m}} \\ \hline \mathbf{0} \end{array}\right] \tag{2.30}$$

Eliminating $\mathbf{u}_s$ from Eq. (2.30), the following equations are derived:

$$\mathbf{u}_{\mathrm{s}} = -\mathbf{D}_{\mathrm{ss}}^{-1}\mathbf{D}_{\mathrm{sm}}\mathbf{u}_{\mathrm{m}} \tag{2.31}$$

and

$$\mathbf{D}^{*}\mathbf{u}_{\mathrm{m}} = \mathbf{F}_{\mathrm{m}} \tag{2.32}$$

where

$$\mathbf{D}^{*} = \mathbf{D}_{\mathrm{mm}} - \mathbf{D}_{\mathrm{ms}}\mathbf{D}_{\mathrm{ss}}^{-1}\mathbf{D}_{\mathrm{sm}} \tag{2.33}$$

is the condensed dynamic stiffness matrix associated with the master dofs. From Eq. (2.33) it is clear that the dynamic condensation method is equal to the static condensation using the dynamic stiffness matrix instead of the classical static stiffness matrix (1.55).

Section 1.4.2 showed that the dynamic stiffness matrix **D** and the mass matrix **M** of an elastic system are related by the equation (Leung, 1978)

$$\mathbf{M}(\omega) = -\frac{\partial \mathbf{D}(\omega)}{\partial \omega^2} \tag{1.69}$$

where **M** and **D** correspond to the same set of coordinates. Differentiation of the dynamic stiffness matrix $\mathbf{D}^*$gives

$$\begin{aligned} \mathbf{M}^* &= -\frac{\partial \mathbf{D}^*(\omega)}{\partial \omega^2} \\ &= \mathbf{M}_{mm} - \mathbf{D}_{ms}\mathbf{D}_{ss}^{-1}\mathbf{M}_{sm} - \mathbf{M}_{ms}\mathbf{D}_{ss}^{-1}\mathbf{D}_{sm} + \mathbf{D}_{ms}\mathbf{D}_{ss}^{-1}\mathbf{M}_{ss}\mathbf{D}_{ss}^{-1}\mathbf{D}_{sm} \end{aligned} \tag{2.34}$$

which has the same form of the Guyan's results exposed in Eq. (2.27). In this case, apart from the approximation inherent in Eq. (2.28), the derivation is exact.

In the next section, in order to study the dynamic behaviour of a simple substructure extrapolated from a generic structure, exact dynamic condensation method is used. In fact this technique allows to derive the stiffness condensation parameters which must be assigned to the substructure, so that it can represents the global structure without loss of information.

2.5 Example 1: two-span beam

2.5.1 Exact dynamic condensation and natural frequencies

Considering the two span beam shown in Figure 2.1 and making use of the dynamic condensation method described above, the expression of the stiffness condensation parameter K_1, which represents the stiffness of the side span of the structure, is derived

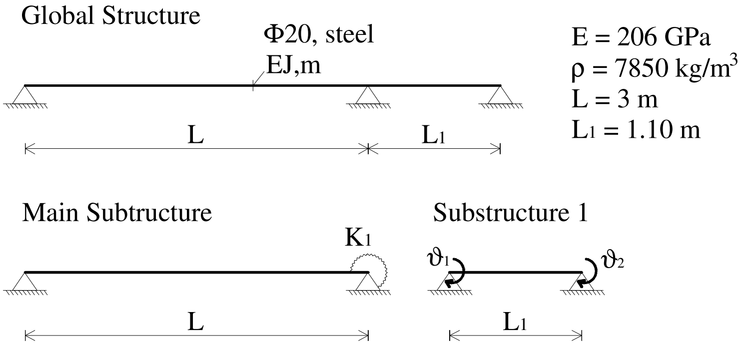

Figure 2.1 – Two-span beam and simplified model

The condensation parameter K_1 is the rotational dynamic stiffness of the substructure 1. This parameter is obtained applying the dynamic condensation method to the substructure 1 and condensing the two degrees of freedom θ_1 and θ_2 into the master dof θ_1. The dynamic stiffness matrix of substructure 1 is partitioned as in Eq. (2.35)

$$\mathbf{D}_1(\omega)=\frac{EJ}{\chi_1 L_1}\begin{array}{c}\begin{array}{cc}\theta_1 & \theta_2\end{array}\\ \left[\begin{array}{c|c}F_{2,1} & F_{1,1}\\ \hline F_{1,1} & F_{2,1}\end{array}\right]\end{array}=\left[\begin{array}{c|c}\mathbf{D}_{\mathrm{mm}} & \mathbf{D}_{\mathrm{ms}}\\ \hline \mathbf{D}_{\mathrm{sm}} & \mathbf{D}_{\mathrm{ss}}\end{array}\right] \tag{2.35}$$

where F_1 and F_2 are the stiffness coefficients derived in Section 1.4.2 and the subscript 1 indicates substructure 1. Making use of Eq. (2.33), K_1 takes the same form of the rotational stiffness of a simply supported beam with a moment in one end, obtained in Section 1.5.3 Eq. (1.88) without axial load influence ($q_1 = q_2 = \lambda$):

$$K_1(\omega)=\mathbf{D}_{\mathrm{mm}}-\mathbf{D}_{\mathrm{ms}}\mathbf{D}_{\mathrm{ss}}^{-1}\mathbf{D}_{\mathrm{sm}}=\frac{2EJ}{L_1}\frac{\lambda\sin\lambda\sinh\lambda}{\sin\lambda\cosh\lambda-\cos\lambda\sinh\lambda} \tag{2.36}$$

Hence, the dynamic stiffness matrix of the main substructure is

$$\mathbf{D}_{\mathrm{sub}}(\omega)=\begin{bmatrix}\dfrac{EJ}{\chi L}F_2 & \dfrac{EJ}{\chi L}F_1\\ \dfrac{EJ}{\chi L}F_1 & \dfrac{EJ}{\chi L}F_2+K_1\end{bmatrix} \tag{2.37}$$

As described in Section 2.4, the vanishing of the determinant of the dynamic stiffness matrix of the substructure $\mathbf{D}_{\mathrm{sub}}$ provides the natural frequencies of the global system:

$$\mathrm{Det}\left[\mathbf{D}_{\mathrm{sub}}(\omega)\right]=0\rightarrow\omega_{1,2,..,n} \tag{2.38}$$

It can be proved that the eigenvalues which satisfy Eq. (2.38) are also the natural frequencies of the dynamic stiffness matrix of the global structure:

$$\mathrm{Det}\left[\mathbf{D}_{\mathrm{sub}}(\omega_{1,2,..n})\right]=\mathrm{Det}\left[\mathbf{D}(\omega_{1,2,..n})\right]=0 \tag{2.39}$$

where $\mathbf{D}(\omega)$ is the dynamic stiffness matrix of the global structure (Eq. (2.40)), obtained by assembling the dynamic stiffness matrix of the two finite elements, one for each span.

$$\mathbf{D}(\omega)=\begin{bmatrix} \frac{EJ}{\chi L}F_2 & \frac{EJ}{\chi L}F_1 & 0 \\ \frac{EJ}{\chi L}F_1 & \frac{EJ}{\chi L}F_2+\frac{EJ}{\chi_1 L_1}F_{2,1} & \frac{EJ}{\chi_1 L_1}F_{1,1} \\ 0 & \frac{EJ}{\chi_1 L_1}F_{1,1} & \frac{EJ}{\chi_1 L_1}F_{2,1} \end{bmatrix} \tag{2.40}$$

The determinant of Eq. (2.37) or (2.40) represents the characteristic frequency equation of the structure. Hence, roots of the characteristic frequency equation are the natural frequencies of the global structure (Figure 2.2 and Table 2.1).

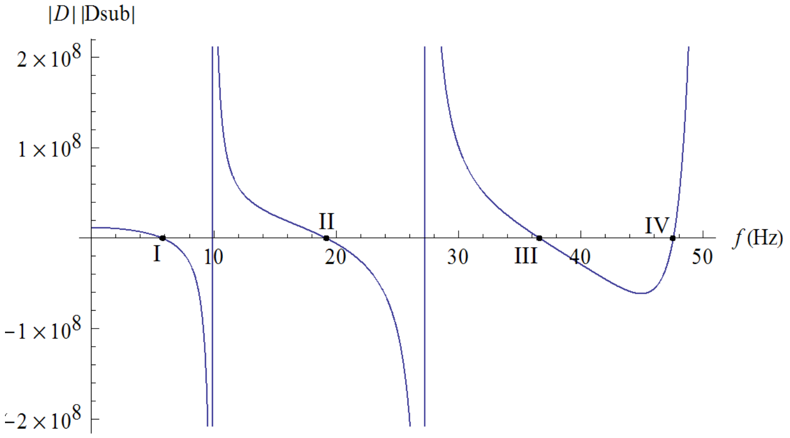

Figure 2.2 – Characteristic frequency equation of the system

Table 2.1 shows that, if the eigenvalue problem is solved by means of the classical static matrices (1.55) (1.56), 6 finite element are not sufficient to describe the dynamic behaviour of the structure. Otherwise, dynamic condensation method, provides the exact solution with 2 elements only for each span. To get to this result with the classical FEM, 48 finite elements are needed.

Method	Modal frequency [Hz]			
	I	II	III	IV
Dynamic Condensation (Exact) - 2 elements	5.952	19.677	37.546	48.738
Classical FEM - 6 finite elements	5.945	19.431	36.503	44.570
Classical FEM - 48 finite elements	5.952	19.677	37.546	48.738

Table 2.1 – First four modal frequencies of the structure

The condensation parameter K_1, Eq. (2.36), is a continuous function of natural frequency, so for any normal mode of the global structure it is possible to identify a specific value of this parameter, which represents the dynamic stiffness of the adjacent span. Otherwise, assuming a vibration frequency of the system, the expression of K_1 provides the value of the dynamic stiffness explicated by the adjacent (Table 2.2). It depends only on the geometrical and mechanical properties of adjacent span. Figure 2.3 show the plot of the condensation parameter K_1 versus frequency.

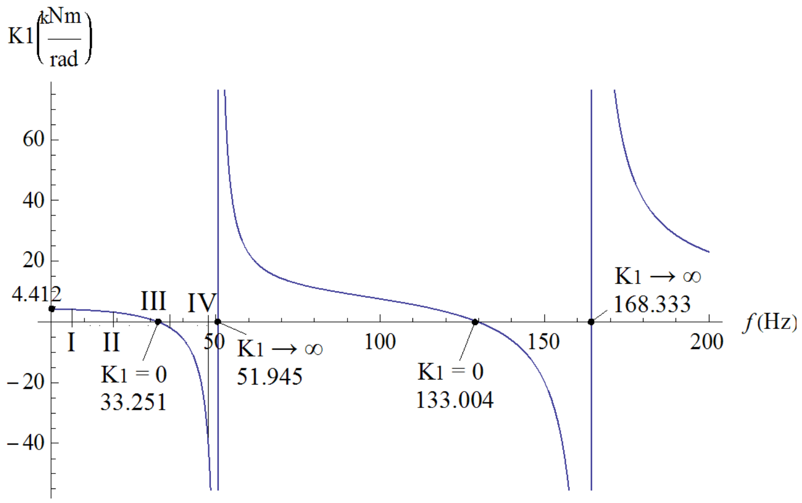

Figure 2.3 – Condensation parameter K_1 – frequency

Vibration mode	I	II	III	IV
Modal frequency f [Hz]	5.952	19.677	37.546	47.738
Condensation parameter K_1 [kNm/rad]	4.324	3.314	-2.446	-28.264

Table 2.2 – First four modal frequency of the structure

When frequency goes to zero, the condensation parameter K_1 of the adjacent span tends to the rotational static stiffness of the simply supported beam:

$$K_1(0) = \lim_{\omega \to 0} \frac{2EJ}{L_1} \frac{\lambda \sin\lambda \sinh\lambda}{\sin\lambda \cosh\lambda - \cos\lambda \sinh\lambda} = \frac{3EJ}{L_1} = 4.412 \text{ kNm/rad} \qquad (2.41)$$

Furthermore it is evident that values of frequency exist for which K_1 reaches zero and others for which it has singular points. The former are the modal frequencies for which the global system vibrates so that there is no transmission of bending moments between the main substructure and the adjacent one (substructure 1). If the central span had mechanical or geometrical characteristics for which the first or second vibration mode are, 33.251 Hz or 133.004 Hz (first two roots of the function $K_1(\omega)$), it would be as if the adjacent span did not exist and the main span would undergo a deflection shape as if it were isolated, Figure 2.4 a).

The frequencies for which K_1 is singular, i.e. 51.945 Hz and 168.333 Hz are reached when the system has mechanical or geometrical characteristics for which the flexural modal shape does not experiment rotation at the right support, e.g. the second modal frequency of the system with $L = L_1$, Figure 2.4 b).

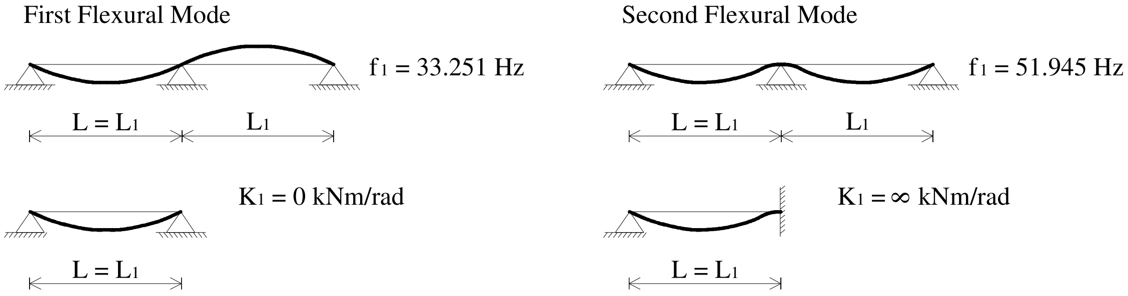

Figure 2.4 a), b) – Physical meaning of K_1 for $L = L_1$

From the plot of Figure 2.3 and Table 2.2 it's clear that K_1 can assume negative values, for example at the third and fourth normal modes. Nonetheless, it is possible to have a negative condensation parameter just on the first modal frequency. It depends only on the mechanical or geometrical characteristics of the structure. For instance, the plots in Figure 2.5 and 2.6 depict the relation between the condensation parameter K_1 and the length of the main span of the main structure. For each value of the length L, the system of the Figure 2.1 has a specific first frequency (Figure 2.5), which corresponds to a specific condensation parameter of the substructure 1 (Figure 2.6).

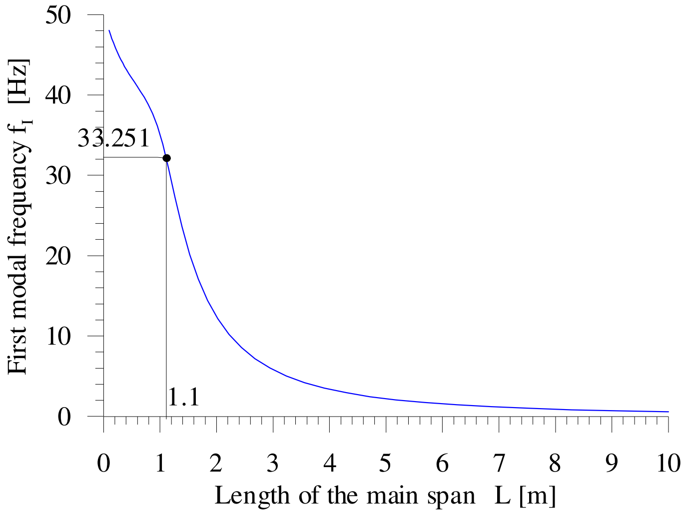

Figure 2.5 – First modal frequency vs. length of the main span

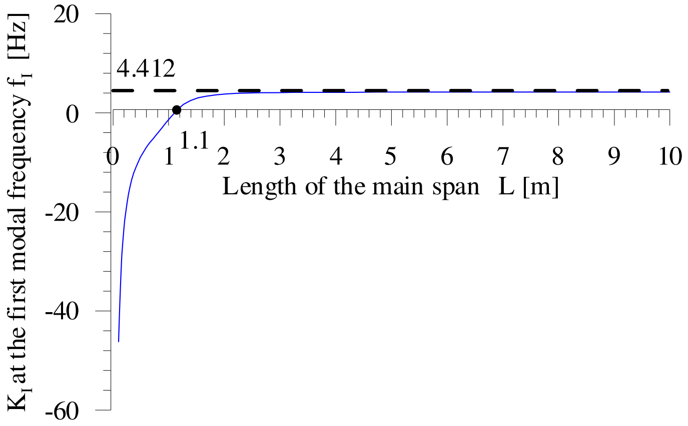

Figure 2.6 – K_1 at the first modal frequency vs. length of the main span

The plot in Figure 2.6 shows that if the span of the main substructure had the same length as the adjacent span L_1 = 1.1 m, K_1 would vanish and there would be no transmission of bending moment through the two spans. In this case, the system is perfectly symmetric (see Figure 2.4.a) and the first flexural mode shape experiments free rotation at the right support. Indeed, plot of Figure 2.5 shows that, for L_1 = 1.1 m, the first modal frequency is 33.251 Hz and this value is exactly the frequency for which the function $K_1(\omega)$ has the first root in the plot of Figure 2.3.

Now, it can be noted that an asymptote occurs at 51.945 Hz in the plot of $K_1(\omega)$ (Figure 2.3). This frequency corresponds to the second vibration mode of the symmetric system, for which the central support is clamped in the second flexural modal shape (Figure 2.4.b). Hence the dynamic stiffness of the section reaches infinity $K_1^{II}(f^{II} = 51.945 \text{ Hz}) \rightarrow \infty$, Figure 2.3.

Moreover, Figure 2.6 shows that K_1 takes negative values at the first modal frequencies when L_1 < 1.1 m. In this case, the first mode shape of the structure is governed by the longer right span. In particular, when the length L goes to zero, the rotational stiffness of the substructure 1 tends to infinity, because the global structure tends to the simply substructure 1 with clamped left end. Conversely, when L approach infinity, the first vibration frequency tends to zero, and the condensation parameter tends to the static stiffness of the substructure 1: $3EJ/L_1$ = 4.412 kNm/rad, as indicated by the horizontal asymptote in Figure 2.6.

2.5.2 Comparison between exact dynamic condensation and Guyan's reduction method

For the same structure of the previous section, exact dynamic condensation method and Guyan's reduction are now compared in terms of condensation parameter K_1.

Consider the substructure 1 in Figure 2.1, for which the dof θ_1 is assumed as master dof. Exact dynamic condensation (apex *ex*) yields Eq. (2.36) for the condensation parameter K_1^{ex}.

Guyan's dynamic condensation has been introduced in Section 2.3, where the condensed mass matrix and the condensed stiffness matrix have been derived (Eq. (2.26) and (2.27)). Making use of this equations to describe the substructure 1 of Figure 2.7, yield:

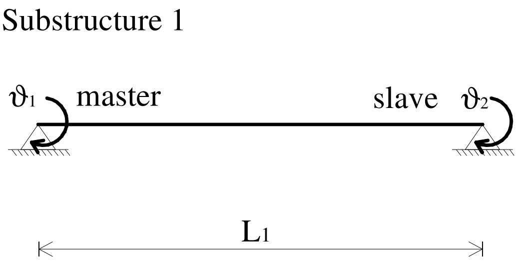

Figure 2.7 – Two-span beam and the simplified model

$$\mathbf{K}_1 = \left[\begin{array}{c|c} \mathbf{K}_{\mathrm{mm}} & \mathbf{K}_{\mathrm{ms}} \\ \hline \mathbf{K}_{\mathrm{sm}} & \mathbf{K}_{\mathrm{ss}} \end{array}\right] = \frac{EJ}{L_1}\left[\begin{array}{c|c} 4 & 2 \\ \hline 2 & 4 \end{array}\right]$$

$$\mathbf{K}_1^* = \mathbf{K}_{\mathrm{mm}} - \mathbf{K}_{\mathrm{ms}}\mathbf{K}_{\mathrm{ss}}^{-1}\mathbf{K}_{\mathrm{sm}} = \frac{3EJ}{L_1} \tag{2.42}$$

$$\mathbf{M} = \left[\begin{array}{c|c} \mathbf{M}_{\mathrm{mm}} & \mathbf{M}_{\mathrm{ms}} \\ \hline \mathbf{M}_{\mathrm{sm}} & \mathbf{M}_{\mathrm{ss}} \end{array}\right] = \frac{mL_1^3}{420}\left[\begin{array}{c|c} 4 & -3 \\ \hline -3 & 4 \end{array}\right]$$

$$\mathbf{M}^* = \mathbf{M}_{\mathrm{mm}} - \mathbf{K}_{\mathrm{ms}}\mathbf{K}_{\mathrm{ss}}^{-1}\mathbf{M}_{\mathrm{sm}} - \mathbf{M}_{\mathrm{ms}}\mathbf{K}_{\mathrm{ss}}^{-1}\mathbf{K}_{\mathrm{sm}} + \mathbf{K}_{\mathrm{ms}}\mathbf{K}_{\mathrm{ss}}^{-1}\mathbf{M}_{\mathrm{ss}}\mathbf{K}_{\mathrm{ss}}^{-1}\mathbf{K}_{\mathrm{sm}} = \frac{2mL_1^3}{105} \tag{2.43}$$

Hence, the condensed dynamic stiffness obtained from application of Guyan's reduction method (apex *G*) can be written as

$$K_1^G(\omega) = K_1^* - \omega^2 M_1^* = \frac{3EJ}{L_1} - \omega^2\frac{2mL_1^3}{105} \tag{2.44}$$

As described in Section 1.4.2, the use of the classical static matrices for the vibration problem of the Euler-Bernoulli beam represents a first order approximation of the exact method of the dynamic stiffness matrix. Hence, K_1^G is the first order approximation of the condensation parameter K_1^{ex}, Eq. (2.36).

In Figure 2.8 exact and Guyan's condensed dynamic stiffness, (Eq. (2.44) in solid line and Eq. (2.36) in dash line respectively) have been plotted versus frequency. It is evident how the Guyan's reduction method approximates the exact method in the neighbourhood of ω = 0. Furthermore Table 2.3 shows a comparison between the condensed stiffness K_1 estimated with the two methods at the first six modal frequencies of the structure. It is worth noting that Guyan's reduction method gives an acceptable value of K_1 only for the first two modes.

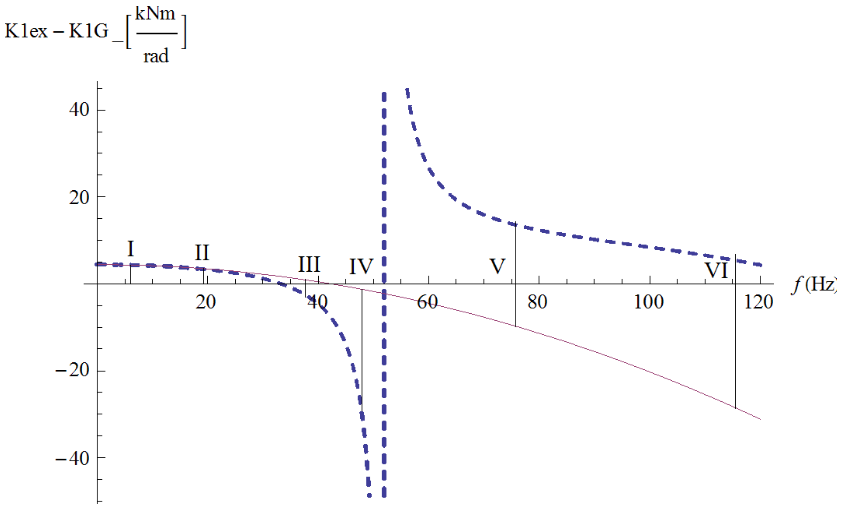

Figure 2.8 – Exact and approximated condensed dynamic stiffness vs. frequency

Vibration mode	I	II	III	IV	V	VI
Modal frequency f [Hz]	5.952	19.677	37.546	47.738	76.761	115.16
Condensation parameter Exact K_1^{ex} [kNm/rad]	4.324	3.314	-2.446	-28.264	13.233	5.473
Condensation parameter Guyan K_1^G [kNm/rad]	4.325	3.457	0.933	-1.213	-10.131	-28.322
Percent difference [%]	0.02	4.32	-	-	-	-

Table 2.3 – Comparison between Guyan's reduction method and exact element method

2.6 Example 2: two-span beam with lumped mass and axial force

2.6.1 Natural frequencies

In this section a more general problem is considered: a two-span beam with lumped mass and subjected to an axial force of compression, (Figure 2.9). The beam has one end simply supported and clamped the other.

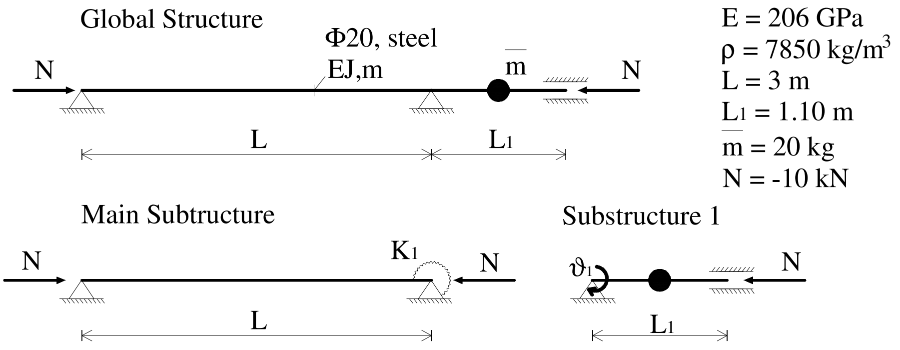

Figure 2.9 – Two-span beam and the simplified model

The spring K_1 is the dynamic stiffness of the end section rotation of the substructure 1. Since the substructure 1 has a single dof, the dynamic stiffness is represented by the element of position (2,2) in the dynamic stiffness matrix of the beam. Its expression is just obtained in Section 1.5.2, Eq. (1.83) .

The dynamic stiffness matrix of the main substructure with the rotational spring is

$$\mathbf{D}(\omega) = \begin{bmatrix} \frac{EJ}{\chi L} F_2 & \frac{EJ}{\chi L} F_1 \\ \frac{EJ}{\chi L} F_1 & \frac{EJ}{\chi L} F_2 + K_1 \end{bmatrix} \tag{2.45}$$

As described in the last section, the vanishing of the determinant of $\mathbf{D}(\omega)$ gives the modal frequencies of the global system (Figure 2.10).

It is worth noting that the first four natural frequencies of the structure have been searched in a larger range of frequency than the previous example. This happens because of the influence of the compression load which reduces the stiffness of the beam, even though it has a greater static stiffness. Table 2.4 summarizes the first four natural frequencies related to Figure 2.10.

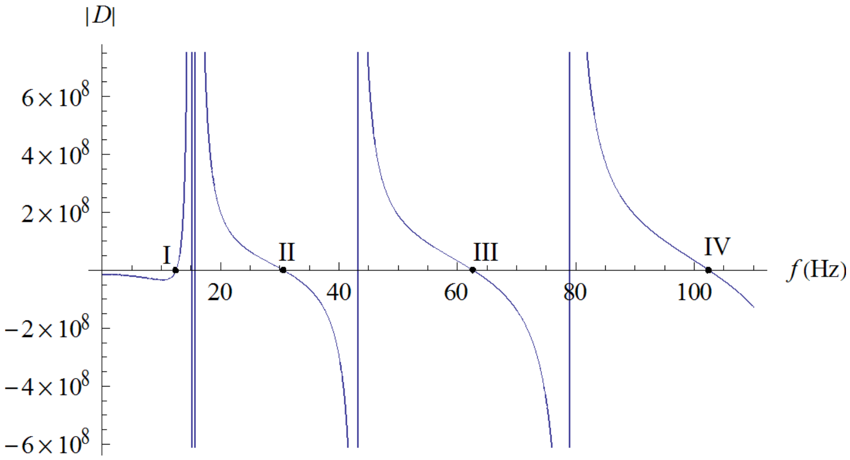

Figure 2.10 – Frequency equation of the system

Vibration Mode	I	II	III	IV
Modal frequency by Exact dynamic condensation 2 elements	12.483	30.631	62.666	102.504

Table 2.4 – First four modal frequency of the structure

2.6.2 Condensed dynamic stiffness versus frequency

Figure 2.11 shows the relation between the dynamic stiffness of the substructure 1, K_1, Eq. (1.83), and the vibration frequencies. The considerations made in the last section also apply here. Hence, the roots of Eq. (1.83) represent the natural frequencies of a symmetric vibrating system, in which substructure 1 does not transmit bending moment to the main substructure.

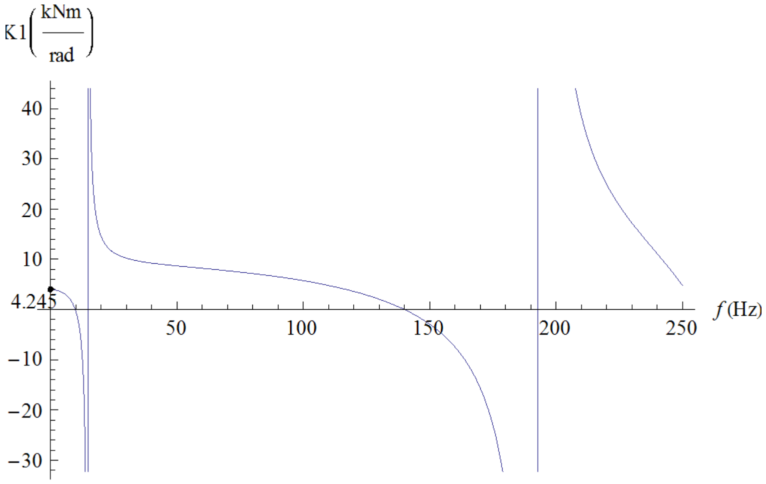

Figure 2.11 – Condensation parameter K_1 vs. frequency

The vertical asymptotes represent particular geometrical or mechanical characteristics of the system for which the condensation parameter K_1 natural approaches infinity: e.g. when the main span tends to zero (left side of singularity) or when the main substructure has such a length that the two spans of the structure vibrate symmetrically without rotation of the common section (right side of singularity). For this example these critical values of main span length are not so evident because of the axial load influence and lumped mass in span.

2.6.3 Condensed dynamic stiffness versus axial load

2.6.3.1 Static case

Figure 2.11 shows that, when the frequency goes to zero, the condensation parameter K_1 tends to the rotational static stiffness of the clamped beam with the effects of the compression force

$$K_1(0,N) = \lim_{\omega\to 0} K_1(\omega,N) = \frac{EJ}{2L_1}\,\frac{\sqrt{n}\,\mathrm{csch}\sqrt{\frac{n}{2}}\left(\sqrt{n}\cosh\sqrt{n} - \sinh\sqrt{n}\right)}{\sqrt{n}\cosh\sqrt{\frac{n}{2}} - 2\sinh\sqrt{\frac{n}{2}}} \tag{2.46}$$

$$K_1(0,-10000) = 4.245\ kNm/rad$$

which is the value of the intercept of the plot on the vertical axis. Eq. (2.46) is equivalent to the well known equation of static stiffness with second order effects (Bazant and Cedolin 1991):

$$K_1(0,N) = \frac{4EJ}{L_1}\,\frac{3I_1}{4I_1^2 - I_2^2} \tag{2.47}$$

where

$$I_1 = -\frac{3}{\sqrt{n}L_1}\left(\frac{1}{\sqrt{n}L_1} - \frac{1}{\tanh\sqrt{n}L_1}\right) \qquad I_2 = \frac{6}{\sqrt{n}L_1}\left(\frac{1}{\sin\sqrt{n}L_1} - \frac{1}{\sqrt{n}L_1}\right) \tag{2.48}$$

It is interesting to plot the Eq. (2.46) respect to the axial force N (Figure 2.12).

It is clear that, if the axial force is a tensile stress, it increases the stiffness of the beam and, for higher values of N, K_1 increases until the yielding of material. For compression stress the graph shows singularity points, which represent the Eulerian critical loads of substructure 1 with clamped-clamped restraint (Figure 2.13). So the expression of K_1 Eq. (2.46) holds information about the buckling loads of the beam. The vertical asymptotes in Figure 2.12 depict the first four critical loads (Table 2.5).

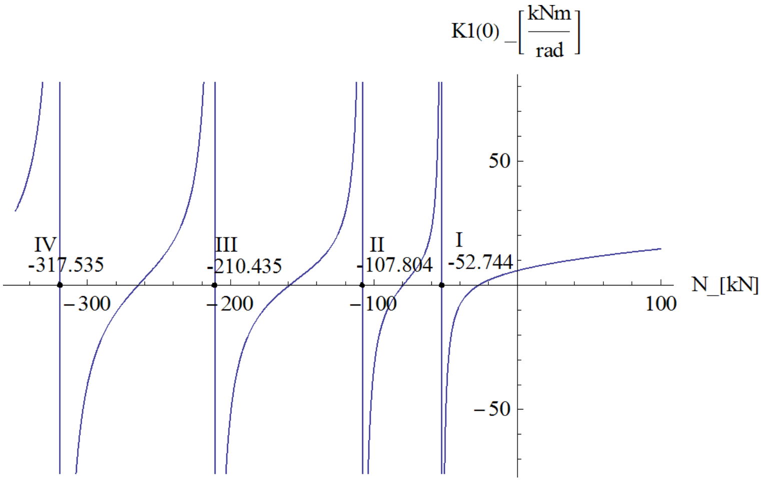

Figure 2.12 – Static stiffness $K_1(0)$ vs axial load

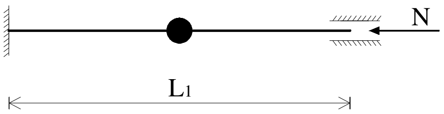

Figure 2.13 – Model of substructure 1with clamped ends

Vibration Mode	I	II	III	IV
Eulerian critical loads [kN]	-52.744	-107.804	-210.435	-317.535

Table 2.5 – First four Eulerian critical load of the substructure 1 doubly clamped.

2.6.3.2 Dynamic case

For the same model of the previous section, the relationship between the condensation parameter K_1, as function of natural frequencies of the global system, and the axial force assigned is derived. This relationship will be useful to understand the experimental data presented in the next chapter.

The maximum axial load may attain the material yielding. However, the maximum tensile load adopted during the experimental tests was about 40 kN. The minimum axial load can be the Eulerian critical load of the system, which is obtained from the vanishing of the modal frequencies of the frame. In Figure 2.14 the roots of the determinant of the dynamic stiffness matrix (Eq. (2.45) and (1.88)) are plotted versus different values of axial load. The natural frequencies of the system vanish at about

N_I = – 3.07 kN and N_II = – 8.98 kN, which are exactly the first two Eulerian critical loads of the frame.

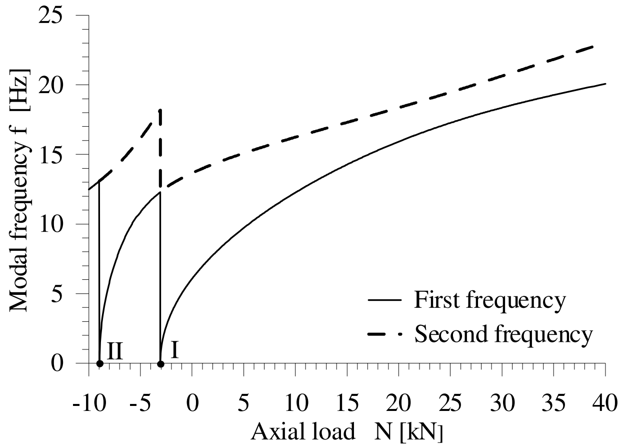

Figure 2.14 – Modal frequency of the system vs. axial load

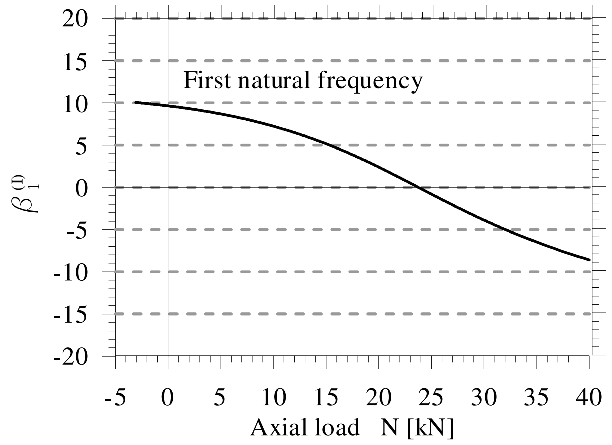

Figure 2.15 – Nondimensional condensation parameter $\beta_1^{(I)}$ vs. axial load

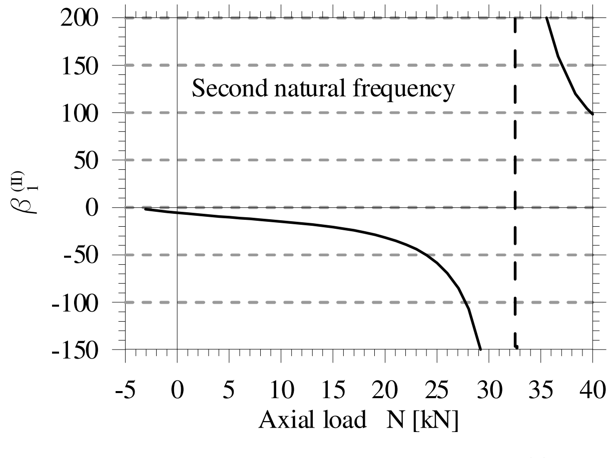

Figure 2.16 – Nondimensional condensation parameter $\beta_1^{(II)}$ vs. axial load

Figure 2.15 and Figure 2.16 show the nondimensional condensation parameter $\beta_1^{(I)}(N) = K_1(\omega,N)L/EJ$ evaluated at the first and the second natural frequencies of the system, $\beta_1^{(I)}(N) = \beta_1(\omega_1,N)$ and $\beta_1^{(II)}(N) = \beta_1(\omega_2,N)$ respectively.

The coefficient $\beta_1^{(I)}$ is a continuous function of the axial load and reaches negative values for axial load higher than about 25 kN. The coefficient $\beta_1^{(II)}$ assumes negative values up to vertical asymptote close to $N = 33$ kN. This happens because the two spans vibrate almost symmetrically for each load step and they vibrate exactly symmetrically for the value of axial load for which the vertical asymptote occurs. In this ideal configuration the right span clamps the left one because of the stiffness variation due to the axial load, while in the previous example this phenomenon was produced by a length variation of the main span.

2.7 Example 3: substructuring

Consider the system shown in Figure 2.17: a simply supported beam subjected to a tensile axial load. In order to consider the left part of the span as isolated, the condensation parameter matrix $\mathbf{K}_1$, which reproduces the contribution of the right part of the beam, has to be derived. In this example the dynamic condensation method has been used differently than in previous examples.

The global structure is divided in two finite elements and four dofs are considered as shown in Figure 2.17. Modelling the left part of the beam with only one finite element, the master dofs are the two rotations θ_1, θ_2 and translation v_2.

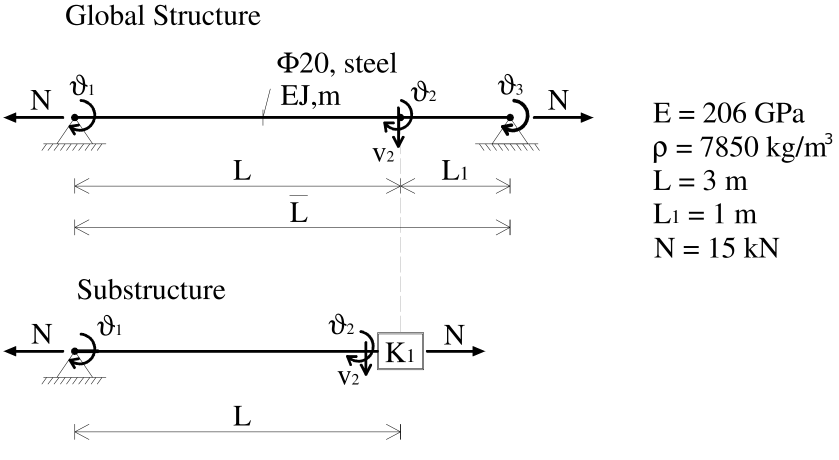

Figure 2.17 – Simply supported beam and the corresponding substructure

The dynamic stiffness matrix of the global structure is

$$\mathbf{D}(\omega)=\begin{array}{c}\begin{array}{cccc}\theta_1 & \theta_2 & v_2 & \theta_3\end{array}\\ \left[\begin{array}{ccc|c}
\frac{EJ}{\chi L}F_2 & -\frac{EJ}{\chi L^2}F_3 & \frac{EJ}{\chi L}F_1 & 0\\
-\frac{EJ}{\chi L^2}F_3 & \frac{EJ}{\chi L^3}F_6+\frac{EJ}{\chi_1 L_1^3}F_{6,1} & -\frac{EJ}{\chi L^2}F_4+\frac{EJ}{\chi_1 L_1^2}F_{4,1} & \frac{EJ}{\chi_1 L_1^2}F_{3,1}\\
\frac{EJ}{\chi L}F_1 & -\frac{EJ}{\chi L^2}F_4+\frac{EJ}{\chi_1 L_1^2}F_{4,1} & \frac{EJ}{\chi L}F_2+\frac{EJ}{\chi_1 L_1}F_{2,1} & -\frac{EJ}{\chi_1 L_1^2}F_{1,1}\\
\hline
0 & \frac{EJ}{\chi_1 L_1^2}F_{3,1} & \frac{EJ}{\chi_1 L_1}F_{1,1} & \frac{EJ}{\chi_1 L_1}F_{2,1}
\end{array}\right]\end{array}$$

(2.49)

$$=\left[\begin{array}{c|c}\mathbf{D}_{\mathrm{mm}} & \mathbf{D}_{\mathrm{ms}}\\ \hline \mathbf{D}_{\mathrm{sm}} & \mathbf{D}_{\mathrm{ss}}\end{array}\right]$$

The dynamic condensation of **D** yields a 3x3 dynamic stiffness matrix of the substructure

$$\mathbf{D}_{\mathrm{sub}}(\omega)=\mathbf{D}^{*}_{\mathrm{mm}}(\omega)=\mathbf{D}_{\mathrm{mm}}-\mathbf{D}_{\mathrm{ms}}\mathbf{D}_{\mathrm{ss}}^{-1}\mathbf{D}_{\mathrm{sm}} \tag{2.50}$$

The stiffness matrix of the substructure $\mathbf{D}_{\mathrm{sub}}$ can also be seen as the assembly of the stiffness matrix of the substructure $\mathbf{D}_0$ and the condensation parameter matrix $\mathbf{K}_1$:

$$\mathbf{D}_{\mathrm{sub}}(\omega)=\mathrm{assemble}\{\mathbf{D}_0+\mathbf{K}_1\}=\left[\begin{array}{ccc}
\frac{EJ}{\chi L}F_2 & -\frac{EJ}{\chi L^2}F_3 & \frac{EJ}{\chi L}F_1\\
-\frac{EJ}{\chi L^2}F_3 & \frac{EJ}{\chi L^3}F_6+\mathbf{K}_1(1,1) & -\frac{EJ}{\chi L^2}F_4+\mathbf{K}_1(1,2)\\
\frac{EJ}{\chi L}F_1 & -\frac{EJ}{\chi L^2}F_4+\mathbf{K}_1(1,2) & \frac{EJ}{\chi L}F_2+\mathbf{K}_1(2,2)
\end{array}\right]$$

(2.51)

Therefore, condensation parameter matrix $\mathbf{K}_1$ may be obtained by the difference between the condensed stiffness matrix $\mathbf{D}_{\mathrm{sub}}$ (2.50) and the stiffness matrix of the substructure $\mathbf{D}_0$:

$$\mathbf{D}_{\text{sub}} - \mathbf{D}_0 = \left[\begin{array}{c|c} \mathbf{0} & \mathbf{0} \\ \hline \mathbf{0} & \mathbf{K}_1 \end{array}\right] = \left[\begin{array}{c|cc} 0 & 0 & 0 \\ \hline 0 & \mathbf{K}_1(1,1) & \mathbf{K}_1(1,2) \\ 0 & \mathbf{K}_1(2,1) & \mathbf{K}_1(2,2) \end{array}\right] \tag{2.52}$$

where the components of $\mathbf{K}_1$ take the forms

$$\mathbf{K}_1(1,1) = \frac{EJ}{L_1^3} \frac{q_1 q_2 \left(q_1^2 + q_2^2\right) \cos q_1 \cosh q_2}{q_2 \sin q_1 \cosh q_2 - q_1 \cos q_1 \sinh q_2} \tag{2.53}$$

$$\mathbf{K}_1(1,2) = \mathbf{K}_1(2,1) = \frac{EJ}{L_1^2} \frac{q_1 q_2 \left(q_1 \sin q_1 \cosh q_2 + q_2 \cos q_1 \sinh q_2\right)}{q_2 \sin q_1 \cosh q_2 - q_1 \cos q_1 \sinh q_2} \tag{2.54}$$

$$\mathbf{K}_1(2,2) = \frac{EJ}{L_1} \frac{\left(q_1^2 + q_2^2\right) \sin q_1 \sinh q_2}{q_2 \sin q_1 \cosh q_2 - q_1 \cos q_1 \sinh q_2} \tag{2.55}$$

The diagonal coefficients represent translational and rotational springs, the off-diagonal coefficient can be seen as a mixed spring that describes the coupling between vertical displacement v and bending moment or rotation θ and shear force.

Hence, describing the system with the dynamic stiffness matrix (2.51) is equivalent to using a single finite element of length $\overline{L} = L + L_1$ for the whole structure, whose dynamic stiffness matrix is:

$$\overline{\mathbf{D}}(\omega) = \frac{EJ}{\chi \overline{L}^3} \begin{array}{c} \begin{array}{cc} \theta_1 & \theta_3 \end{array} \\ \begin{bmatrix} F_2 \overline{L}^2 & F_1 \overline{L}^2 \\ F_1 \overline{L}^2 & F_2 \overline{L}^2 \end{bmatrix} \end{array} \tag{2.56}$$

In fact, as shown in Figure 2.18, the vanishing of the determinants of $\mathbf{D}_{\text{sub}}(\omega) = \text{assemble}\{\mathbf{D}_0 + \mathbf{K}_1\}$ (Eq. (2.51) in solid line) and $\overline{\mathbf{D}}$ (Eq. (2.56) in dash line) provides the same natural frequencies (Table 2.6).

Vibration mode	I	II	III	IV
Dynamic Condensation (Exact)	10.068	21.939	36.980	56.030

Table 2.6 – Roots of the characteristic frequency equation of the system

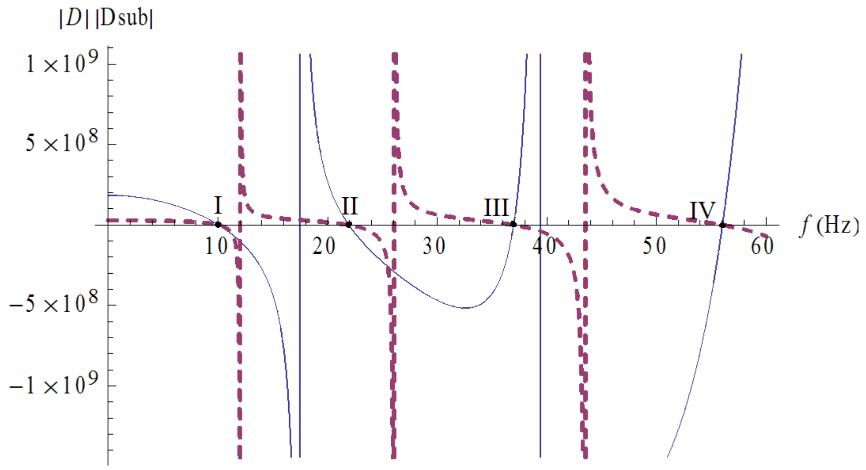

Figure 2.18 - Frequency equation of the main substructure, $\mathbf{D}_{\text{sub}}$.

For each modal frequency, the condensation parameter matrix $\mathbf{K}_1$, Eq. (2.52), are reported in Table 2.7. The generic element $K_1{}^i$ represents the condensation parameter contribution of the right side of the span for i –th normal mode.

Mode I	Mode II
$\mathbf{K}_1^{(\text{I})} = \begin{bmatrix} 17.524\,\text{kN/m} & 6.379\,\text{kN/rad} \\ 6.379\,\text{kN} & 6.915\,\text{kNm/rad} \end{bmatrix}$	$\mathbf{K}_1^{(\text{II})} = \begin{bmatrix} -0.239\,\text{kN/m} & 3.763\,\text{kN/rad} \\ 3.763\,\text{kN} & 6.448\,\text{kNm/rad} \end{bmatrix}$

Mode III	Mode IV
$\mathbf{K}_1^{(\text{III})} = \begin{bmatrix} -48.737\,\text{kN/m} & -3.759\,\text{kN/rad} \\ -3.759\,\text{kN} & 5.072\,\text{kNm/rad} \end{bmatrix}$	$\mathbf{K}_1^{(\text{IV})} = \begin{bmatrix} -212.131\,\text{kN/m} & -32.231\,\text{kN/rad} \\ -32.231\,\text{kN} & -0.400\,\text{kNm/rad} \end{bmatrix}$

Table 2.7 – Condensation parameter matrix $\mathbf{K}_1$.

2.8 Conclusions

In this chapter, the exact dynamic condensation method has been presented (Leung 1978). It gives the exact condensation parameters to be assigned to the dynamic stiffness matrix of the substructures of interest. Vice versa, Guyan's reduction method provides only a first order approximation of them (Guyan 1964).

For each examples, the analytical equations of the condensation parameters and its relation with axial force or frequency has been derived. These examples represent the basis to understand the end stiffness experimental results obtained in the next chapters.

3

Static and dynamic algorithms for axial load identification of frames on rigid supports

3.1 Introduction

The dynamic behaviour of a generic member belonging to a structure can be modelled as a substructure provided that boundary conditions are correctly assigned (Leung 1978). In Chapters 1 and 2, the analytical bases to model such a beam have been given. This chapter proposes two axial load identification methods of beam on rigid supports, which make use of dynamic and static tests.

The first one is based on the procedure developed by Tullini and Laudiero (2008), which shows that, if geometric and elastic properties of the beam are known, the axial force and the flexural stiffness of the end constraints can be deduced by one vibration frequency and three components of the corresponding mode shape. Moreover, a simple relation, irrespective of boundary conditions, between mode shape displacements and axial resultant is determined. In Section 3.2.3 a new formulation of the limit curves which bound the admissible data conditions for a physically correct identification of the unknown parameters is given. Validation of this technique was obtained by laboratory tests having many control point positions and with lumped mass-in-span. The dynamic tests were performed through pulse tests and the data analysis made use of peak picking method (PPM, Ewins 1984) and pole/residue model identification (PRMI, Balmés 1997).

Static procedures are restricted to supported beam and consists in the measure of the displacements of three instrumented sections located at the quarters of the beam, due to the application of a vertical force. An equation similar to the transcendental equation of the dynamic procedure is obtained, together with two equations for the evaluation of the flexural end stiffness. Laboratory tests are performed to validate the analytical results.

3.2 Axial load identification by means of dynamic tests

The identification method proposed hereafter for the axial load identification of Euler-Bernoulli beam assumes geometric and elastic properties as known parameters. Making use of any natural frequency and of three displacement components of the corresponding mode shape, both axial loads and stiffness of end flexural springs of a beam subjected to tensile or compression forces can easily be obtained. Moreover, relations between mode shape displacements and axial resultants are determined. In Section 3.2.1 and 3.2.2, some basic results suggest by Tullini and Laudiero (2008) are reported.

3.2.1 Governing equations

The reference model is constituted by a simply supported prismatic beam of length *L*, constrained by two end elastic-springs with k_0 and k_1 flexural stiffness, subjected to an axial resultant *N* (positive sign is assigned to tensile forces). Young's modulus *E*, mass per unit length *m* and cross-section second area moment *J* are assumed to be constant, and known as well (Figure 3.1).

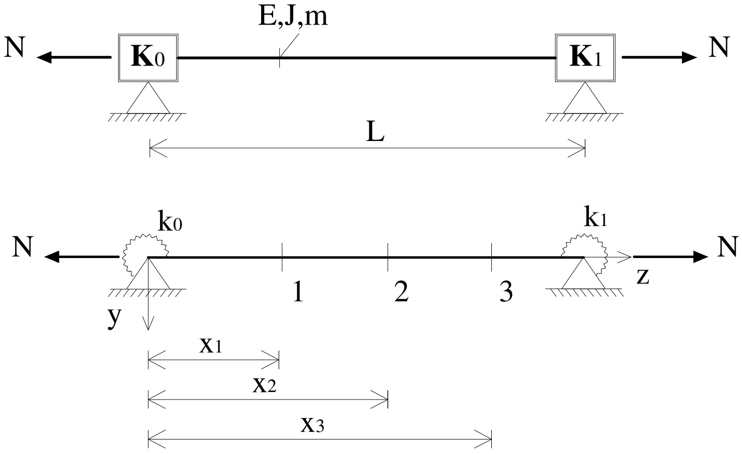

Figure 3.1 – Beam with end flexural constraints and location of the instrumented sections

The model in Figure 3.1 is a particular case of the more general one presented in Section 1.3.1, where the contribution of lumped mass in-span and the end forces are not considered, and the condensation parameter matrices reduce to the stiffness k_0 and k_1:

$$\mathbf{K}_0(\omega)=\begin{bmatrix}0 & 0\\ 0 & k_0(\omega)\end{bmatrix} \qquad \mathbf{K}_1(\omega)=\begin{bmatrix}0 & 0\\ 0 & k_1(\omega)\end{bmatrix} \tag{3.1}$$

Making use of the nondimensional coordinate $z = x/L$ and neglecting both rotary inertia and shear deformation, circular frequencies ω and vibration mode $v(z)$ are ruled by the eigenvalue problem presented in Eq. (1.33):

$$v''''(z)-nv''(z)-\lambda^4 v(z)=0 \tag{3.2}$$

with boundary conditions (1.43) that reduce to:

$$\begin{cases} v(0)=0\\ v''(0)-\beta_0 v'(0)=0\\ v(1)=0\\ v''(1)+\beta_1 v'(1)=0 \end{cases} \tag{3.3}$$

where prime means derivation with respect to z and

$$\beta_0=\frac{k_0 L}{EJ} \qquad \beta_1=\frac{k_1 L}{EJ} \qquad n=\frac{NL^2}{EJ} \qquad \lambda^4=\frac{mL^4\omega^2}{EJ} \tag{3.4}$$

Solution of Eq. (3.2) was given by Eq. (1.38):

$$v(z)=C_1\cos q_1 z+C_2\sin q_1 z+C_3\cosh q_2 z+C_4\sinh q_2 z \tag{3.5}$$

where

$$q_1^2=\frac{1}{2}\left(\sqrt{n^2+4\lambda^4}-n\right) \qquad q_2^2=\frac{1}{2}\left(\sqrt{n^2+4\lambda^4}+n\right)=q_1^2+n \tag{3.6}$$

Boundary conditions (3.3) furnish integration constants $C_1 - C_4$ and q_1, respectively.

3.2.2 Valuation of parameters

In order to identify the axial load N and the stiffness k_0 and k_1 of the end flexural constraints, knowledge is required of one vibration frequency and the corresponding mode shape at three locations coordinates x_1, x_2 and x_3 (Fig. 3.1). With reference to the nondimensional coordinate $z = x/L$, three displacements are determined and denoted by $v_i = v(x_i)$ for $i = 1,2,3$. Hence, constants $C_1 - C_4$ can be determined to the accuracy of a constant and the mode shape (3.5) is finally obtained. In fact, substituting Eq. (3.5) into the first boundary condition Eqs. (3.3) yields $C_3 = -C_1$ and the same Eq. (3.5) reduces to

$$v(x) = C_1 (\cos q_1 x - \cosh q_2 x) + C_2 \sin q_1 x + C_4 \sinh q_2 x \tag{3.7}$$

Hence, the following linear equation system is obtained:

$$\begin{bmatrix} \cos q_1 x_1 - \cosh q_2 x_1 & \sin q_1 x_1 & \sinh q_2 x_1 \\ \cos q_1 x_2 - \cosh q_2 x_2 & \sin q_1 x_2 & \sinh q_2 x_2 \\ \cos q_1 x_3 - \cosh q_2 x_3 & \sin q_1 x_3 & \sinh q_2 x_3 \end{bmatrix} \begin{bmatrix} C_1 \\ C_2 \\ C_4 \end{bmatrix} = \begin{bmatrix} v_1 \\ v_2 \\ v_3 \end{bmatrix} \tag{3.8}$$

Coefficient C_1, C_2 and C_4 are linear functions of the three (experimental) amplitudes v_1, v_2, v_3, and depend on the unknown parameter n and on constant λ through coefficients q_1 and q_2 reported in Eqs. (3.6). In its turn, λ depends on the experimental circular frequency ω. By imposing the third boundary condition Eqs. (3.3), the following transcendental equation is obtained, to be solved for the unknown constant n:

$$C_1(n,\lambda)(\cos q_1(n,\lambda) - \cosh q_2(n,\lambda)) + C_2(n,\lambda)\sin q_1(n,\lambda) + C_4(n,\lambda)\sinh q_2(n,\lambda) = 0 \tag{3.9}$$

Finally, the second and the fourth boundary conditions Eq. (3.3) yield coefficients β_0 and β_1:

$$\beta_0 = \frac{v''(0)}{v'(0)} = -\frac{(\mathrm{q}_1^2 + \mathrm{q}_2^2) C_1}{\mathrm{C}_2 q_1 + \mathrm{C}_4 q_2} \tag{3.10}$$

$$\beta_1 = -\frac{v''(1)}{v'(1)} = \frac{(\mathrm{q}_1^2 + \mathrm{q}_2^2)(C_1 \cos q_1 + C_2 \sin q_1)}{-C_1 (q_1 \sin q_1 + q_2 \sinh q_2) + C_2 q_1 \cos q_1 + C_4 q_2 \cosh q_2} \tag{3.11}$$

The above formulation can be simplified if control points are assumed at sections having nondimensional coordinates $z_1 = 1/4$, $z_2 = 1/2$ and $z_3 = 3/4$. In this case, if the mid-section does not coincide with a node of the assumed mode shape, i.e. if $v_2 \neq 0$, Eqs. (3.9) - (3.11), respectively, yield

$$\frac{v_1 + v_3}{v_2} = \frac{1 + 2\cos(q_1/4)\cosh(q_2/4)}{\cos(q_1/4) + \cosh(q_2/4)} \tag{3.12}$$

$$\beta_0 = \left(q_1^2 + q_2^2\right)\frac{a(v_1/v_2) - b}{c(v_1/v_2) - d} \qquad \beta_1 = \left(q_1^2 + q_2^2\right)\frac{a(v_3/v_2) - b}{c(v_3/v_2) - d} \tag{3.13}$$

where constants a, b, c and d are given by the following relations:

$$\begin{aligned}
a &= \sin q_1 \sinh\frac{q_2}{2} - \sin\frac{q_1}{2}\sinh q_2 \\
b &= \sin q_1 \sinh\frac{q_2}{4} - \sin\frac{q_1}{4}\sinh q_2 \\
c &= c_1 + c_2 \\
c_1 &= \left(\sinh\frac{q_2}{2} + \cos q_1 \sinh\frac{q_2}{2} - \cos\frac{q_1}{2}\sinh q_2\right) + \\
c_2 &= q_2\left(\sin\frac{q_1}{2} - \sin q_1 \cosh\frac{q_2}{2} + \sin\frac{q_1}{2}\cosh q_2\right) \\
d &= d_1 + d_2 \\
d_1 &= q_1\left(\cos q_1 \sinh\frac{q_2}{4} + \sinh\frac{3q_2}{4} - \cos\frac{q_1}{4}\sinh q_2\right) \\
d_2 &= q_2\left(\sin\frac{q_1}{4}\cosh q_2 + \sin\frac{3q_1}{4} - \sin q_1 \cosh\frac{q_2}{4}\right)
\end{aligned} \tag{3.14}$$

Regardless of any boundary conditions, the transcendental equation (3.12) provides values of n corresponding to any (experimental) value of λ . Moreover, if the first mode shape gives $v_1 = v_3$ or the second mode shape shows $v_2 = 0$, the symmetric boundary conditions are ascertained.

3.2.3 Particular case of end constraint stiffness

Figure 3.3 shows the plot of ratio $(v_1 + v_3)/2v_2$ versus λ for both positive and negative values of n. In particular, dotted lines represent the graph of Eq. (3.12) for $n = -4\pi^2, -\pi^2, 0, 10, 100, 1000, 10000$.

It is to be noted that the first minimum value for n corresponds to the first Eulerian critical load of a fully clamped beam ($\beta_0 = \beta_1 = \infty$) having nondimensional value $n = -4\pi^2$ and mode shape:

$$v(x) = C(1 - \cos 2\pi z) \tag{3.15}$$

In fact, Eq. (3.15) yields $(v_1 + v_3)/2v_2 = 0.5$ and, consequently, the first vibration frequency vanishes for the couple $[n,(v_1+v_3)/2v_2] = [0, 0.5]$. It is reasonable to assume that couples $[n, \lambda]$ can not exist beyond the curve corresponding to $n = -4\pi^2$ (lower solid line in Figure 3.3 for $\lambda < 11$). Moreover, all the curve are bonded by the line $(v_1 + v_3)/2v_2 = 1$ (upper solid line in Figure 3.2). Hence, all physical data points must lie between these two curves and the envelope curve of the minima of Eq. (3.12) (lower solid line in Figure 3.3 for $\lambda > 11$.

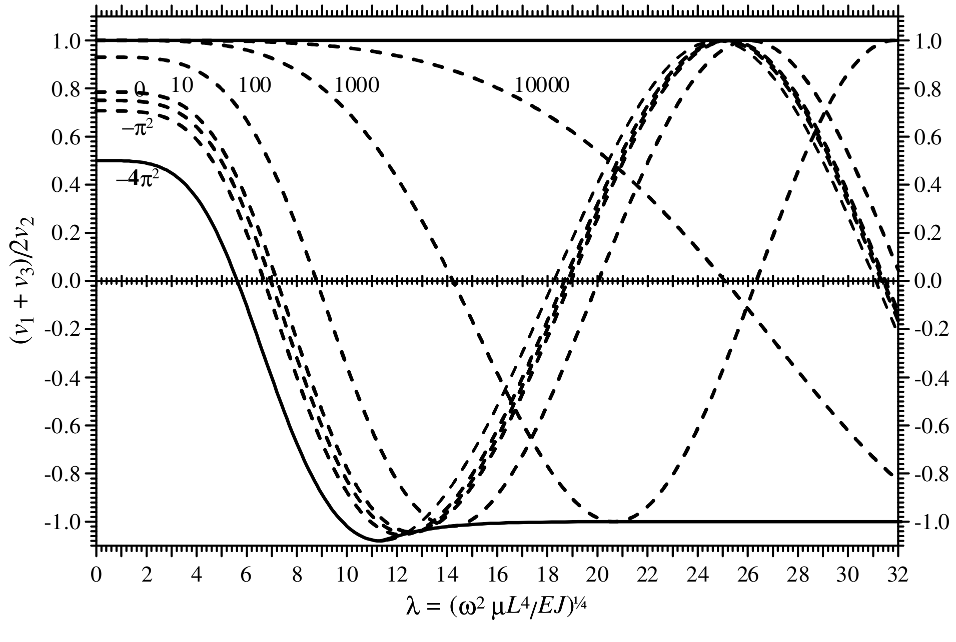

Figure 3.2 – Ratio $(v_1 + v_3)/2v_2$ versus λ for some given values of n

In order to find narrow admissible regions in the plane $\lambda - (v_1 + v_3)/2v_2$, the limit situation of clamped-clamped and simply supported beams are analysed. Rearranging Eqs. (3.13), alternative relations for mode shape amplitudes ratio can be obtained:

$$\frac{v_1}{v_2} = \frac{\left(q_1^2 + q_2^2\right)b - d\,\beta_0}{\left(q_1^2 + q_2^2\right)a - c\beta_0}, \quad \frac{v_3}{v_2} = \frac{\left(q_1^2 + q_2^2\right)b - d\,\beta_1}{\left(q_1^2 + q_2^2\right)a - c\beta_1} \tag{3.16}$$

Equating the sum of Eqs. (3.16) to the right-hand side of Eq. (3.12) and making use of Eqs. (3.14) yield the frequency characteristic equation, in the form

$$\begin{aligned}&\left(q_1^2+q_2^2\right)^2\sin q_1\sinh q_2+\left(\beta_0+\beta_1\right)\left(q_1^2+q_2^2\right)\left(q_2\sin q_1\cosh q_2-q_1\cos q_1\sinh q_2\right)+\\&+\beta_0\beta_1\left[2q_1q_2\left(1-\cos q_1\cosh q_2\right)+\left(q_2^2-q_1^2\right)\sin q_1\sinh q_2\right]=0\end{aligned}\qquad(3.17)$$

In clamped-clamped beams ($\beta_0 = \beta_1 = \pm\infty$), Eqs. (3.17) and (3.16) yield

$$\left(q_1\cos\frac{q_1}{2}\sinh\frac{q_2}{2}-q_2\sin\frac{q_1}{2}\cosh\frac{q_2}{2}\right)\left(q_1\sin\frac{q_1}{2}\cosh\frac{q_2}{2}+q_2\cos\frac{q_1}{2}\sinh\frac{q_2}{2}\right)=0\qquad(3.18)$$

$$\frac{v_1+v_3}{2v_2}=\frac{d}{c}\quad\text{for odd eigenvalue }\lambda\qquad(3.19)$$

For even eigenvalues λ, the constant c given by Eqs. (3.14) is equal to zero.

For simply supported beams, ($\beta_0 = \beta_1 = 0$), the eigenfunctions coincide with the Eulerian critical shapes:

$$v\left(x\right)=C\sin m\pi z,\quad m=1,\ldots,\infty\qquad(3.20)$$

In this case, the first vibration frequency vanishes for $n = -\pi^2$ corresponding to the first Eulerian critical load. In fact the couple [0, √2/2] belongs to the curve for $n = -\pi^2$.

Moreover, for simply supported beam, Eq. (3.17) yields the classical result as follows:

$$\sin q_1=2\cos\frac{q_1}{2}\sin q_1=0\quad\Rightarrow q_1=m\pi,\quad q_2=\frac{\lambda^2}{m\pi}\quad\text{for }m=1,\ldots,\infty\qquad(3.21)$$

Using the first two of Eqs. (3.14) and coefficients q_1, q_2 reported in Eqs. (3.21), Eq. (3.17) can be written in the form

$$\frac{v_1+v_3}{2v_2}=\frac{b}{a}\quad\Rightarrow\frac{v_1+v_3}{2v_2}=\frac{1}{2\cos\left(m\pi/4\right)}\quad\text{for }m\text{ odd}\qquad(3.22)$$

Hence, $(v_1 + v_3)/2v_2 = 1/\sqrt{2}$ for m = 1,7, 9, 15, 17, etc. and $(v_1 + v_3)/2v_2 = - 1/\sqrt{2}$ for m = 3, 5, 11, 13, etc.

However, simply supported beam can not define a limit situation because condensation parameter may be less than zero, as shown in the examples of previous sections.

Figure 3.3 magnifies the area of Figure 3.2 in a zone related to the first frequency, reproducing Eq. (3.12) for some particular values of the nondimensional axial force *n*, Eq. (3.19) corresponding to the clamped-clamped limit situation, and Eq. (3.22) for the particular case of simply supported beam (dashed line). Therefore, Figure 3.4 represents a plot where the point of experimental coordinates [λ, $(\nu_1 + \nu_3)/2\nu_2$] can be located; hence the curve NL^2/EJ containing the experimental point yields the unknown value of the axial force *N*.

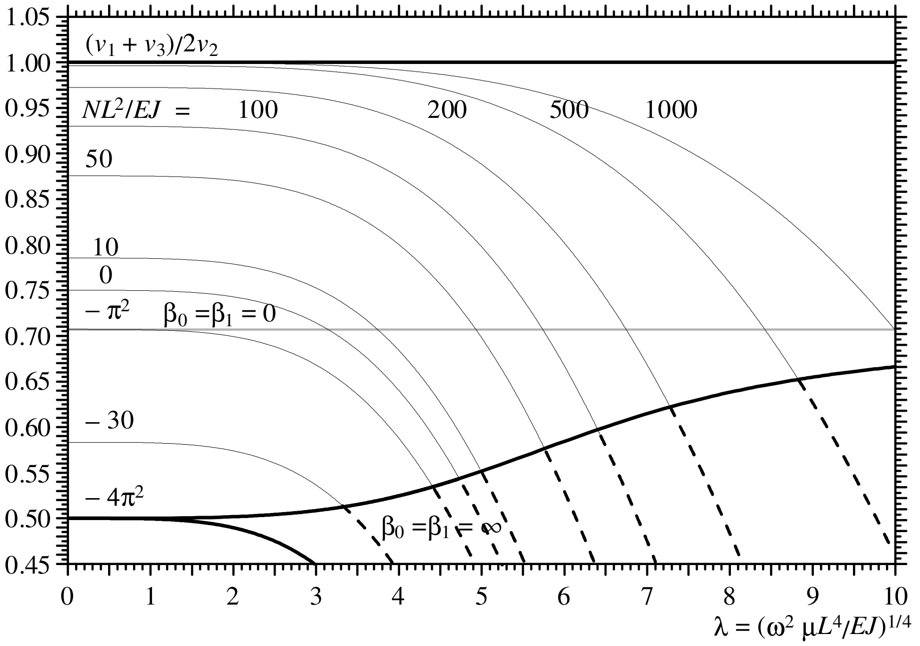

Figure 3.3 – f Ratio $(\nu_1 + \nu_3)/2\nu_2$ versus λ for the first vibration frequency, for some given values of *n*

3.2.4 Laboratory tests

In civil or mechanical engineering, when a single span of a continuous beam is to be analyzed, the adjacent beams behave as elastic constrains with respect to the beam under investigation. Therefore, it is usual to idealize the adjacent beams as rotational springs and the beam under investigation as if it were constrained by elastic rotational springs at one or both ends. This is the reason why a reference model of a beam resting on rigid supports and constrained by two end rotational springs is commonly adopted. In the laboratory tests reported in the following, the end rotational springs were brought back to adjacent spans of a continuous beam and the stiffness values of rotational springs were assumed to coincide with the flexural stiffness of the adjacent beam. In the case of vault tie-rod restrained by lateral masonry walls, the masonry behaviour at the rod ends is modelled again with elastic rotational springs which reproduce the restraining effect of the masonry wall. In fact, as far as vibrations imply very small deflections, a purely elastic model can be acceptable.

In order to apply the analytical procedure derived in the previous section, a set of experimental tests have been organized, Figure (3.4-3.8).

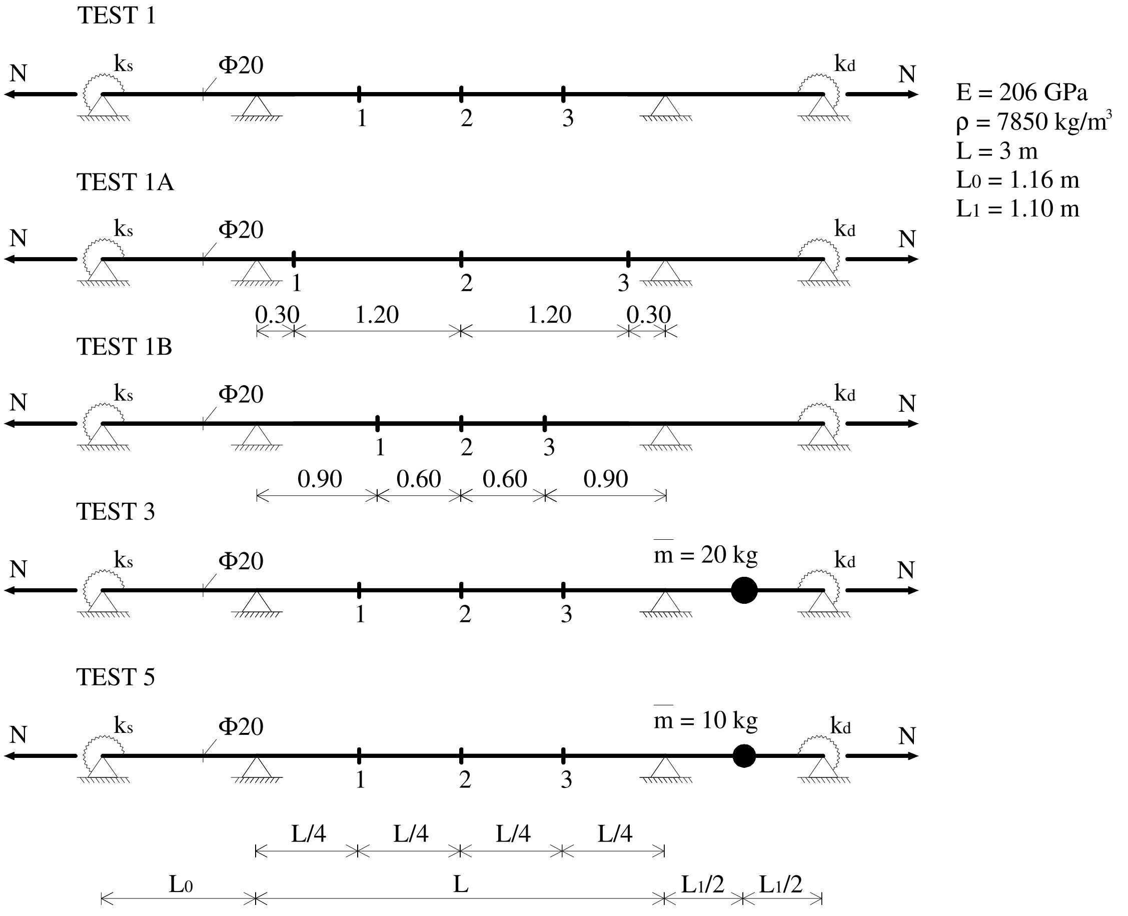

Figure 3.4 – Experimental frames configuration (units in m)

A steel rod with 20 mm diameter was adopted and Young’s modulus E = 206 GPa and density ρ = 7850 kg/m^3 were experimentally evaluated. In order to create outer spans simulating end constraints of variable stiffness, two additional supports were introduced at intermediate section (Figure 3.6a). With the aim of observing the variation of the dynamic stiffness of the right span, additional masses were fixed at its middle span, having $\overline{m}$ = 10 kg for test 3 and $\overline{m}$ = 20 kg for test 5, Figure 3.6b. The configurations of test 1A and 1B are the same of test 1, except for the location of the instrumented sections. As it will be presented in Section 3.2.5.1, in order to evaluate a variation in the identification accuracy, spacing of 1.20 m for test 1A and 0.60 m for test 1B are adopted instead of 0.75 m as for the other tests.

At one end, an hydraulic jack was adopted to assign the axial force and, at the other end, two 100 kN load cells were placed, with accuracy of 2 mV/V (Figure 3.8). Steps load of about 5 kN for each configuration were assigned to the rod, up to a maximum value of 51.13 kN for test 1, 40.81 kN for test 2 and 40.64 kN for test 3.

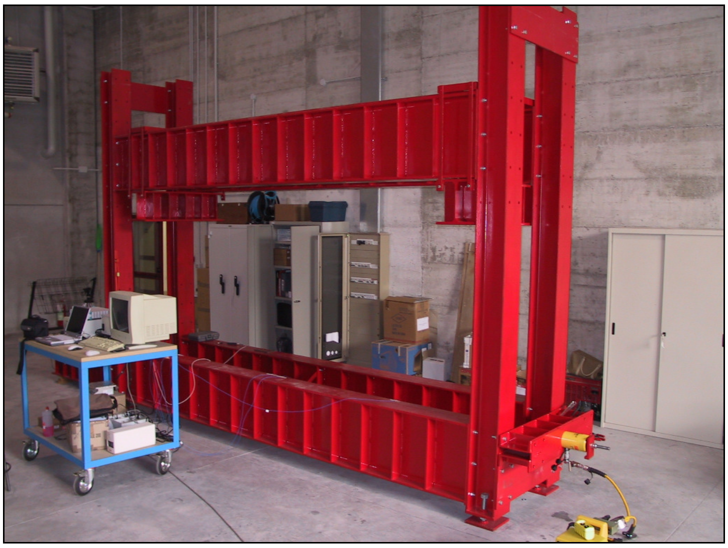

Figures 3.5 – Frame for experimental tests

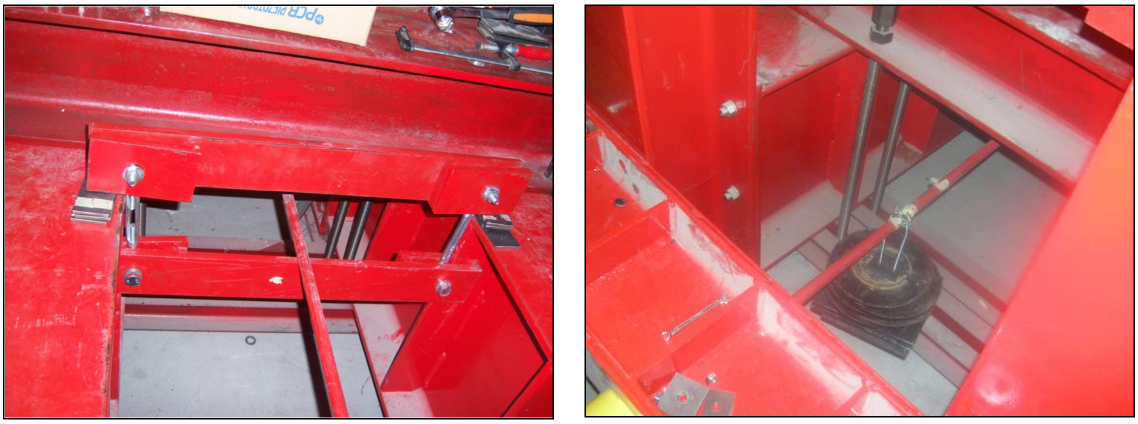

Figures 3.6 – Internal support of the rod and cast iron discs lumped at the middle of right span

Figure 3.7 – Accelerometers arrangement and fixing system adopted by metallic wrappers

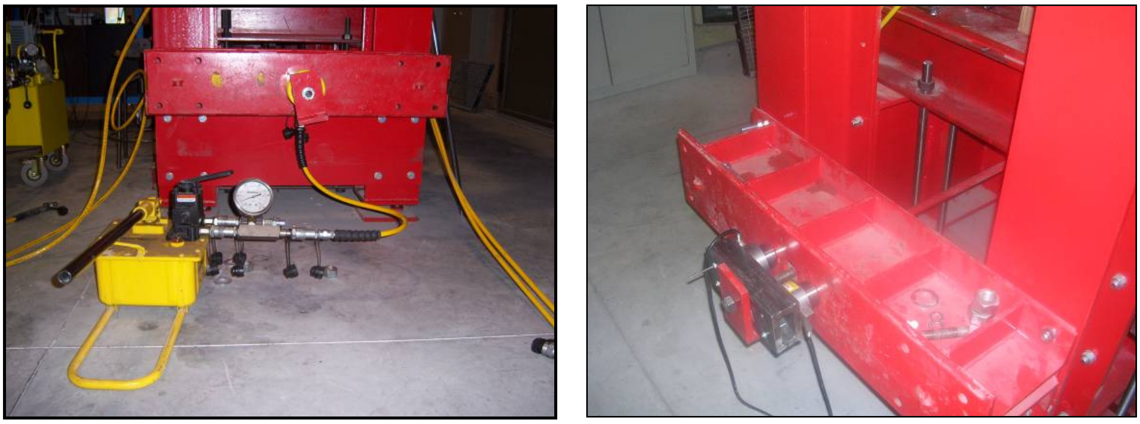

Figures 3.8 – The rod is pulled by the hydraulic jack and the stress and 2 load cells measure the load assigned

Three piezoelectric accelerometers PCB/353B18, having sensitivity of 10 mV/g and weight of 1.8 g, were fastened in the central span, at equal distances, by means of metallic wrappers (Figure 3.7).

Dynamic tests were performed, hitting the instrumented sections with an impact hammer PCB/086C04, able to measure a pulse up to 4.4 kN with sensitivity of 1.2 mV/N. All the instruments were connected to a signal conditioner and, finally, to a PC data acquisition system set with block size (*BS*) equal to 2^{16} and 5000 Hz as sampling rate (*SR*). For each value of axial load imposed by the actuator, the tests were performed hitting, three times, each of the three instrumented sections of the central span.

Because of the difficulty in evaluating the effective rotational stiffness introduced by the experimental equipment, in Figure 3.4 two springs of unknown stiffness are idealized at the end of the beam (k_s, k_d).

3.2.5 Experimental modal analysis techniques employed

Some fundamental topics of signal analysis theory, required for the definition of the frequency response function (FRF), are summarized following Bendat and Piersol (1993), Piersol and Paez (2009). In fact, many of the methods operating in frequency domain make use of FRF to obtain the dynamic characteristics of structures.

3.2.5.1 Fourier Transform

A periodic signal, i.e. $x(t) = x(t + T_0)$ for all t, where T_0 is the period, can be written as sum, generally finite, of harmonic functions by mean of Fourier's series:

$$x(t) = \sum_{k=-\infty}^{+\infty} X_k(\omega) e^{\mathrm{i}k\omega t} \tag{3.23}$$

where the coefficients X_k are given by

$$X_k(\omega) = \frac{1}{T_0} \int_{-\frac{T_0}{2}}^{\frac{T_0}{2}} x(t) e^{-\mathrm{i}k\frac{2\pi}{T_0}t} \, \mathrm{d}t \tag{3.24}$$

The Fourier transform is the generalization of the Fourier series for non periodic function, i.e. $T_0 = \infty$. The Fourier transform of a function $x(t)$ is given by

$$X_k(\omega) = \int_{-\infty}^{+\infty} x(t) e^{-\mathrm{i}\omega t} \mathrm{d}t \tag{3.25}$$

In order to calculate the corresponding Fourier coefficient to k-th harmonic through discrete steps Δt, an approximation of Eq. (3.24) is required:

$$X_k = \frac{1}{N\Delta t} \sum_{n=0}^{N-1} x(n\Delta t) e^{-\mathrm{i}k\frac{2\pi}{N\Delta t}n\Delta t} = \frac{1}{N} C_k \tag{3.26}$$

where $N\Delta t$ is the sampling time, $(BS\text{-}1)/SR$, and C_k

$$C_k = \sum_{n=0}^{N-1} x(n\Delta t) \tag{3.27}$$

is the fast Fourier transform (FFT) or discrete transform (DFT). Note that the FFT defines *N* discrete frequency values for *N* discrete time values with an inherent frequency resolution of

$$\Delta\omega = \frac{1}{N\Delta t} \tag{3.28}$$

As it is known, the Nyquist frequency occurs at $m = N/2$, hence only the first ($N/2 - 1$) frequency components represent unique values; the last ($N/2 - 1$) frequency component constitute the redundant values representing the negative frequency components in Eq. (3.25).

3.2.5.2 The frequency response function

The definition of the frequency response function (FRF) is of particular importance for the identification techniques in the frequency domain.

The general mathematical representation of a single degree of freedom (sdof) system is expressed by

$$m\ddot{x}(t) + c\dot{x}(t) + kx(t) = f(t) \tag{3.29}$$

where m is the mass constant, c the damping constant and k the stiffness constant. An equivalent equation of motion is determined for the Fourier transform or frequency domain (ω). This representation has the advantage of converting a differential equation to an algebraic equation. This is accomplished by taking the Fourier transform of Eq. (3.29). Thus, Fourier transform solution of Eq. (3.29) becomes:

$$X(\omega) = \alpha(\omega) F(\omega) \tag{3.30}$$

where

$$\alpha(\omega) = \frac{1}{-m\omega^2 + \mathrm{i}c\omega + k} \tag{3.31}$$

Equation (3.30) states that the system response $X(\omega)$ is directly related to the system forcing function $F(\omega)$ through the quantity α (ω). If the system forcing function $F(\omega)$ and its response $X(\omega)$ are known, $\alpha(\omega)$ can be calculated. That is:

$$\alpha(\omega)=\frac{X(\omega)}{F(\omega)} \tag{3.32}$$

The quantity $\alpha(\omega)$ is known as the *frequency response function* of the system. The FRF relates the Fourier transform of the system input to the Fourier transform of the system response.

The denominator of the FRF in Eq. (3.31) contains the characteristic equation of the system. Note that the characteristic values of this complex equation are in general complex even though the equation is a function of real-valued independent variable (ω). The characteristic values of this equation are known as the complex roots of the characteristic equation or the complex poles of the system. In term of modal parameters, these characteristic values are also called the modal frequencies. This means that the two roots of the characteristic equation of a single dof system are complex conjugates. For most real structure the damping ratio is rarely higher than 10 percent.

More precisely, the FRFs are defined as the ratio between the Fourier transform of the generic system response (displacement, acceleration …) and the Fourier transform of the modulus of the applied force. The ratio between the Fourier transform of the displacement of a point's system $y(t)$ and the Fourier transform of the applied force is called *receptance*:

$$\alpha(\omega)=\frac{Y(\omega)}{F(\omega)} \tag{3.33}$$

Similarly, *mobility* is the ratio between the Fourier transform of the velocity of a point's system $\dot{y}(t)$ and the Fourier transform of the applied force f. Finally the ratio between the Fourier transform of the acceleration of a point's system $\ddot{y}(t)$ and the Fourier transform of the applied force f is known as *inertance*:

$$H(\omega)=\frac{\ddot{Y}(\omega)}{F(\omega)}=\frac{A(\omega)}{F(\omega)}=-\omega^2\alpha(\omega) \tag{3.34}$$

where $A(\omega)$ stands for the Fourier transform of the acceleration. The development of the FRF solution for the multi degrees of freedom (mdof) case parallels the sdof case. This development relates, mass, damping and stiffness matrices to a matrix frequency response function model, involving mdof:

$$\boldsymbol{\alpha}(\omega) = \frac{1}{-\omega^2\mathbf{M} + \mathrm{i}\omega\mathbf{C} + \mathbf{K}} \tag{3.35}$$

Making use of the well known modal matrix **Φ**, whose column are the eigenvectors, and the expressions derived from the orthogonal modes of vibration

$$\begin{aligned} \boldsymbol{\Phi}^T\mathbf{K}\boldsymbol{\Phi} &= \mathrm{diag}\left\{\omega_r^2\right\} \\ \boldsymbol{\Phi}^T\mathbf{M}\boldsymbol{\Phi} &= \mathbf{I} \\ \boldsymbol{\Phi}^T\mathbf{C}\boldsymbol{\Phi} &= \mathrm{diag}\left\{2\zeta_r\omega_r\right\} \end{aligned} \tag{3.36}$$

the following relation is obtained

$$\boldsymbol{\Phi}^T\boldsymbol{\alpha}(\omega)^{-1}\,\boldsymbol{\Phi} = \boldsymbol{\Phi}^T\left(-\omega^2\mathbf{M} + i\omega\mathbf{C} + \mathbf{K}\right)\boldsymbol{\Phi} = \mathrm{diag}\left\{\omega_r^2 - \omega^2 + 2\mathrm{i}\zeta_r\omega_r\omega\right\} \tag{3.37}$$

Hence, the frequency response function can be written as

$$\boldsymbol{\alpha}(\omega) = \frac{\boldsymbol{\Phi}^T\boldsymbol{\Phi}}{\mathrm{diag}\left\{\omega_r^2 - \omega^2 + 2\mathrm{i}\zeta_r\omega_r\omega\right\}} \tag{3.38}$$

or showing the components

$$\alpha_{hk}(\omega) = \sum_{r=1}^{\mathrm{N}} \frac{\Phi_{rh}\Phi_{rk}}{\omega_r^2 - \omega^2 + 2\mathrm{i}\zeta_r\omega_r\omega} \tag{3.39}$$

Makin use of Eq. (3.34), the inertance function can be written as

$$H_{hk}(\omega) = -\sum_{r=1}^{\mathrm{N}} \frac{\omega^2\left(R_{hk}\right)_r}{\omega_r^2 - \omega^2 + 2\mathrm{i}\zeta_r\omega_r\omega} \tag{3.40}$$

where the residue $(R_{hk})_r$ is the product of the eigenvectors. Just as in the analytical case where the ultimate solution can be described in terms of sdof systems, the FRFs between any input and response dof can be represented as a linear superposition of the sdof models derived previously.

3.2.5.3 Stationary random vibrations

A random vibration is one whose value at any time can not be predicted from its value at any other time. It can be thought of as a single physical realization, $x(t)$, of a random process, which theoretically is described by an ensemble of all possible physical realizations denoted by $\{x(t)\}$. Virtually all stationary random vibrations can be represented by an ergodic random process, meaning the properties of the random process $\{\mathrm{x}(t)\}$ can be described by time averages over a signal sample record $x(t)$. It follows that the sample records of a stationary random vibration collected repeatedly under similar conditions will have time histories that differ in detail but have the same average properties. When one or more of the average parameters of interest remain constant overt time, the phenomenon is called stationary.

By definition, random vibrations cannot be described by an explicit mathematical functions and, hence, must be described in statistical terms. This can be done in the amplitude domain by probability functions, in the time domain by correlation functions, and, as presented in the follow, in the frequency domain by spectral density functions.

Given a stationary random vibration $x(t)$, the *autocorrelation function* $R_{xx}(\tau)$ of $x(t)$ is given by

$$R_{xx}(\tau) = \lim_{T\to\infty} \frac{1}{T} \int_0^T x(t)\, x(t+\tau)\, \mathrm{d}\tau \tag{3.41}$$

where τ is a time delay. The autocorrelation function is essentially a measure of the linear relationship between the values of the random vibration at any two instances t and $t + \tau$. The Fourier transform of the autocorrelation function yields the *power spectral density function* (also called the *autospectral density function*, or more simply the *power spectrum* or *autospectrum*:

$$W_{xx}(\omega) = \int_{-\infty}^{+\infty} R_{xx}(\tau) e^{-\mathrm{i}2\pi\omega\tau} \mathrm{d}\tau \tag{3.42}$$

It my be defined in a manner more relevant to data analysis algorithms by

$$\begin{aligned} W_{xx}(\omega) &= \lim_{T\to\infty} \frac{2}{T} E\left[\left|X(\omega,T)\right|^2\right] \quad \omega > 0 \\ \hat{W}_{xx}(\omega) &= \frac{2}{n_d T} \sum_{k=1}^{n_d} \left|X(\omega,T)\right|^2 \qquad \omega > 0 \end{aligned} \tag{3.43}$$

where $E[]$ is the expected value of [], which implies an ensemble average, the hat (^) denotes an estimate as opposed to an exact value and n_d stands for the number of tests. The power spectral density function describes the frequency content of the vibration and, hence, is generally the most important and widely used function for engineering applications, which are facilitated by three important properties of power spectra, as follows:

i) Given two or more statistically independent vibrations, the power spectrum for the sum of the vibration is equal to the sum of the power spectra for the individual vibrations, that is,

$$W_{xx}(\omega) = \sum_k W_{kk}(\omega) \qquad k = 1, 2, 3, \ldots \tag{3.44}$$

ii) The area under the power spectrum between any two frequencies, ω_a and ω_b equals the mean square value of the vibration in the frequency range form ω_a to ω_b that is

$$\psi_x^2(\omega_a, \omega_b) = \int_{\omega_a}^{\omega_b} W_{xx}(\omega)\, \mathrm{d}\omega \tag{3.45}$$

iii) Given an excitation $x(t)$ to a structural system with a frequency response function $H(\omega)$, the power spectrum of the response $y(t)$ is given by the product of the power spectrum of the excitation and the squared magnitude of the response function, that is,

$$W_{yy}(\omega) = \left|H(\omega)\right|^2 W_{xx}(\omega) \tag{3.46}$$

The digital algorithm to implement the autospectrum can be written as

$$\hat{W}_{xx}(m\Delta\omega) = \frac{2SR}{n_d BS} \sum_{k=1}^{n_d} \left|X_k(m\Delta\omega)\right|^2 \qquad m = 1, 2, \ldots, \frac{N}{2} - 1 \tag{3.47}$$

Given two stationary random vibrations, $x(t)$ and $y(t)$, the *cross correlation function* $R_{xy}(\tau)$ between $x(t)$ and $y(t)$ is given by

$$R_{xy}(\tau) = \lim_{T\to\infty}\frac{1}{T}\int_0^T x(t)\,y(t+\tau)\,\mathrm{d}\tau \tag{3.48}$$

The cross correlation function is a measure of the relationship between two random vibrations at any instance t with a time delay τ between two random vibration time histories. The Fourier transform of the cross correlation function yields what is generally a more important descriptive property of two stationary random vibrations, namely, the *cross spectral density function* (also called the *cross spectrum*):

$$W_{xy}(\omega) = \int_{-\infty}^{+\infty} R_{xy}(\tau)e^{-\mathrm{i}2\pi\omega\tau}\mathrm{d}\tau \tag{3.49}$$

It is defined by

$$\begin{aligned} W_{xy}(\omega) &= \lim_{T\to\infty}\frac{2}{T}E\left[X^*(\omega,T)Y(\omega,T)\right] \quad \omega > 0 \\ \hat{W}_{xy}(\omega) &= \frac{2}{n_d T}\sum_{k=1}^{n_d} X^*(\omega,T)Y(\omega,T) \qquad \omega > 0 \end{aligned} \tag{3.50}$$

where $X^*(\omega,T)$ is the complex conjugate of the Fourier transform of $y(t)$. The cross spectrum is generally a complex number that measures the linear relationship between two random vibration as a function of frequency with a possible phase shift between the vibration. Specifically, the cross spectrum can be written as

$$W_{xy}(\omega) = \left|W_{xy}(\omega)\right|e^{-\mathrm{i}\theta_{xy}(\omega)} \qquad \theta_{xy}(\omega) = 2\pi\omega\tau(\omega) \tag{3.51}$$

where $\tau(\omega)$ is the time delay between $x(t)$ and $y(t)$ a the frequency ω. An important application of the cross spectrum is as follows. Given a random excitation $x(t)$ to a structure with a frequency response function $H(\omega)$, the cross spectrum between the excitation $x(t)$ and the response $y(t)$ is given by the product of the power spectrum of the excitation and the frequency response function, $H(\omega)$, that is,

$$W_{xy}(\omega) = H(\omega)W_{xx}(\omega) \quad \Rightarrow \quad H(\omega) = \frac{W_{xy}(\omega)}{W_{xx}(\omega)} \tag{3.52}$$

where W_{xx} stands for the autospectrum of the exciting force due to the hammer and W_{xy} the cross spectrum of the instrumented section.

The digital algorithm to implement the cross spectrum can be written as

$$\hat{W}_{xy}\left(m\Delta\omega\right)=\frac{2SR}{n_d BS}\sum_{k=1}^{n_d}X_k^*\left(m\Delta\omega\right)Y_k\left(m\Delta\omega\right) \qquad m=1,2,\dots,\frac{N}{2}-1 \tag{3.53}$$

Even though the correct evaluation of the frequency response function for each instrumented section is through Eq. (3.52), it was seen that each hammer hit can be considered as an independent phenomenon and the FRF of the generic instrumented section can be evaluated, without leakage of information, considering its mean value for the set of three hammer hits making use of Eq. (3.34), rewritten here:

$$\overline{H}_{ij}\left(\omega\right)=\frac{1}{3}\sum_{k=1}^{3}H_{ij,k}\left(\omega\right)=\frac{1}{3}\sum_{k=1}^{3}\frac{A_{i,k}\left(\omega\right)}{F_{j,k}\left(\omega\right)} \tag{3.54}$$

where i represents the section instrumented position and j the position of the hammer hit.

The following graph shows the comparison between two FRF recorded during the experimental tests. The first, in blue line, is evaluated by means of Eq. (3.52), whilst the second one, in green line, derives from Eq. (3.54). Obviously, W_{xy} and W_{xx} are evaluated making use of Eq. (3.53) and (3.47), respectively, in which n_d = 3. The two experimental functions are strictly close over the whole range of frequency considered. Therefore, in the data analysis, the experimental FRFs has been singly evaluated for each hammer impact and Eq. (3.54) has been employed.

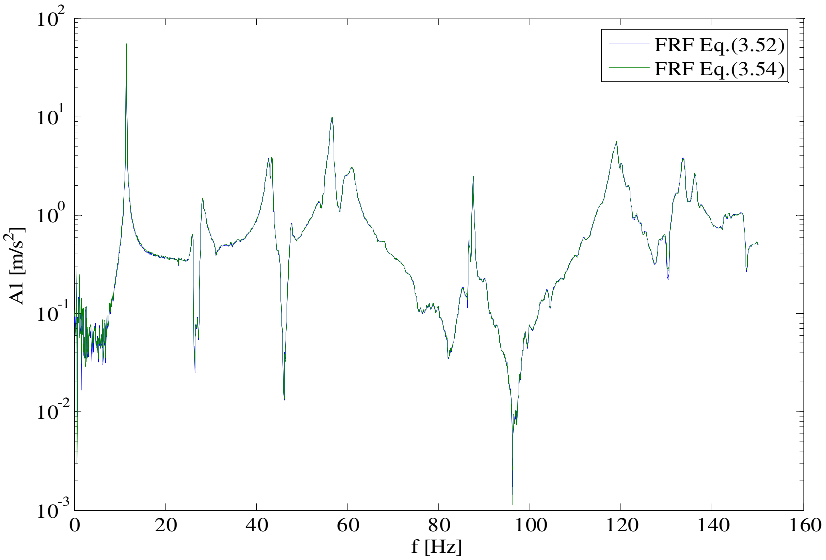

Figure 3.9 – Comparison between Eq. (3.52) and Eq. (3.54) for the evaluation of the experimental FRFs

3.2.5.4 Dynamic identification in the frequency domain

Algorithms in the frequency domain require the acquisition of the accelerations from the experimental tests and allow to get information on the dynamic behaviour of a structure in terms of natural frequencies, modal damping and mode shapes using the features of frequency response.

The are many methods to identify the modal parameter of a system from FRF, but many are based on the same assumptions: in the proximity of the natural frequencies of the system, the contribution of the mode that causes the resonance is predominant over the others, which are thus negligible. With this assumption, a system with *N* degrees of freedom can be transformed into *N* sdof systems and thus it's possible to operate on a limited range of frequencies around the *r*-th natural frequency.

This section describes the fitting techniques, employed in this work, to extract from FRFs the modal characteristics of the structures

Peak picking method (PPM).

This method can be successfully applied for systems with low damping ratio and when the vibration frequencies are not very close to each other (Ewins, 1984).

Figure 3.10 shows an example of the times histories and the frequency spectra of the impact hammer and of three accelerometers for a given pulse. This kind of graphs are typical for test 1, where no masses have been fastened to the structure. It can be noted that the natural frequencies of the system correspond to the peaks of the inertance functions, which are also well spaced.

In the neighbourhood of a given natural frequency ω_r, Eq. (3.40) admits the following approximation

$$H_{hk}(\omega) \cong -\frac{\omega^2}{mL}\frac{v_h^{(r)}v_k^{(r)} \Big/ \left\| v^{(r)} \right\|^2}{\omega_r^2 - \omega^2 + 2i\zeta_r\omega_r\omega} \tag{3.55}$$

Then, the contributions of modes with different circular frequencies can be neglected, and the frequency domain analysis of the vibration beam reduces to that of an independent sdof. Consequently, the peak-picking method can usefully be adopted. In other words, natural frequencies are located at each peak of inertance moduli (Figure 3.10) and the damping value can be estimated with the half-power method. As matter of fact, for the first three frequencies of the beam under investigation, damping ratios turned out to be less than 5% so as to justify the use of Eq. (3.55). Finally, Eq. (3.55) shows that the *r*-th eigenvalue components are proportional to the inertance modulus peaks. Then, hitting the *j*-th instrumental section, the following ratios are obtained (Tullini and Laudiero, 2008):

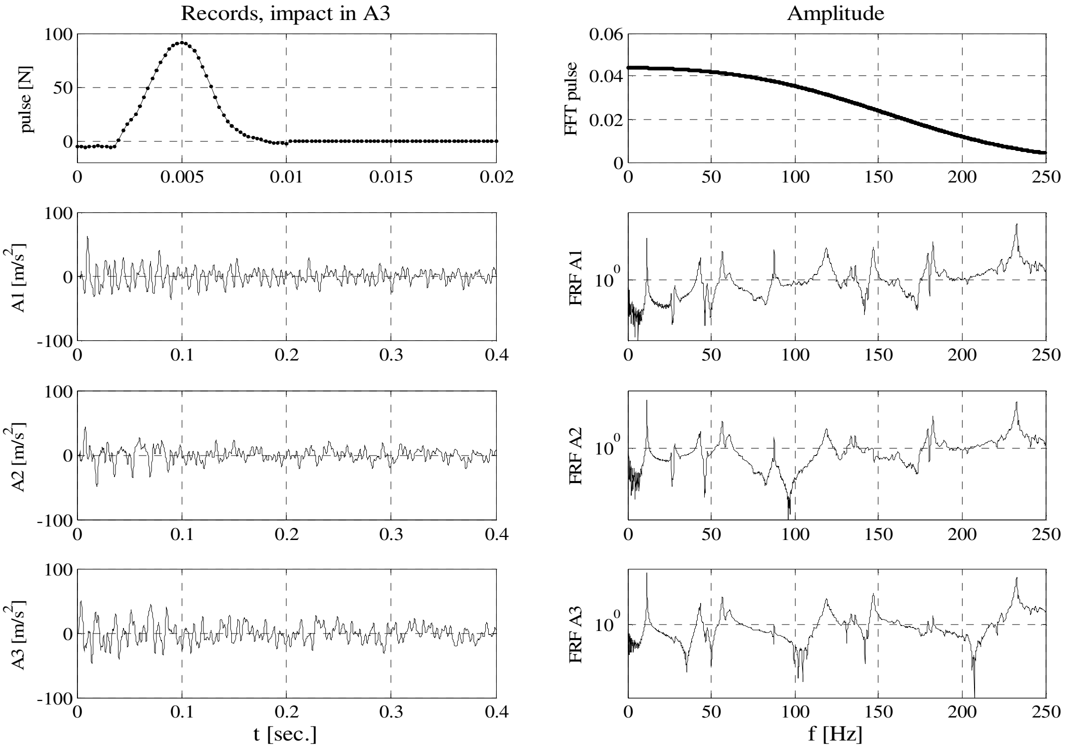

Figure 3.10 – Time history and frequency spectrum for the impact hammer and three instrumented sections (from test 1)

$$\frac{v_1^{(r)}}{v_2^{(r)}} = \frac{\left|H_{1,j}\left(\omega_r\right)\right|}{H_{2,j}\left(\omega_r\right)}, \qquad \frac{v_3^{(r)}}{v_2^{(r)}} = \frac{\left|H_{3,j}\left(\omega_r\right)\right|}{H_{2,j}\left(\omega_r\right)} \tag{3.56}$$

Pole/Residue Model Identification (PRMI).

It is known that the response of a linear system with N degrees of freedom can be represented by the sum of the responses of individual modes of vibration. In the frequency domain expression of receptance, i.e. the ratio of Fourier transform and the displacement of the driving force Eq. (3.39), can be written as (Ewins, 1984)

$$\boldsymbol{\alpha}\left(\omega,\mathbf{p}\right) = \sum_{r=1}^{N} \frac{\mathbf{R}\left(\omega_j\right)}{\omega_r^2 - \omega^2 + 2i\xi_r\omega_r\omega} \tag{3.57}$$

where $\mathbf{R}$ is the matrix of the residue, i.e. the product of the eigenvectors $\boldsymbol{\Phi}(\omega_r)\ \boldsymbol{\Phi}(\omega_r)^{\mathrm{T}}$, normalized respect to the mass matrix. The linear system is completely identified if the modal parameters $\mathbf{p} = \{\ \omega_r,\ \xi_r,\ \boldsymbol{\Phi}(\omega_r)\}_{r\ =\ 1,\ldots N}$ are known. If only M parameters are known, Eq. (3.57) can be approximated by

$$\boldsymbol{\alpha}\left(\omega,\mathbf{p}\right)=\sum_{r=1}^{M}\frac{\mathbf{R}\left(\omega_{j}\right)}{\omega_{r}^{2}-\omega^{2}+2i\xi_{r}\omega_{r}\omega}+\mathbf{E} \tag{3.58}$$

where **E** is a constant matrix. The fitting algorithm PRMI (Pole/Residue Model Identification, Balmés, 1997) optimizes the modal parameters minimizing the cost function *J*, for each vibration mode and for each instrumented section:

$$J=\sum_{\substack{i\in\{\text{instrumented section}\}\\ j\in\{\text{actuator position}\}\\ k\in\{\text{frequencies identified}\}}}\left|\alpha_{ij}\left(\omega_{k},\mathbf{p}\right)-\alpha_{ij}^{X}\left(\omega_{k},\mathbf{p}\right)\right|^{2} \tag{3.59}$$

The method is used to evaluate the modal parameters for tests 3 and 5, in which the presence of the lumped mass in the middle of the side beam span produces two frequency peaks too close to use the peak picking method. Figure 3.11 shows a fitting of an experimental FRF of test 3 (blue line) by mean of PRMI (green line), in the amplitude – frequency plane and Bode plot. Figure 3.12 shows the fitting in the Nyquist's plot.

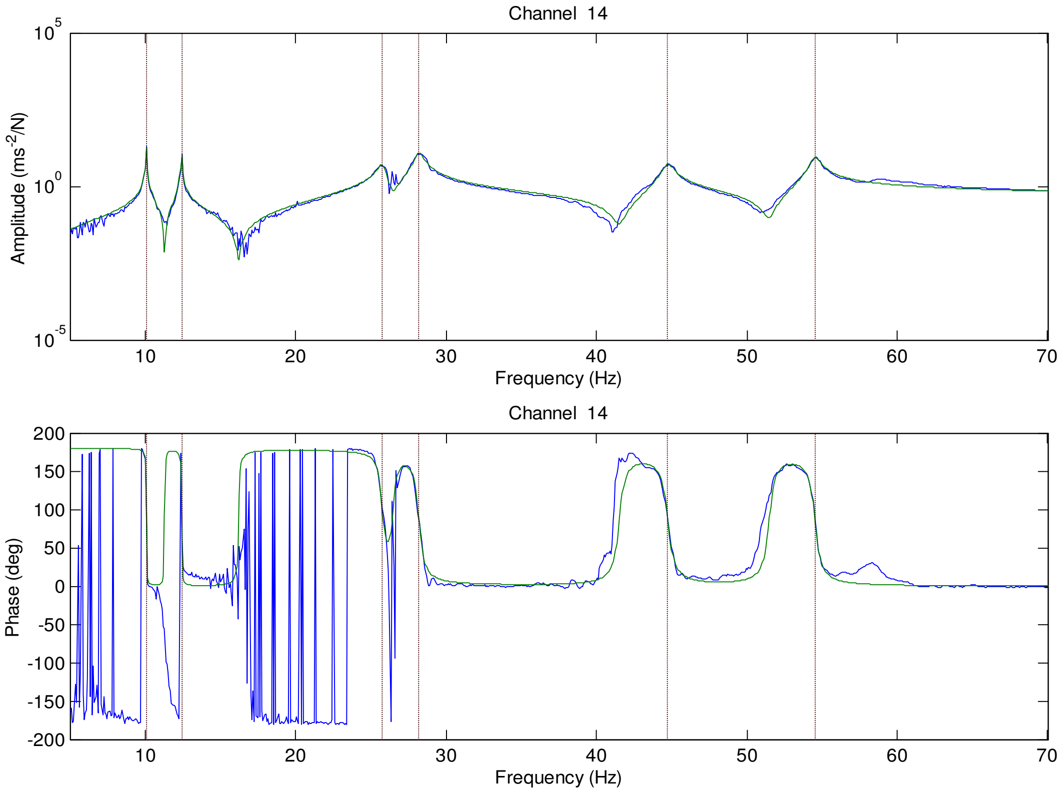

Figure 3.11 – Experimental FRF of a instrumented section and its numerical fitting by means of PRMI. Modulus versus frequency and Bode diagram

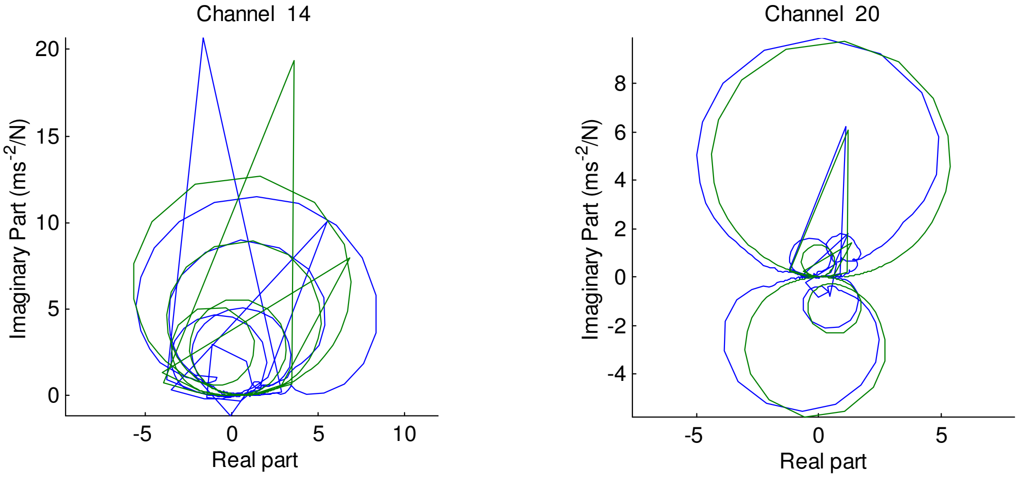

Figure 3.12 – Experimental FRF of two instrumented sections and their numerical fitting by means of PRMI in the Nyquist plane

3.2.6 Results

Making use of the experiment modal analysis introduced in the previous section, average of the experimental and estimated parameters are presented.

3.2.6.1 Experimental data

As described in Section 3.2.5, PPM is applied to test 1 where frequencies are not very close to each other, whereas PRMI is used for test 3 and 5, where lumped mass carried by right span of the frames produces inertance peaks too close to apply PPM. In particular, modal vibration frequencies and amplitudes of the corresponding mode shape at the three instrumented section have been identified for each impact's hammer and for each load step. Since 9 pulses (3 for each instrumented section) have been given for each load step, there are a total of 27 experimental FRFs for each step of axial load. From this data set, only the FRF corresponding to the best measures have been considered, in order not to affect the optimization procedure of the PRMI.

The Tables 3.1 - 3.6 show the average modal parameters for each imposed axial load N_X and for the five configurations tested. On the other hand, the identified couple [λ, $(\nu_1+\nu_3)/2\nu_2$] for test 1, 3 and 5 are plotted in Figure 3.13. For test 1A and 1B, the instrumented section is not at quarters of the beam span, it then has not been located in the plot.

As described in Section 3.2.3, the identified couples [λ, $(\nu_1+\nu_3)/2\nu_2$] lie within the area defined by the limit situation $(\nu_1+\nu_3)/2\nu_2 = 1$ and the curve corresponding to $n = -4\pi^2$, Eulerian critical load for a double clamped beam (dotted lines).

TEST 1

N_a [kN]	f [Hz]	v_1	v_2	v_3	λ	$(v_1+v_3)/2v_2$
5.662	11.520	0.6226	1.0000	0.6477	5.043	0.6352
10.524	13.894	0.6302	1.0000	0.6544	5.538	0.6423
14.978	15.734	0.6399	1.0000	0.6528	5.894	0.6464
20.692	17.785	0.6464	1.0000	0.6572	6.266	0.6518
24.876	19.150	0.6511	1.0000	0.6593	6.502	0.6552
30.712	20.930	0.6546	1.0000	0.6630	6.798	0.6588
35.640	22.295	0.6582	1.0000	0.6659	7.016	0.6621
40.366	23.516	0.6600	1.0000	0.6687	7.205	0.6643
45.577	24.804	0.6613	1.0000	0.6702	7.400	0.6657
50.873	26.084	0.6648	1.0000	0.6722	7.589	0.6685

Table 3.1 – Average of the experimental parameters at the first modal frequency, Test 1

TEST 1A

N_a [kN]	f [Hz]	v_1	v_2	v_3	λ	$(v_1+v_3)/2v_2$
4.502	10.834	0.7371	1.0000	0.7684	3.913	0.7527
10.945	14.049	0.7496	1.0000	0.7730	4.455	0.7613
15.108	15.747	0.7541	1.0000	0.7737	4.717	0.7639
20.077	17.563	0.7576	1.0000	0.7770	4.982	0.7673
24.749	19.109	0.7632	1.0000	0.7790	5.196	0.7711
30.385	20.833	0.7678	1.0000	0.7803	5.426	0.7741
34.871	22.069	0.7693	1.0000	0.7821	5.584	0.7757
40.181	23.453	0.7714	1.0000	0.7840	5.757	0.7777
45.696	24.811	0.7733	1.0000	0.7851	5.921	0.7792
49.771	25.787	0.7758	1.0000	0.7856	6.036	0.7807

Table 3.2 – Average of the experimental parameters at the first modal frequency, Test 1A

TEST 1B

N_a [kN]	f [Hz]	v_1	v_2	v_3	λ	$(v_1+v_3)/2v_2$
4.502	10.834	0.2138	1.0000	0.2268	5.043	0.2203
10.945	14.049	0.2216	1.0000	0.2310	5.538	0.2263
15.108	15.747	0.2220	1.0000	0.2351	5.894	0.2285
20.077	17.563	0.2268	1.0000	0.2384	6.266	0.2326
24.749	19.109	0.2300	1.0000	0.2412	6.502	0.2356
30.385	20.833	0.2348	1.0000	0.2420	6.798	0.2384
34.871	22.069	0.2370	1.0000	0.2446	7.016	0.2408
40.181	23.453	0.2397	1.0000	0.2471	7.205	0.2434
45.696	24.811	0.2425	1.0000	0.2489	7.400	0.2457
49.771	25.787	0.2453	1.0000	0.2493	7.589	0.2473

Table 3.3 – Average of the experimental parameters at the first modal frequency, Test 1B

TEST 3

N_a [kN]	f [Hz]	v_1	v_2	v_3	λ	$(v_1+v_3)/2v_2$
4.476	10.068	0.5765	1.0000	0.7522	4.715	0.6644
11.371	12.289	0.5629	1.0000	0.8444	5.209	0.7036
15.610	13.203	0.5574	1.0000	0.8982	5.399	0.7278
21.049	14.155	0.5507	1.0000	0.9638	5.590	0.7572
26.220	15.253	0.5595	1.0000	0.9661	5.803	0.7628
29.704	15.701	0.4405	0.9459	1.0000	5.888	0.7615
34.645	16.345	0.5402	0.9741	1.0000	6.007	0.7906
41.226	17.156	0.4673	0.9426	1.0000	6.154	0.7780

Table 3.4 – Average of the experimental parameters at the first modal frequency, Test 3

TEST 3 – Second mode shape

N_a [kN]	$f^{(II)}$ [Hz]	$v_1^{(II)}$	$v_2^{(II)}$	$v_3^{(II)}$	$\lambda^{(II)}$	$(v_1^{(II)}+v_3^{(II)})/2v_2^{(II)}$
4.476	12.420	0.6907	1.0000	0.4663	5.236	0.5785
11.371	15.139	0.6671	1.0000	0.5643	5.781	0.6157
15.610	16.561	0.6592	1.0000	0.6009	6.047	0.6300
21.049	18.358	0.6573	1.0000	0.6223	6.366	0.6398
26.220	19.932	0.6599	1.0000	0.6341	6.634	0.6470
29.704	20.966	0.6604	1.0000	0.6399	6.804	0.6501
34.645	22.295	0.6640	1.0000	0.6461	7.016	0.6550
41.226	23.982	0.6658	1.0000	0.6529	7.277	0.6593

Table 3.5 – Average of the experimental parameters at the second modal frequency, Test 3

TEST 5

N_a [kN]	f [Hz]	v_1	v_2	v_3	λ	$(v_1+v_3)/2v_2$
4.427	10.605	0.6049	1.0000	0.6718	4.839	0.6384
10.312	13.459	0.6187	1.0000	0.6836	5.451	0.6511
15.170	15.344	0.6227	1.0000	0.6975	5.820	0.6601
20.162	17.207	0.6313	1.0000	0.6963	6.164	0.6638
25.558	18.814	0.6348	1.0000	0.7083	6.445	0.6716
30.960	20.249	0.6348	1.0000	0.7226	6.686	0.6787
36.735	21.618	0.6340	1.0000	0.7364	6.909	0.6852
41.016	22.551	0.6342	1.0000	0.7483	7.056	0.6913

Table 3.6 – Average of the experimental parameters at the first modal frequency, Test 5

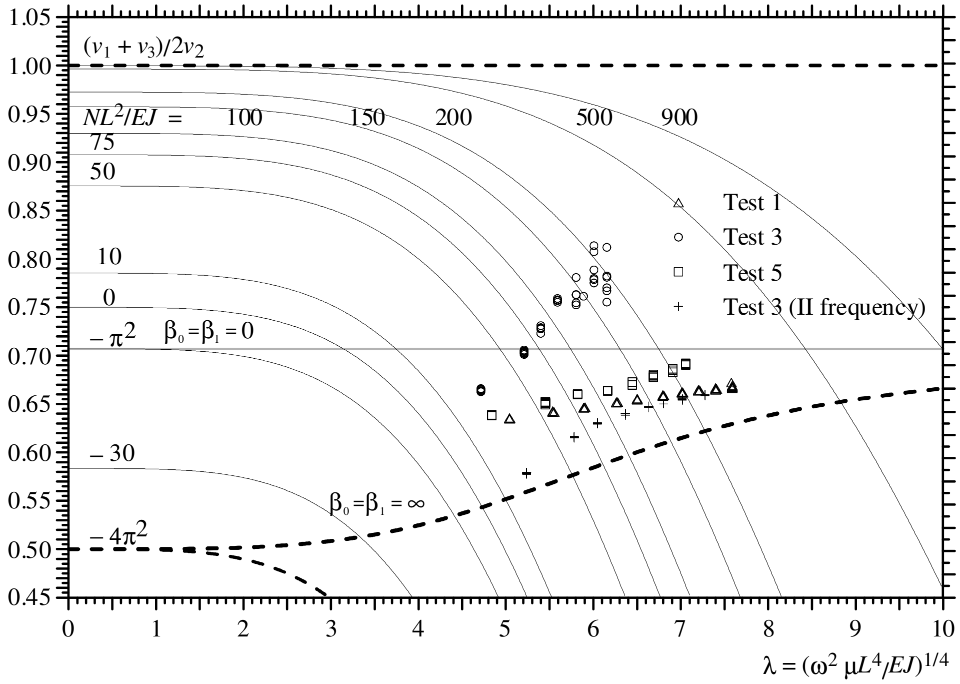

Figure 3.13 – Location of the experimental couples [λ, (v1+v3)/2v2]

The experimental points are very accurate, but for high value of axial load the circles of test 5 are scattered. This is because the mass placed in the middle of the side beam imposes its translational motion to the whole system, so the central beam undergoes its motion (Figure 3.16b). High values of axial load involve an increase in the stiffness of the side beam and the global vibration motion is governed by the translational motion of the lumped mass. Consequently, the amplitudes of the first modal shape become smaller and much more subjected to measurement errors. Moreover, Table 3.4 shows that, for axial load greater than about 26 kN, the highest first modal shape amplitude is recorded at the section v_3 near the right span, instead of section v_2 as in other tests. The scattering observed in Figure 3.13 starts precisely at this value of axial force. Furthermore, as it will be presented in Section 3.2.5.4, the right end stiffness coefficient β_1 takes negative value at the first vibration frequency for high axial load values. Therefore the data points corresponding to the first mode shape are above the line of the simply supported beam case ($\beta_0 = \beta_1 = 0$)

Figures 3.14 and 3.15 show a comparison between two typical FRF of v_1 for test 3 and test 5, respectively. It can be noted from Figure 3.14 that the inertance at the first peak (v_1 in Figure 3.16b), corresponding to the translational vibration motion of the mass (v_1 in Figure 3.16b), is much lower than the second one, which corresponds to the flexural vibration of the central span (v_1 n Figure 3.16a). For lumped mass equal to 10 kg (test 5), the flexural vibration mode of the central span remains the first vibration mode of the frame (Figure 3.16a), so Figure 3.15 shows a well defined peak at the first vibration frequency and measurement errors are smaller.

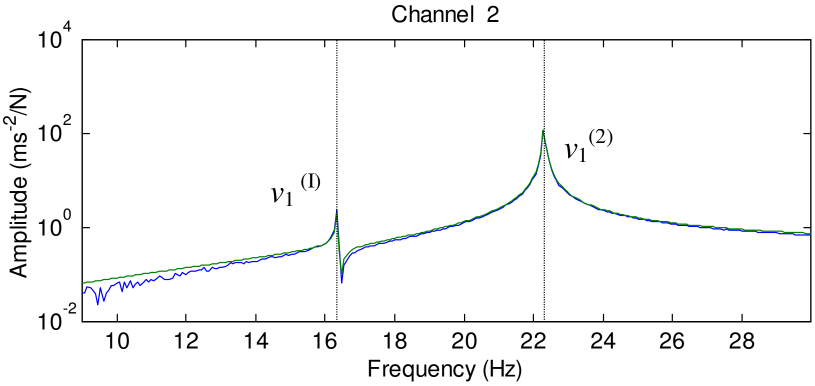

Figure 3.14 – Test 3 (m = 20 kg): experimental FRF for an high value of axial force and its numerical fitting

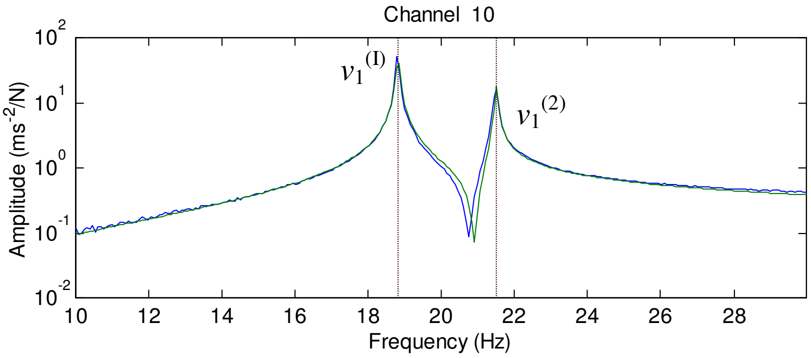

Figure 3.15 – Test 5 (m = 10 kg): typical experimental FRF and its numerical fitting

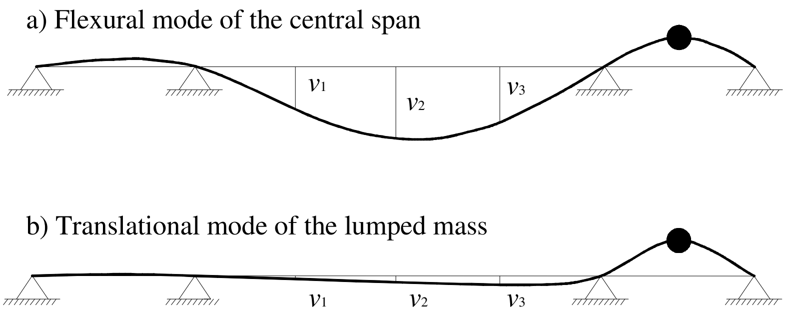

Figure 3.16 – First two mode shapes of the system: a) First mode shape recorded for tests 1 and 5, $\overline{m} = 0, 10\,\text{kg}$ respectively; b) First mode shape recorded for test 3, $\overline{m} = 20\,\text{kg}$ and for high value of N

Therefore, in order to overcome errors in the axial load identification using the first mode shape, the second mode shape has been also identified for test 3. Table 3.5 shows the average modal parameters for each imposed axial load N_X, which are plotted in

Figure 3.13 by cross-symbols. It can be seen that, as expected, the second mode shape corresponds to the flexural vibration of the central span. In fact the modal shape amplitude v_2 recorded in the middle section is the greater for each load step and the experimental points are much closer. Moreover, it should be noted that this data are under the line of the simply supported beam case ($\beta_0 = \beta_1 = 0$).

3.2.6.2 Axial load identification

Estimated axial load N_a may be found by solving Eq. (3.12) for each couple of experimental data [λ, $(v_1+v_3)/2v_2$] of test 1,3,5 and solving numerically Eq. (3.9) for tests 1A and 1B, for which the control points are not located at the quarter of beam span.

Figure 3.17-3.22 compare measured N_X and estimated N_a axial force for each configuration tested. Results for test 3 reported in Figure 3.21 derives from the use of the second flexural mode of the frame.

The graphs show excellent agreement between measured and estimated mean parameters, except for the test 3, where the first mode shape has been used. The scatter of the experimental points for axial load greater than about 26 kN, observed in Figure 3.13, is also evident in the axial load identification at the same load level (Figure 3.20). Nevertheless, using the second mode shape the average percent errors Δ is about 1%.

Finally, from tables beside Figures 3.18-19, it is clear how the percent errors of test 1A with more spaced control point (1.20 m) are much lower than those in test 1B (0.75 m). As expected, for test 1B with less spaced (0.60 m) control points the identification quality gets worse.

N_x [kN]	N_a [kN]	Δ [%]
5.662	5.713	0.90
10.524	10.558	0.32
14.978	14.893	-0.57
20.692	20.497	-0.94
24.876	24.640	-0.95
30.712	30.481	-0.75
35.640	35.427	-0.60
40.366	40.077	-0.72
45.577	45.130	-0.98
50.873	50.693	-0.35

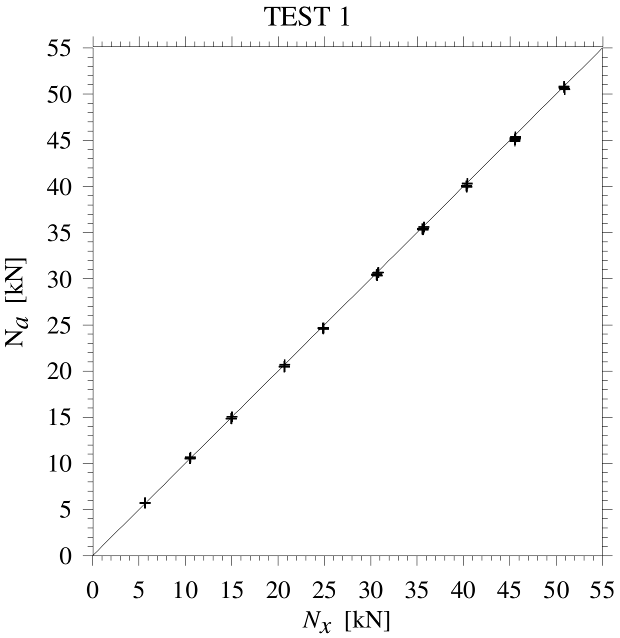

Figure 3.17 – Comparison between measured (N_x) and estimated (N_a) forces, Test 1

N_X [kN]	N_a [kN]	Δ [%]
4.502	4.618	2.44
10.945	11.075	1.19
15.108	15.152	0.24
20.077	20.102	0.15
24.749	24.807	0.24
30.385	30.490	0.35
34.871	34.915	0.13
40.181	40.198	0.04
45.696	45.697	0.00
49.771	49.856	0.17

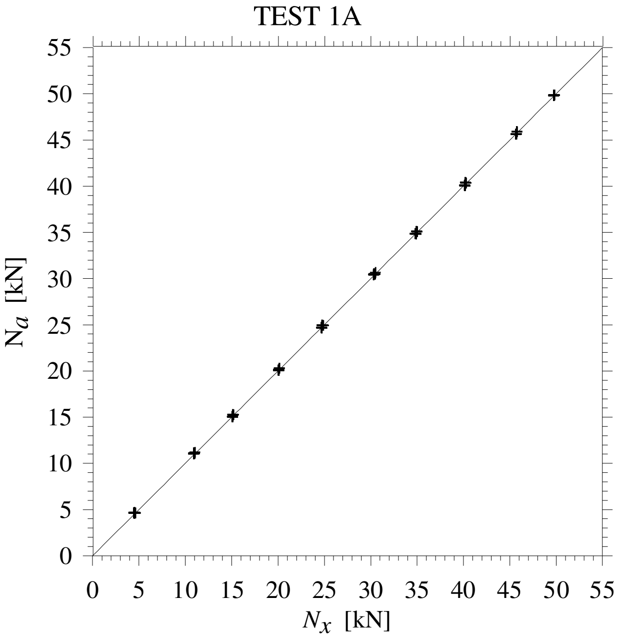

Figure 3.18 – Comparison between measured (N_x) and estimated (N_a) forces, Test 1

N_X [kN]	N_a [kN]	Δ [%]
4.502	4.303	-4.55
10.945	10.698	-2.25
15.108	14.699	-2.77
20.077	19.570	-2.50
24.749	24.222	-2.13
30.385	29.860	-1.73
34.871	34.177	-1.99
40.181	39.381	-1.99
45.696	44.741	-2.09
49.771	48.926	-1.70

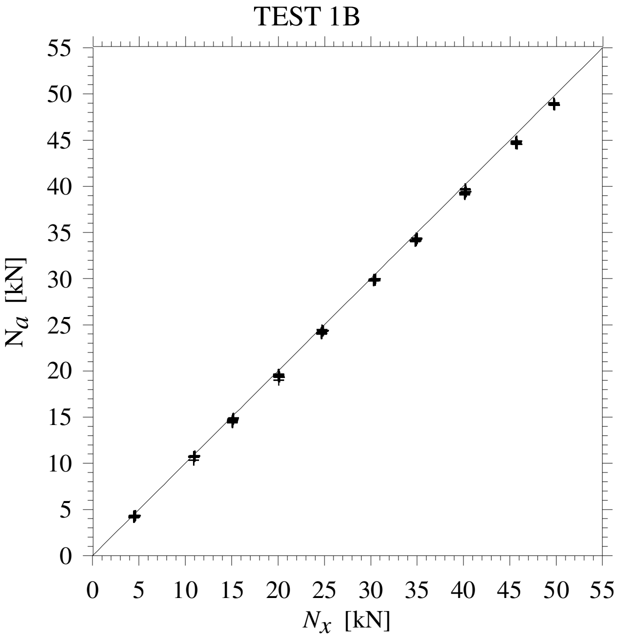

Figure 3.19 – Comparison between measured (N_x) and estimated (N_a) forces, Test 1

N_X [kN]	N_a [kN]	Δ [%]
4.476	4.812	7.51
11.371	11.374	0.02
15.610	15.503	-0.69
21.049	21.211	0.77
26.220	25.430	-3.01
29.704	26.683	-10.17
34.645	34.054	-1.71
41.226	34.970	-15.17

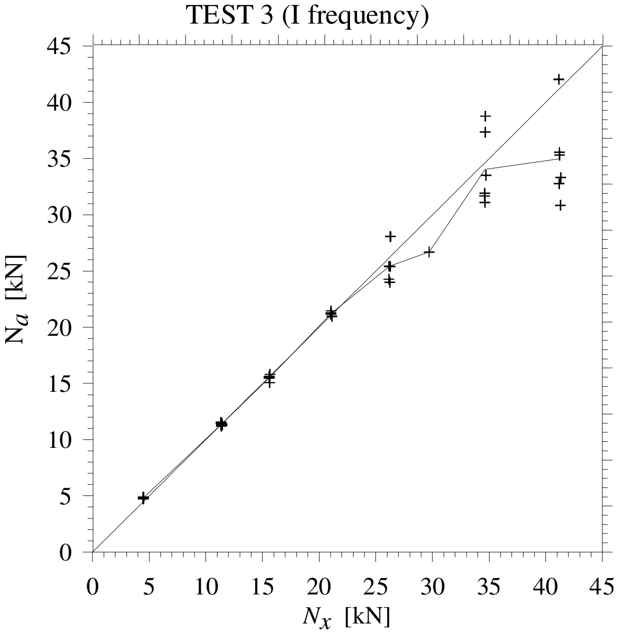

Figure 3.20 – Comparison between measured (N_x) and estimated (N_a) forces, Test 3

N_X [kN]	N_a [kN]	Δ [%]
4.476	4.528	1.17
11.371	11.474	0.90
15.610	15.621	0.07
21.049	20.949	-0.48
26.220	26.084	-0.52
29.704	29.573	-0.44
34.645	34.494	-0.44
41.226	41.031	-0.47

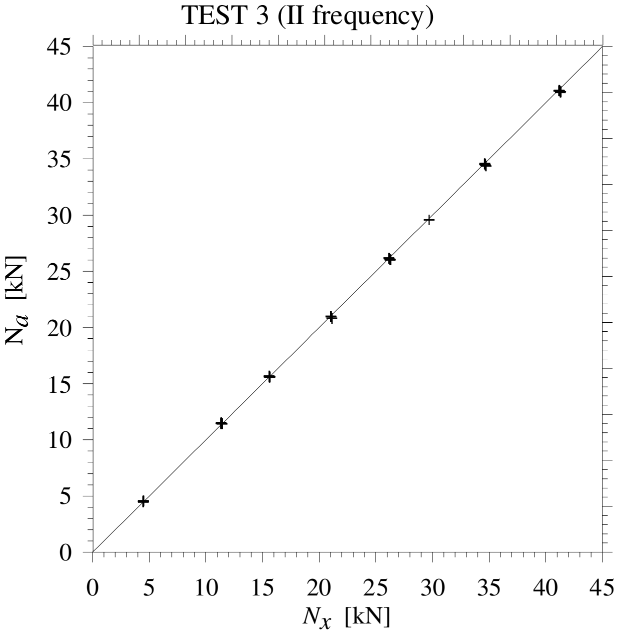

Figure 3.21 – Comparison between measured (N_x) and estimated (N_a) forces using the second mode shape, Test 3

N_x [kN]	N_a [kN]	Δ [%]
4.427	4.380	-1.07
10.312	10.229	-0.80
15.170	15.019	-1.00
20.162	20.045	-0.58
25.558	25.382	-0.69
30.960	30.721	-0.77
36.735	36.307	-1.16
41.016	40.687	-0.80

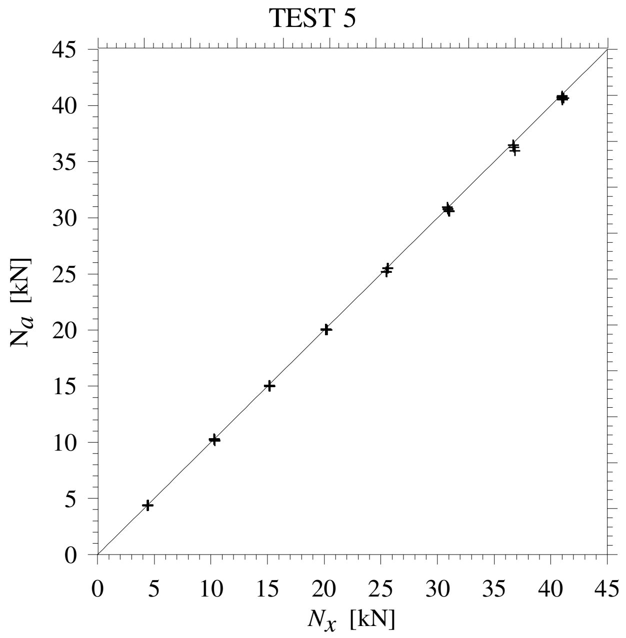

Figure 3.22 – Comparison between measured (N_x) and estimated (N_a) forces, Test 5

3.2.6.3 End stiffness identification

For each couple of experimental data $[\lambda ,(v_{1}+v_{3})/2v_{2}]$ Eq. (3.13) gives estimation of the dynamic condensation parameters β_0 and β_1 for test 1,3 and 5; otherwise for test with control points at generic position, test 1A and 1B, Eqs. (3.10)-(3.11) have been used.

The analytical investigation considered the limit cases $k_s = k_d = 0$ and $k_s = k_d = \infty$ only because of the difficulty of evaluating the rotational stiffness introduced by the experimental equipment. For the limit cases considered, the condensation parameters β_0 and β_1 of the central beam, Figure 3.23, derive form the application of exact dynamic condensation method and takes the expressions obtained in Section 1.5.2 and 1.5.3, see Eq. (3.60), (3.61), (3.62) and (3.63)

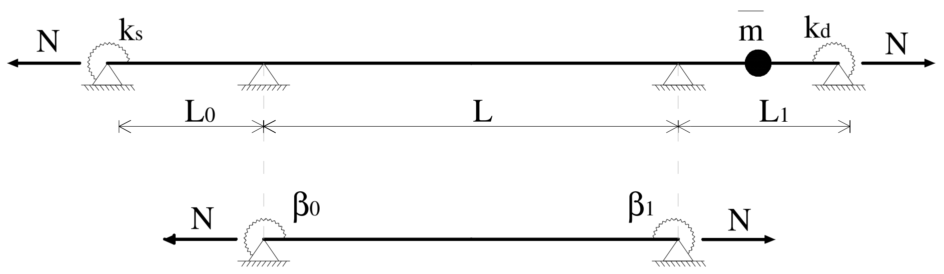

Figure 3.23 – Reference model for the analytical evaluation of the end stiffness coefficients

For supported ends and mass-in-span: $k_{s,d} = 0$ and $\overline{m} > 0$

$$\beta_{0,1}=\frac{L}{L_{0,1}}\frac{\left(2F_2q_1q_2\left(q_1^2+q_2^2\right)+F_2^M\lambda^4\mu\right)^2-\left(F_1^M\lambda^4\mu-2F_1q_1q_2\left(q_1^2+q_2^2\right)^2\right)}{\left(2\chi q_1q_2\left(q_1^2+q_2^2\right)+\chi^M\lambda^4\mu\right)\left(2F_2q_1q_2\left(q_1^2+q_2^2\right)+F_2^M\lambda^4\mu\right)} \tag{3.60}$$

For supported ends and without mass in span: $k_{s,d}=0$ and $\overline{m}=0$

$$\beta_{0,1}=\frac{L}{L_{0,1}}\frac{\left(q_1^2+q_2^2\right)\sin q_1\sinh q_2}{q_2\sin q_1\cosh q_2-q_1\cos q_1\sinh q_2} \tag{3.61}$$

For clamped ends and without mass-in-span: $k_{s,d}=\infty$ and $\overline{m}>0$

$$\beta_{0,1}=\frac{L}{L_{0,1}}\frac{\left(q_1^2+q_2^2\right)\left[2q_1q_2F_2+\mu\lambda^4F_2^M\right]}{2q_1q_2\left(q_1^2+q_2^2\right)\chi+\mu\lambda^4\chi^M} \tag{3.62}$$

For clamped ends and without mass-in-span: $k_{s,d}=\infty$ and $\overline{m}=0$

$$\beta_{0,1}=\frac{L}{L_{0,1}}\frac{\left(q_1^2+q_2^2\right)\left(q_1\cos q_1\sinh q_2-q_2\sin q_1\cosh q_2\right)}{\left(q_1^2-q_2^2\right)\sin q_1\sinh q_2+2q_1q_2\left(\cos q_1\cosh q_2-1\right)} \tag{3.63}$$

It can be noted that Eq. (3.62) has already been analyzed in the Example 2 of Section 2.6.3.2, where its trend versus axial load for the first two modal frequencies has been plotted (Figure 2.15 and 2.16 respectively). Indeed, Example 2 considers the dynamic condensation of a clamped side beam carrying a mass in span in order to evaluate its rotational dynamic stiffness. It corresponds to the analytical evaluation of β_1 in the limit situation $k_d=\infty$ with $\overline{m}>0$.

Tables 3.7-3.11 and Figures 3.24-3.28 show, for each test, the comparison between the experimental estimation of β_0 and β_1 and their limit values derived from application of Eqs. (3.60)-(3.63). In particular, in order to obtain a region which confines the experimental estimate of β_0 and β_1, Eqs.(3.60)-(3.63) have been plotted versus axial force by means of dotted line. Symbols correspond to single test evaluations and solid lines represent the average of the experimental data.

TEST 1

N_x [kN]	β_0			β_1		
	Test 1	$k_{s,d} = 0$	$k_{s,d} = \infty$	Test 1	$k_{s,d} = 0$	$k_{s,d} = \infty$
5.662	13.892	9.382	11.564	10.021	9.7868	12.101
10.524	16.036	10.797	12.661	11.091	11.169	13.162
14.978	16.810	11.956	13.601	13.493	12.307	14.076
20.692	18.425	13.299	14.732	14.985	13.632	15.180
24.876	19.157	14.203	15.514	16.177	14.526	15.946
30.712	21.182	15.373	16.550	17.503	15.686	16.962
35.640	21.931	16.295	17.379	18.181	16.601	17.778
40.366	23.395	17.131	18.142	18.733	17.431	18.530
45.577	25.847	18.006	18.949	20.241	18.302	19.326
50.873	25.856	18.853	19.736	20.858	19.144	20.104

Table 3.7 – Average of the experimental parameters and analytical end stiffness, Test 1

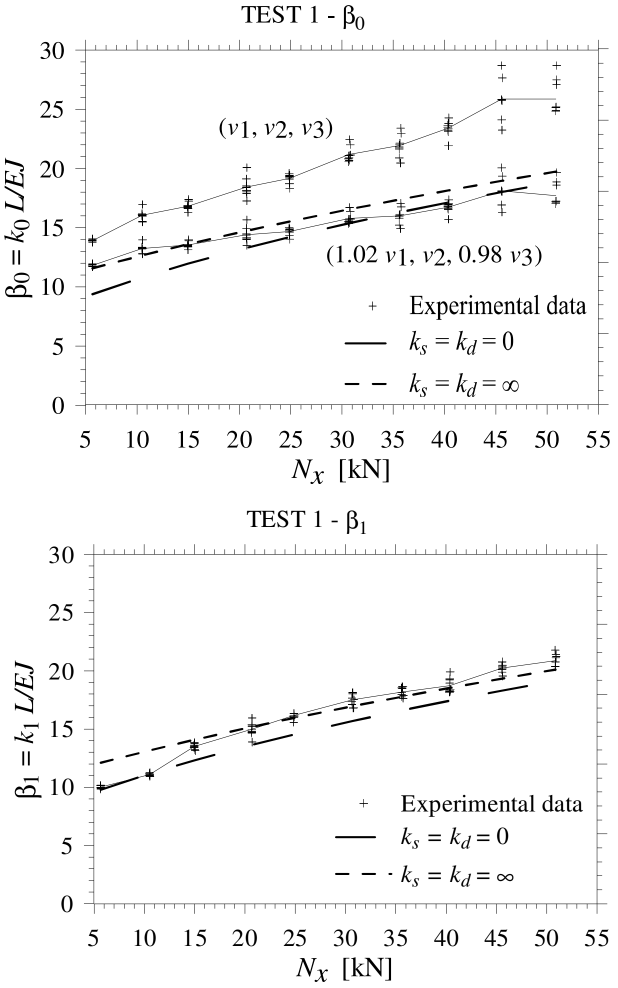

Figure 3.24 – End constraint stiffness of the central span vs tensile force N

TEST 1A – B

N_x [kN]	β_0				β_1			
	Test 1A	Test 1B	$k_{s,d} = 0$	$k_{s,d} = \infty$	Test 1A	Test 1B	$k_{s,d} = 0$	$k_{s,d} = \infty$
4.502	11.728	15.897	9.015	11.290	4.502	9.585	10.242	9.430
10.945	13.558	18.175	10.912	12.752	10.945	11.475	11.998	11.281
15.108	15.702	20.620	11.988	13.628	15.108	12.251	13.957	12.339
20.077	16.689	23.849	13.161	14.614	20.077	13.217	15.291	13.496
24.749	17.866	23.658	14.176	15.491	24.749	14.065	16.111	14.499
30.385	18.588	25.005	15.310	16.493	30.385	15.810	17.861	15.623
34.871	19.561	27.209	16.155	17.252	34.871	16.400	18.864	16.461
40.181	20.466	29.071	17.099	18.112	40.181	17.121	19.790	17.400
45.696	21.276	31.491	18.026	18.967	45.696	18.062	21.309	18.321
49.771	21.314	31.007	18.680	19.575	49.771	19.185	22.152	18.972

Table 3.8 – Average of the experimental parameters and analytical end stiffness, Test 1

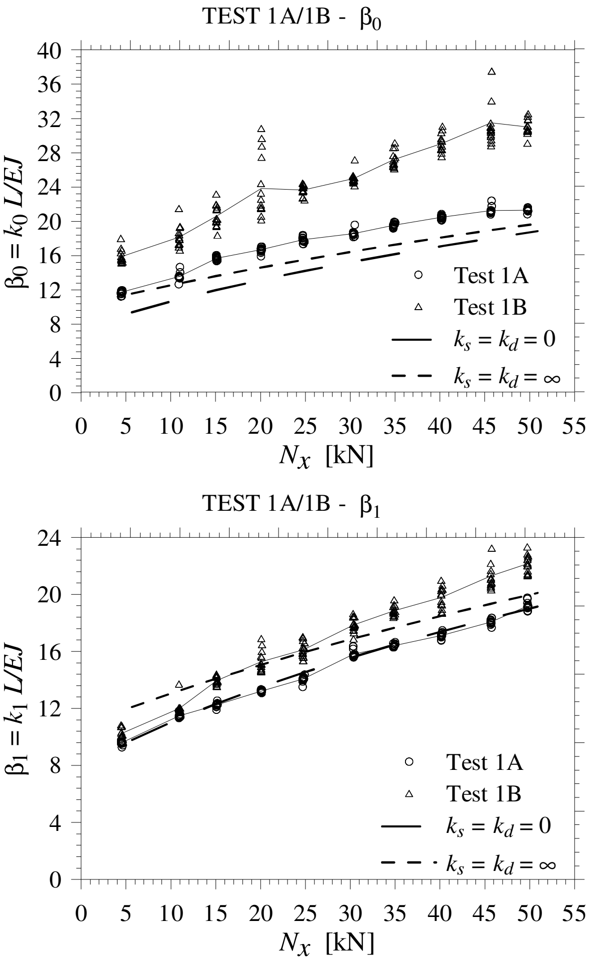

Figure 3.25 – End constraint stiffness of the central span vs tensile force *N*

TEST 3

N_x [kN]	β_0			β_1		
	Test 3	$k_{s,d} = 0$	$k_{s,d} = \infty$	Test 3	$k_{s,d} = 0$	$k_{s,d} = \infty$
4.476	15.693	9.106	11.298	0.771	0.384	7.442
11.371	20.552	11.225	12.874	-3.649	-3.916	4.574
15.610	22.005	12.366	13.776	-5.851	-5.894	2.171
21.049	24.138	13.691	14.873	-8.290	-7.925	-1.256
26.220	37.313	14.840	15.864	-9.207	-9.517	-4.282
29.704	-60.143	15.563	16.504	-10.118	-10.463	-6.023
34.645	55.230	16.531	17.377	-11.730	-11.678	-8.099
41.226	6.257	17.732	18.480	-11.897	-13.123	-10.328

Table 3.9 – Average of the experimental parameters and analytical end stiffness, Test 3 first mode shape

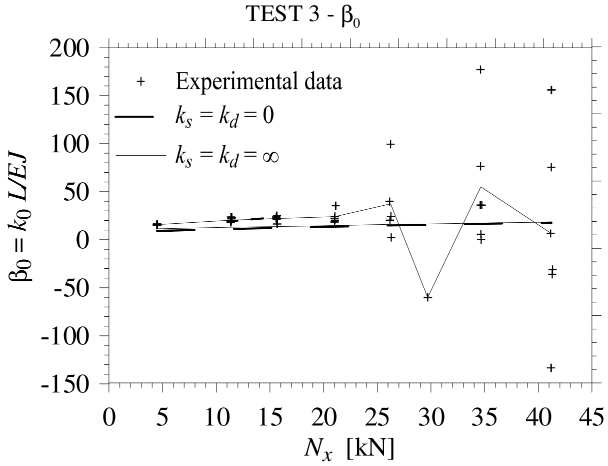

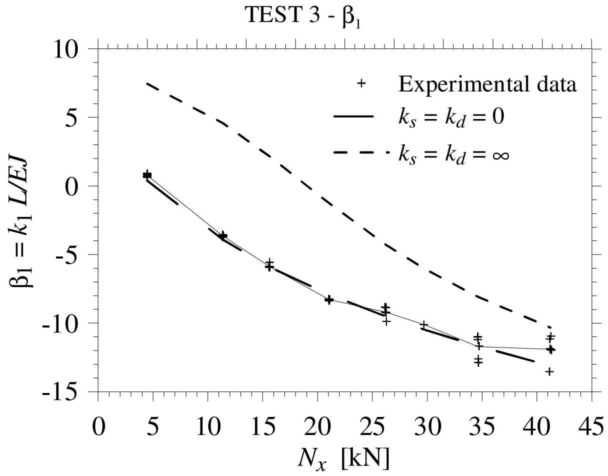

Figure 3.26 – End constraint stiffness of the central span vs tensile force N. Test 3 first mode shape

TEST 3 – Second mode shape

N_x [kN]	$\beta_0^{(II)}$			$\beta_1^{(II)}$		
	Test 3	$k_{s,d} = 0$	$k_{s,d} = \infty$	Test 3	$k_{s,d} = 0$	$k_{s,d} = \infty$
4.476	13.186	8.826	10.999	-41.777	-34.108	-12.334
11.371	14.978	10.931	12.669	334.931	803.960	-21.514
15.610	16.767	12.039	13.605	58.182	93.681	-32.520
21.049	19.144	13.323	14.718	41.146	56.403	-73.342
26.220	20.000	14.437	15.701	36.198	46.244	-843.960
29.704	21.498	15.139	16.328	35.241	42.819	200.280
34.645	21.600	16.080	17.178	33.892	39.940	88.355
41.226	23.384	17.251	18.249	33.246	37.896	59.873

Table 3.10 –Average of the experimental parameters and analytical end stiffness, Test 3 2nd mode shape

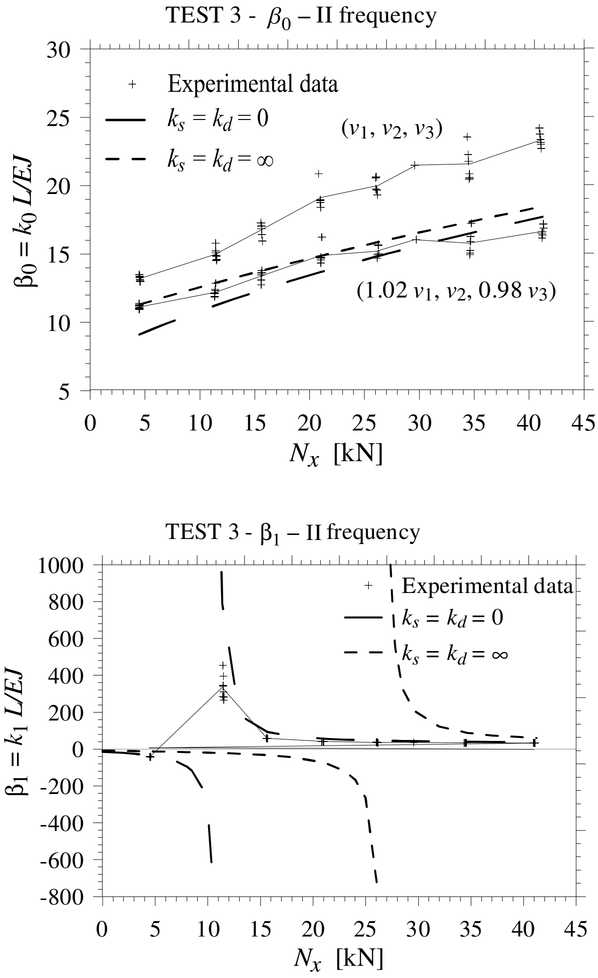

Figure 3.27 – End constraint stiffness of the central span vs tensile force *N*. Test 3 second mode shape

TEST 5

N_x [kN]	β_0			β_1		
	Test 5	$k_{s,d} = 0$	$k_{s,d} = \infty$	Test 5	$k_{s,d} = 0$	$k_{s,d} = \infty$
4.427	14.943	9.019	11.277	6.524	5.529	10.039
10.312	16.278	10.778	12.622	6.024	4.956	10.305
15.170	18.177	12.049	13.649	4.755	4.411	10.480
20.162	19.428	13.231	14.641	5.322	3.784	10.616
25.558	20.445	14.400	15.650	3.636	3.031	10.715
30.960	22.483	15.482	16.605	1.564	2.205	10.764
36.735	25.195	16.559	17.573	-0.463	1.251	10.761
41.016	25.398	17.313	18.259	-2.243	0.504	10,721

Table 3.11 – Average of the experimental parameters and analytical end stiffness, Test 5

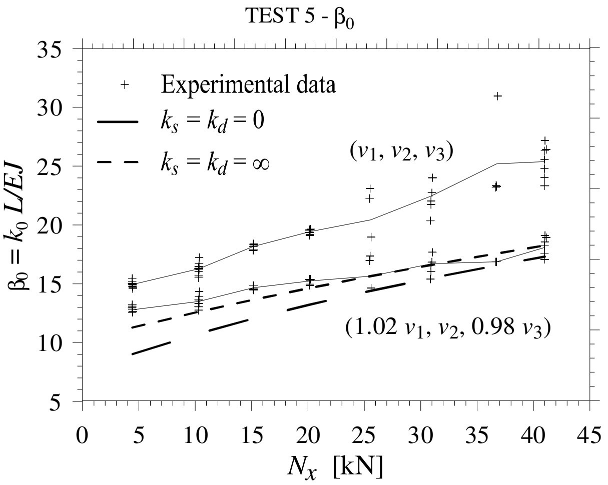

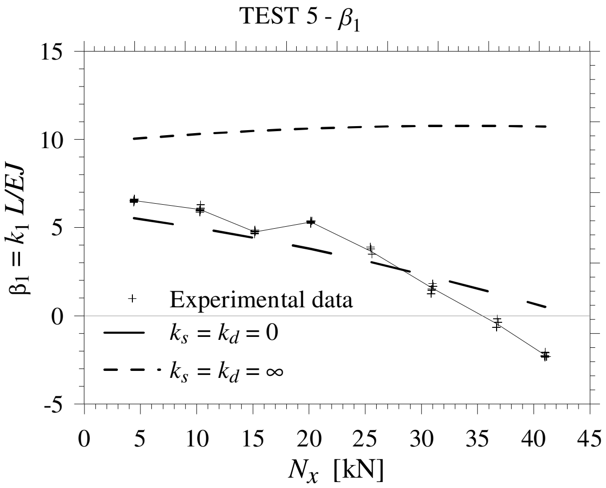

Figure 3.28 – End constraint stiffness of the central span vs tensile force *N*. Test 5

It can be noted that for each test, at the beam end in front of the hydraulic jack, the estimation of the elastic parameter β_1 is quite reasonable. Vice versa, at the opposite end in front of the load cells, β_0 estimation is not satisfactory at all. Yet, if β_0 is calculated with the arbitrary values of 0.98 v_1/v_2 and 1.02 v_3/v_2, the corresponding line is obtained, which is much closer to the limit (dotted lines). Hence, identification of boundary conditions is clearly ill conditioned.

Moreover, it should be noted that the dotted line, corresponding to β_1 with $k_s = k_d = \infty$ for configuration 3 and calculated with the second modal frequency (Figure 3.27), has the same trend of β_1 obtained in the Example 2 in Section 2.6.3.2, (Figure 2.16). The vertical asymptote occurs 3 kN less than the asymptote observed in the example because of the presence of the left beam. However, the limit case of simply supported beam $k_s = k_d = 0$ has a similar trend, even if the vertical asymptote occurs for a lower value of axial force. It is amazing how the data points follow this trend also near the asymptote.

Analogously to the axial load identification, the condensation parameter estimated by means of test 1A is closer to the analytical curves than the parameters which derive from test 1B. Figures 3.26-3.27 clearly shows that the farthest boundary conditions of the beam tend to simple supports.

Finally, it can be noted that the region between the dotted lines, corresponding to the two limit conditions, is considerably wider for the frames with the lumped mass in span. Hence, it provides a better identification of the end stiffness of the central beam than the identification made for the other tests.

3.2.6.4 Comparison between PPM and PRMI for the experimental modal analysis

With the aim of making a comparison between the dynamic identifications by means of PPM and PRMI, dynamic parameters and identified mechanical quantities for configuration 5 have been analyze with both methods. In particular tests for axial load about 5 kN, 10 kN, 20 kN and 35 kN have been considered, (Table 3.12). It can be noted that the difference between the two methods is absolutely negligible, and the simpler peak picking method can be adopted.

3.3 Axial load identification by means of static tests

Adopting Euler-Bernoulli beam model, this section shows that, if bending stiffness and mass per unit length of a beam with constant cross section are known, the axial force and the flexural stiffness of the end constraints can be deduced by three displacements recorded at three instrumented sections along the beam length, after the application of a transversal static force.

N_x [kN]	4.427		10.312		20.177		36.691	
Method	PPM	PRMI	PPM	PRMI	PPM	PRMI	PPM	PRMI
f [Hz]	10.605	10.605	13.453	13.459	17.214	17.207	21.616	21.618
v_1	0.6049	0.6049	0.6166	0.6187	0.6301	0.6313	0.6337	0.6340
v_2	1.0000	1.0000	1.0000	1.0000	1.0000	1.0000	1.0000	1.0000
v_3	0.6718	0.6718	0.6841	0.6836	0.6974	0.6963	0.7364	0.7364
λ	4.839	4.839	5.450	5.451	6.165	6.164	6.908	6.909
$(v_1+v_3)/2v_2$	0.6384	0.6384	0.6504	0.6511	0.6638	0.6638	0.6850	0.6852
N_a [kN]	4.380	4.380	10.167	10.229	20.062	20.045	36.279	36.307
β_0	14.943	14.943	16.997	16.278	19.889	19.428	25.326	25.195
β_1	6.524	6.524	6.054	6.024	5.187	5.322	-0.442	-0.463

Table 3.12 – Comparison between the parameters identified by mean of PPM and PRMI for some axial load imposed in Test 5

3.3.1 Governing equations

The reference model is constituted by a simply supported prismatic beam of length L, constrained by two end elastic-springs having k_0 and k_1 flexural stiffness, subjected to an axial force N (positive sign is assigned to tensile forces) and to a vertical force P at $x = a$. Young's modulus E, mass per unit length m and cross-section second area moment J are assumed to be constant, and known as well (Figure 3.29).

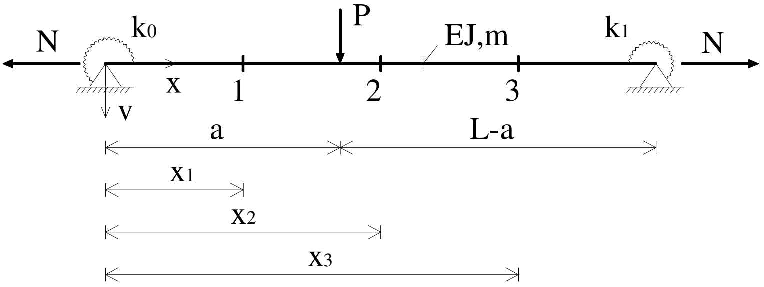

Figure 3.29 – Beam with end flexural constraints and location of the instrumented sections

As well as the previous section, the condensation parameters of boundary conditions reduce to the static contribute of $\mathbf{D}(\omega)$:

$$\mathbf{K}_0 = \begin{bmatrix} 0 & 0 \\ 0 & k_0 \end{bmatrix} \qquad \mathbf{K}_1 = \begin{bmatrix} 0 & 0 \\ 0 & k_1 \end{bmatrix} \tag{3.64}$$

Making use of the nondimensional coordinate $z = x/L$ and neglecting shear deformation, Eq. (1.33) reduces to

$$v''''(z) - nv''(z) = 0 \tag{3.65}$$

To solve Eq. (3.65) is necessary to subdivide the beam length in two subintervals, one before the vertical force and an another after it. Consequently the two solutions of the field equation are

$$\begin{aligned} v_{\mathrm{I}}(z) &= C_1 \cosh\sqrt{n}\,z + C_2 \sinh\sqrt{n}\,z + C_3 z + C_4 \qquad && 0 \le z \le \alpha \\ v_{\mathrm{II}}(z) &= C_5 \cosh\sqrt{n}\,z + C_6 \sinh\sqrt{n}\,z + C_7 z + C_8 \qquad && \alpha \le z \le 1 \end{aligned} \tag{3.66}$$

Boundary and internal conditions, respectively (1.43) and (1.74), reduce to

$$\text{Boundary conditions} \qquad \begin{cases} v(0) = 0 \\ v_{\mathrm{I}}''(0) - \beta_0 v_{\mathrm{I}}'(0) = 0 \\ v_{\mathrm{II}}(1) = 0 \\ v_{\mathrm{II}}''(1) + \beta_1 v_{\mathrm{II}}'(1) = 0 \end{cases} \tag{3.67}$$

$$\text{Internal conditions} \qquad \begin{cases} v_{\mathrm{I}}(\alpha) - v_{\mathrm{II}}(\alpha) = 0 \\ v_{\mathrm{I}}'(\alpha) - v_{\mathrm{II}}'(\alpha) = 0 \\ v_{\mathrm{I}}'''(\alpha) - v_{\mathrm{II}}'''(\alpha) = -\psi \\ v_{\mathrm{I}}''(\alpha) - v_{\mathrm{II}}''(\alpha) = 0 \end{cases} \tag{3.68}$$

where prime means derivation with respect to z and

$$\beta_0 = \frac{k_0 L}{EJ} \qquad \beta_1 = \frac{k_1 L}{EJ} \qquad n = \frac{NL^2}{EJ} \qquad \alpha = \frac{a}{L} \qquad \psi = \frac{PL^3}{EJ} \tag{3.69}$$

It is worth noting that the load parameter Ψ has the dimension of a length.

3.3.2 Valuation of parameters

In order to identify the axial load N and the stiffness k_0 and k_1 of the end flexural constraints, knowledge is required of three transversal displacements recorded at three location coordinates x_1, x_2 and x_3 (Figure 3.29), due to the application of the static force

P. With reference to the nondimensional coordinate $z = x/L$, three displacements are determined and denoted by $v_i = v(x_i)$ for $i = 1,2,3$.

Hence, the constants $C_1 - C_8$ can be determined from the solution of the system (3.70), constituted by the five boundary and internal conditions which do not depend on the stiffness parameters (first and third equations in (3.67) and Eqs.(3.68) except the third), together with the three experimental records of transversal displacements.

$$\begin{cases} v_{\mathrm{I}}(0)=0 & \\ v_{\mathrm{II}}(1)=0 & \\ v_{\mathrm{I}}(\alpha)-v_{\mathrm{II}}(\alpha)=0 & \text{Boundary and internal conditions} \\ v'_{\mathrm{I}}(\alpha)-v'_{\mathrm{II}}(\alpha)=0 & \\ v''_{\mathrm{I}}(\alpha)-v''_{\mathrm{II}}(\alpha)=0 & \\ v_{\mathrm{I}}(z_1)=v_1 & \\ v_{\mathrm{I}}(z_2)=v_2 & \text{Experimental records} \\ v_{\mathrm{II}}(z_3)=v_3 & \end{cases} \tag{3.70}$$

Substituting Eqs. (3.66) in (3.70), an homogeneous linear system in the eight unknowns C_1-C_8 is obtained:

$$\begin{cases} C_1+C_4=0 \\ C_5\cosh\sqrt{n}+C_6\sinh\sqrt{n}+C_7+C_8=0 \\ (C_1-C_5)\cosh\alpha\sqrt{n}+(C_2-C_6)\sinh\alpha\sqrt{n}+(C_3-C_7)\alpha+C_4-C_8=0 \\ (C_1-C_5)\sqrt{n}\sinh\alpha\sqrt{n}+(C_2-C_6)n\cosh\alpha\sqrt{n}+C_3-C_7=0 \\ (C_1-C_5)\cosh\alpha\sqrt{n}+(C_2-C_6)\sinh\alpha\sqrt{n}=0 \\ C_1\cosh\sqrt{n}\,z_1+C_2\sinh\sqrt{n}\,z_1+C_3z_1+C_4-v_1=0 \\ C_1\cosh\sqrt{n}\,z_2+C_2\sinh\sqrt{n}\,z_2+C_3z_2+C_4-v_2=0 \\ C_5\cosh\sqrt{n}\,z_3+C_6\sinh\sqrt{n}\,z_3+C_7z_3+C_8-v_3=0 \end{cases} \tag{3.71}$$

Coefficient C_1, C_2 and C_8 are linear functions of the three (experimental) displacements v_1, v_2, v_3, and depend on the unknown parameter n. Once the constants C_1-C_8 have been determined, by imposing the third internal condition Eqs. (3.68), the following equation is obtained, to be solved for the unknown constant n:

$$\left[C_2(n)-C_6(n)\right]\cosh\alpha\sqrt{n}+\left[C_1(n)-C_5(n)\right]\sinh\alpha\sqrt{n}+\frac{\psi}{n^{3/2}}=0 \tag{3.72}$$

Therefore, regardless of any boundary conditions as well as dynamic procedure of Section 3.2.2, the axial force identification is obtained.

Finally, the second and the fourth boundary conditions Eq. (3.67) yields coefficients β_0 and β_1.

$$\begin{cases}\beta_0=\dfrac{v_{\mathrm{I}}''(0)}{v_{\mathrm{I}}'(0)}=\dfrac{C_3(n)+C_2(n)\sqrt{n}}{C_1(n)n}\\[2ex] \beta_1=-\dfrac{v_{\mathrm{II}}''(1)}{v_{\mathrm{II}}'(1)}=\dfrac{C_5(n)\sqrt{n}\sinh\sqrt{n}+C_6(n)\sqrt{n}\cosh\sqrt{n}+C_7(n)}{n\left(C_5(n)\cosh\sqrt{n}+C_6(n)\sinh\sqrt{n}\right)}\end{cases} \tag{3.73}$$

The above formulation can be simplified if control points and the transversal load are assumed at sections having nondimensional coordinates $z_1 = 1/4$, $z_2 = 1/2$ and $z_3 = 3/4$.

In the next section, the solving equations for load position at $\alpha = 1/4$ and $\alpha = 1/2$ are derived.

3.3.2.1 Vertical load in the midspan

The vertical load and the instrumented section assume the position depicted in Figure 3.30.

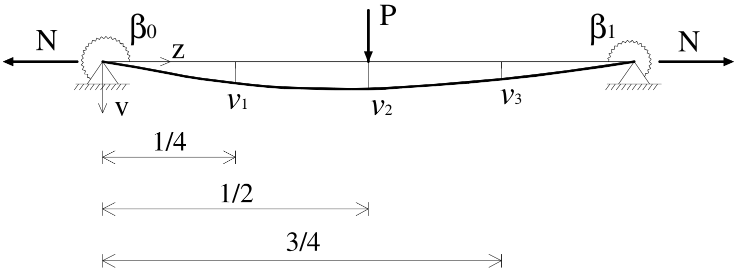

Figure 3.30 – Reference beam with instrumented sections at the quarter of the span and P at $\alpha = 1/2$

For $z_1 = 1/4$, $z_2 = 1/2$, $z_3 = 3/4$ and $\alpha = 1/2$, Eqs. (3.72) and (3.73) yield

$$\frac{v_1+v_3}{v_2}=\frac{1+2\cosh\left(\sqrt{n}/4\right)}{1+\cosh\left(\sqrt{n}/4\right)}+\frac{\psi/v_2\left(\sqrt{n}-4\sinh\left(\sqrt{n}/4\right)\right)}{4n^{3/2}\left(1+\cosh\left(\sqrt{n}/4\right)\right)} \tag{3.74}$$

$$\beta_0=\frac{a\left(v_1/v_2\right)-b}{c\left(v_1/v_2\right)-d} \qquad \beta_1=\frac{a\left(v_3/v_2\right)-b}{c\left(v_3/v_2\right)-d} \tag{3.75}$$

where constants a, b, c, d are given by the following relations:

$$
\begin{aligned}
a &= 16n^{5/2}\sinh\frac{n}{2}\\
b &= 2n\tanh\frac{\sqrt{n}}{8}\left(4n^{3/2}\left(2+2\cosh\frac{\sqrt{n}}{4}+\cosh\frac{\sqrt{n}}{2}\right)+\frac{\psi}{v_2}\left(2\sinh\frac{\sqrt{n}}{2}-\sqrt{n}\right)\right)\\
c &= -16n^{3/2}\left(\sqrt{n}\cosh\frac{\sqrt{n}}{2}-2\sinh\frac{\sqrt{n}}{2}\right)\\
d &= \operatorname{sech}^2\frac{\sqrt{n}}{8}\biggl(-2n^{3/2}\biggl(3\sqrt{n}\cosh\frac{\sqrt{n}}{4}+\left(1+2\cosh\frac{\sqrt{n}}{4}\right)\biggl(-\sqrt{n}+\sqrt{n}\cosh\frac{\sqrt{n}}{4}+\\
&\quad +n\cosh\frac{\sqrt{n}}{2}-4\sinh\frac{\sqrt{n}}{2}\biggr)\biggr)+\frac{\psi}{v_2}\biggl(\left(-4+n\right)\cosh\frac{\sqrt{n}}{4}+4\cosh\frac{3\sqrt{n}}{4}+\\
&\quad -\sqrt{n}\left(5\sinh\frac{\sqrt{n}}{4}+\sinh\frac{3\sqrt{n}}{4}\right)\biggr)\biggr)
\end{aligned}
\tag{3.76}
$$

It can be noted that, except for the term corresponding to the vertical load, Eq. (3.74) and (3.75) have the same forms of the equation obtained in Section 3.2.2 for the axial load identification by means of dynamic test, Eqs. (3.12) and (3.13). Indeed, when the circular frequency goes to zero, Eq. (3.12) reduce to Eq. (3.74) with $\Psi = 0$.

Moreover, Eq. (3.74) seems to contain the paradox that the displacements amplitude $(v_1+v_3)/v_2$ ratio is a function of the axial force n also with null vertical load. In seek of convenience, a pinned-pinned beam without axial force and subjected to a transversal load in the midspan is now considered (Figure 3.31).

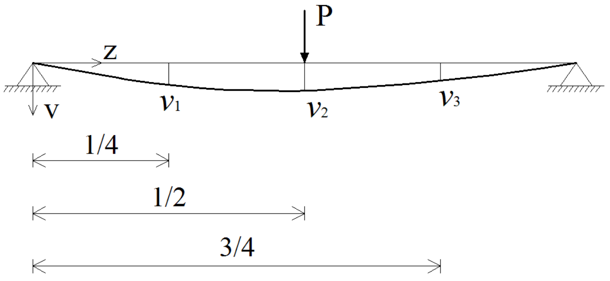

Figure 3.31 – Pinned-pined beam subjected to a transversal load in the middle of the span

The corresponding displacements at the marked sections are the following:

$$
v_1 = \frac{11}{768}\psi \qquad v_2 = \frac{1}{48}\psi \qquad v_3 = \frac{11}{768}\psi \tag{3.77}
$$

Hence, the displacement ratio becomes

$$\frac{v_1+v_3}{v_2}=\frac{11}{8} \tag{3.78}$$

Taking the limit for *n* tending to zero, Eq. (3.74) reduces to:

$$\frac{v_1+v_3}{v_2}=\lim_{n\to 0}\frac{1+2\cosh\left(\sqrt{n}/4\right)}{1+\cosh\left(\sqrt{n}/4\right)}+\frac{\psi\left(\sqrt{n}-4\sinh\left(\sqrt{n}/4\right)\right)}{4v_2 n^{3/2}\left(1+\cosh\left(\sqrt{n}/4\right)\right)}=\frac{3}{2}-\frac{\psi}{384v_2} \tag{3.79}$$

Eqs. (3.78) and (3.79) are equivalent; indeed, substituting the expression of v_2, Eqs. (3.77)b, in Eq. (3.79), Eqs. (3.78) is obtained. Hence, Eq. (3.74) does not describe the relationship between the displacements at the quarters of the beam span versus the vertical load applied, but it only evaluates the transversal stiffness in these sections.

3.3.2.2 Transversal load in the middle of the span

In this section the transversal load and the instrumented section assume the position depicted in Figure 3.32.

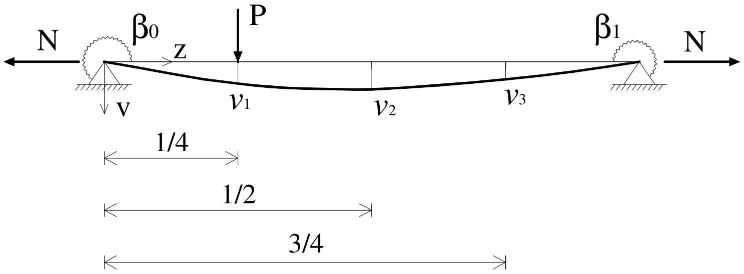

Figure 3.32 – Reference beam with instrumented sections in the quarter of the span and *P* at α = 1/4

For z_1 = 1/4, z_2 = 1/2, z_3 = 3/4 and α = 1/4, Eqs. (3.72) and (3.73) yield

$$\frac{v_1+v_3}{v_2}=\frac{1+2\cosh\left(\sqrt{n}/4\right)}{1+\cosh\left(\sqrt{n}/4\right)}+\frac{\psi/v_2\left(\sqrt{n}-4\sinh\left(\sqrt{n}/4\right)\right)}{8n^{3/2}\left(1+\cosh\left(\sqrt{n}/4\right)\right)} \tag{3.80}$$

$$\beta_0=\frac{a_1\left(v_1/v_2\right)-b_1}{c_1\left(v_1/v_2\right)-d_1} \qquad \beta_1=\frac{a_3\left(v_3/v_2\right)-b_3}{c_3\left(v_3/v_2\right)-d_3} \tag{3.81}$$

where constants a_1, b_1,…, d_3 are given by the following relations:

$$
\begin{aligned}
a_1 &= 32n^{5/2}\sinh\frac{\sqrt{n}}{2}\\
b_1 &= 2n\tanh\frac{\sqrt{n}}{8}\Bigg(8n^{3/2}\Bigg(2+2\cosh\frac{\sqrt{n}}{4}+\cosh\frac{\sqrt{n}}{2}\Bigg)+\frac{\psi}{v_2}\Bigg(\sqrt{n}\Bigg(1+4\cosh\frac{\sqrt{n}}{4}+\\
&\quad +2\cosh\frac{\sqrt{n}}{2}-12\sin\frac{\sqrt{n}}{4}-8\sinh\frac{\sqrt{n}}{2}\Bigg)\Bigg)\\
c_1 &= -32n^{3/2}\Bigg(\sqrt{n}\cosh\frac{\sqrt{n}}{2}-2\sinh\frac{\sqrt{n}}{2}\Bigg)\\
d_1 &= \operatorname{sech}^2\frac{\sqrt{n}}{8}\Bigg(-4n^{3/2}\Bigg(3\sqrt{n}\cosh\frac{\sqrt{n}}{4}+\Bigg(1+2\cosh\frac{\sqrt{n}}{4}\Bigg)\Bigg(-\sqrt{n}+\sqrt{n}\cosh\frac{\sqrt{n}}{4}+\\
&\quad +\sqrt{n}\cosh\frac{\sqrt{n}}{2}-4\sinh\frac{\sqrt{n}}{2}\Bigg)\Bigg)-\frac{\psi}{v_2}\Bigg(n\Bigg(2\cosh\frac{\sqrt{n}}{2}+\cosh\frac{3\sqrt{n}}{4}\Bigg)+2\sqrt{n}\Bigg(6\sinh\frac{\sqrt{n}}{4}+\\
&\quad -3\sinh\frac{\sqrt{n}}{2}-4\sinh\frac{3\sqrt{n}}{4}\Bigg)+8\Bigg(-\cosh\frac{\sqrt{n}}{4}+\cosh\frac{\sqrt{n}}{2}+\cosh\frac{3\sqrt{n}}{4}-1\Bigg)\Bigg)\Bigg)\\
a_3 &= 32n^{5/2}\sinh\frac{\sqrt{n}}{2}\\
b_3 &= 2n\tanh\frac{\sqrt{n}}{8}\Bigg(8n^{3/2}\Bigg(2+2\cosh\frac{\sqrt{n}}{4}+\cosh\frac{\sqrt{n}}{2}\Bigg)+\frac{\psi}{v_2}\Bigg(4\sinh\frac{\sqrt{n}}{4}-\sqrt{n}\Bigg)\Bigg)\\
c_3 &= -32n^{3/2}\Bigg(\sqrt{n}\cosh\frac{\sqrt{n}}{2}-2\sinh\frac{\sqrt{n}}{2}\Bigg)\\
d_3 &= -\operatorname{sech}^2\frac{\sqrt{n}}{8}\Bigg(4n^2\Bigg(3\cosh\frac{\sqrt{n}}{4}+2\cosh\frac{\sqrt{n}}{2}+\cosh\frac{3\sqrt{n}}{4}\Bigg)+\\
&\quad -16n^{3/2}\Bigg(\sinh\frac{\sqrt{n}}{2}+\sinh\frac{\sqrt{n}}{2}+\sinh\frac{3\sqrt{n}}{4}\Bigg)+\frac{\psi}{v_2}\Bigg(8-n\cosh\frac{\sqrt{n}}{4}-8\cosh\frac{\sqrt{n}}{2}+\\
&\quad +4\sqrt{n}\sinh\frac{\sqrt{n}}{4}+2\sqrt{n}\sinh\frac{\sqrt{n}}{2}\Bigg)\Bigg)
\end{aligned}
\tag{3.82}
$$

It can be noted that, despite of the increased complexity of the parameters, the structure of the equations is preserved. Moreover, it can be proved that, if the vertical load is applied at section $z = 3/4$, the same results are obtained and the expressions of β_0 and β_1 are switched.

3.3.3 Laboratory tests

In order to apply the analytical procedure derived in the previous section, a set of experimental tests have been organized. The specimen and the configuration adopted are the same of the test 1 of Section 3.2.4 (Figure 3.33).

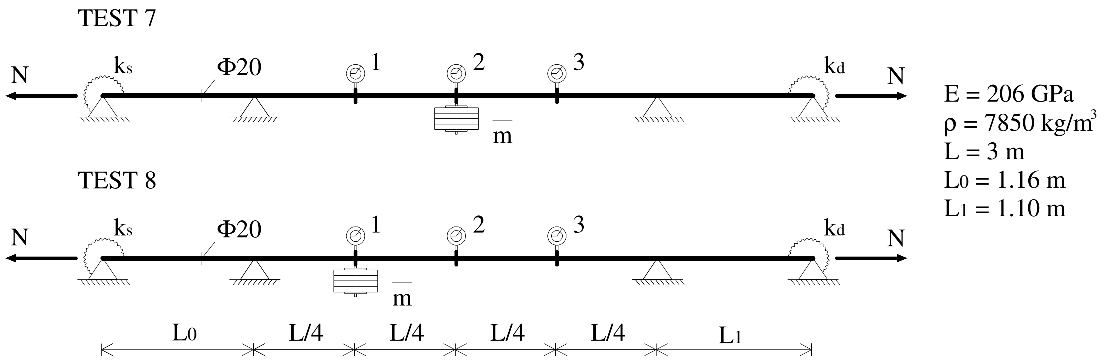

Figure 3.33 – Experimental frame configuration

The vertical load was applied by means of cast iron discs fastened at the middle of the central span of the frame (test 7) and at its first quarter (test 8), as depicted in Figure 3.34. The displacements were measured making use of three centesimal comparators with accuracy of 0.01 mm. The end supports were realized by means of the connection with hydraulic jack (right side) and load cells (left side), see Figure 3.5, 3.6 and 3.8.

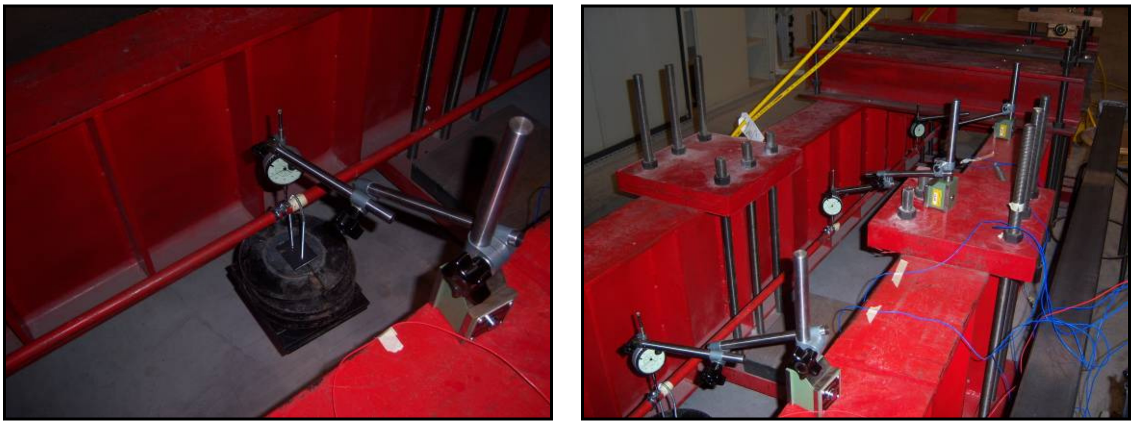

Figure 3.34 – Cast iron discs fastened to the beam and arrangement of the comparators

For each axial load, the transversal force was increased adding iron discs and reaching a mass of 6, 14, and 22 kg, corresponding to vertical loads of about 59 N, 137 N and 216 N respectively. Then, the corresponding displacements at the instrumented sections were recorded. Hence, for each axial load imposed, three terns of displacements have been recorded, so three experimental estimates of the axial force and the stiffness end constraints are made possible. It is worth specifying that the maximum axial force and the greater mass placed, 40 kN and 22 kg respectively, do not yield the beam.

3.3.4 Results

3.3.4.1 Experimental data

Tables 3.13-3.20 show the experimental data corresponding to transversal load applied in the midspan (test 7) and at the first quarter of the span (test 8), for each value of axial load imposed N_X. The two last lines in the tables represent the displacements for the unloading path.

Tables clearly show that in the unloading path the displacements recorded at each instrumented section reach the same value reached in the loading path. Moreover, in order to confirm the elastic behaviour of the specimen, the ratio between the vertical load ΔP and the corresponding displacements Δv has been plotted versus the vertical load for each value of N_X. Since the ratio represents the transversal stiffness of the beam, the experimental data show almost constant lines with greater values as the axial load increases. For instance, Figure 3.35 shows the case for displacement v_1 of test 7.

N_X = 4.15 kN		Test 7			Test 8		
P [N]	Ψ [mm]	v_1 [mm]	v_2 [mm]	v_3 [mm]	v_1 [mm]	v_2 [mm]	v_3 [mm]
59	981.86	2.43	4.24	2.40	2.24	2.44	1.13
137	2291.00	5.66	9.83	5.49	5.46	5.82	2.69
216	3600.20	8.67	14.94	8.38	8.64	9.07	4.22
137	2291.00	5.66	9.81	5.50	5.60	5.83	2.68
59	981.86	2.42	4.21	2.39	2.39	2.48	1.13

Table 3.13 – Displacements recorded for test 7 and 8, N_X = 4.15 kN

N_X = 10.42 kN		Test 7			Test 8		
P [N]	Ψ [mm]	v_1 [mm]	v_2 [mm]	v_3 [mm]	v_1 [mm]	v_2 [mm]	v_3 [mm]
59	981.86	1.34	2.43	1.31	1.46	1.38	0.61
137	2291.00	3.18	5.68	3.09	3.42	3.23	1.44
216	3600.20	5.01	8.89	4.87	5.40	5.10	2.29
137	2291.00	3.19	5.7	3.08	3.42	3.24	1.44
59	981.86	1.35	2.44	1.30	1.46	1.38	0.62

Table 3.14 – Displacements recorded for test 7 and 8, N_X = 10.42 kN

N_X = 14.90 kN		Test 7			Test 8		
P	Ψ	v_1	v_2	v_3	v_1	v_2	v_3
[N]	[mm]	[mm]	[mm]	[mm]	[mm]	[mm]	[mm]
59	981.86	1.06	1.94	1.04	1.19	1.09	0.50
137	2291.00	2.51	4.54	2.44	2.79	2.53	1.14
216	3600.20	3.93	7.09	3.74	4.41	4.00	1.81
137	2291.00	2.51	4.53	2.46	2.80	2.54	1.14
59	981.86	1.06	1.94	1.05	1.19	1.07	0.49

Table 3.15 – Displacements recorded for test 7 and 8, N_X = 14.90 kN

N_X = 20.10 kN		Test 7			Test 8		
P	Ψ	v_1	v_2	v_3	v_1	v_2	v_3
[N]	[mm]	[mm]	[mm]	[mm]	[mm]	[mm]	[mm]
59	981.86	0.84	1.53	0.81	0.97	0.86	0.40
137	2291.00	1.98	3.57	1.92	2.28	1.99	0.91
216	3600.20	3.11	5.63	3.02	3.60	3.15	1.44
137	2291.00	1.99	3.62	1.92	2.30	1.99	0.90
59	981.86	0.85	1.53	0.82	0.98	0.85	0.40

Table 3.16 – Displacements recorded for test 7 and 8, N_X = 20.10 kN

N_X = 25.30 kN		Test 7			Test 8		
P	Ψ	v_1	v_2	v_3	v_1	v_2	v_3
[N]	[mm]	[mm]	[mm]	[mm]	[mm]	[mm]	[mm]
59	981.86	0.70	1.29	0.69	0.83	0.70	0.32
137	2291.00	1.64	3.00	1.59	1.94	1.65	0.75
216	3600.20	2.58	4.73	2.51	3.05	2.59	1.19
137	2291.00	1.65	3.02	1.60	1.95	1.69	0.75
59	981.86	0.71	1.30	0.69	0.84	0.72	0.33

Table 3.17 – Displacements recorded for test 7 and 8, N_X = 25.30 kN

N_X = 30.20 kN		Test 7			Test 8		
P	Ψ	v_1	v_2	v_3	v_1	v_2	v_3
[N]	[mm]	[mm]	[mm]	[mm]	[mm]	[mm]	[mm]
59	981.86	0.59	1.11	0.58	0.73	0.61	0.28
137	2291.00	1.39	2.61	1.36	1.7	1.42	0.65
216	3600.20	2.19	4.08	2.14	2.69	2.24	1.03
137	2291.00	1.4	2.6	1.36	1.71	1.43	0.64
59	981.86	0.6	1.11	0.58	0.74	0.61	0.27

Table 3.18 – Displacements recorded for test 7 and 8, N_X = 30.20 kN

N_X = 35.00 kN		Test 7			Test 8		
P	Ψ	v_1	v_2	v_3	v_1	v_2	v_3
[N]	[mm]	[mm]	[mm]	[mm]	[mm]	[mm]	[mm]
59	981.86	0.53	0.98	0.51	0.65	0.53	0.24
137	2291.00	1.24	2.29	1.2	1.51	1.24	0.56
216	3600.20	1.94	3.61	1.88	2.39	1.97	0.9
137	2291.00	1.24	2.31	1.22	1.52	1.25	0.56
59	981.86	0.54	0.99	0.51	0.64	0.53	0.25

Table 3.19 – Displacements recorded for test 7 and 8, N_X = 35.00 kN

N_X = 40.00 kN		Test 7			Test 8		
P	Ψ	v_1	v_2	v_3	v_1	v_2	v_3
[N]	[mm]	[mm]	[mm]	[mm]	[mm]	[mm]	[mm]
59	981.86	0.46	0.86	0.45	0.58	0.47	0.22
137	2291.00	1.09	2.03	1.06	1.36	1.1	0.51
216	3600.20	1.71	3.19	1.67	2.15	1.73	0.81
137	2291.00	1.09	2.04	1.07	1.36	1.12	0.5
59	981.86	0.46	1.86	0.45	0.58	0.48	0.22

Table 3.20 – Displacements recorded for test 7 and 8, N_X = 40.00 kN

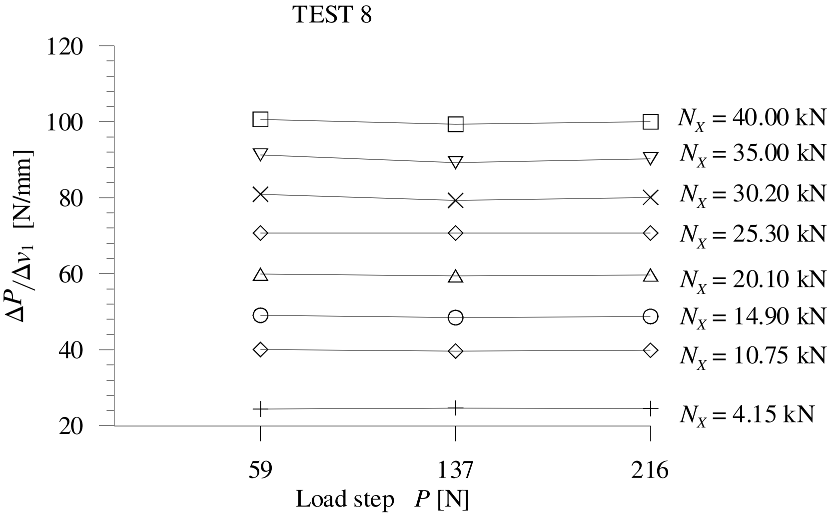

Figure 3.35 – $\Delta P/\ \Delta v$ vs. load step, for transversal force at the first quarter of the span

3.3.4.2 Axial load identification

Estimated axial load N_a may be found by solving Eqs. (3.74) and (3.80) for the experimental data [ψ, v_1, v_2, v_3] collected in Tables 3.13-3.20 for test 7 and 8 respectively.

Figures 3.36-3.37 compare measured N_X and estimated N_a axial force for each test. The graphs show excellent agreement only for test 7 (vertical load in the beam midspan), with an average error less than 3%, whereas an average error of about 9% has been observed for test 8. Probably, a vertical load close to a support makes the beam deflection more subjected to measurement errors. Nonetheless, the percent errors decreases significantly for high values of N_X.

Hence, the procedure can be safely adopted if the vertical load is applied at the beam midspan.

N_X [kN]	N_a [kN]	Δ [%]
4.15	4.061	-2.18
10.75	10.397	-3.40
14.90	14.219	-4.79
20.10	19.958	-0.71
25.30	24.733	-2.29
30.20	28.940	-4.35
35.00	34.164	-2.45
40.00	39.677	-0.81

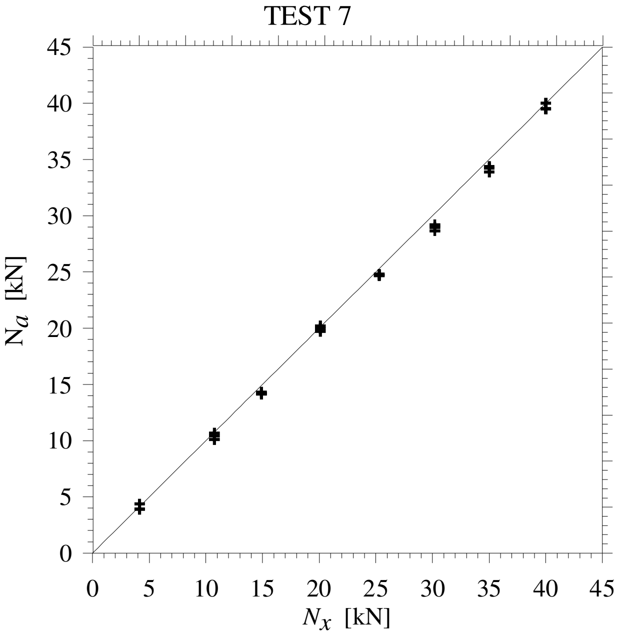

Figure 3.36 – Displacements recorded for test 7 and 8, N_X = 40.00 kN

N_X [kN]	N_a [kN]	Δ [%]
4.15	3.039	-36.56
10.75	9.708	-10.73
14.90	13.957	-6.75
20.10	19.213	-4.62
25.30	24.690	-2.47
30.20	28.957	-4.29
35.00	33.267	-5.21
40.00	39.536	-1.17

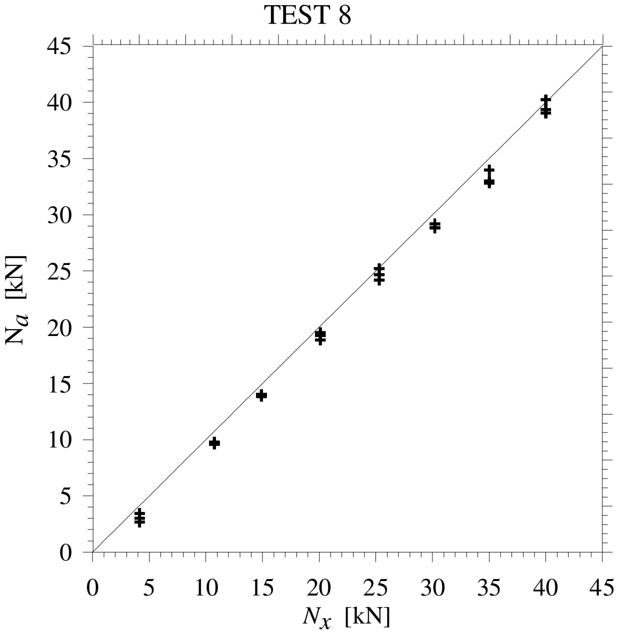

Figure 3.37 – Displacements recorded for test 7 and 8, N_X = 40.00 kN

3.3.4.3 End stiffness identification

As for the end stiffness identification, Eqs. (3.75) and (3.81) give estimation of the static flexural stiffness β_0 and β_1 for test 7 and 8 respectively.

As in Section 3.2.6.3, the analytical investigation considered the limit cases $k_s = k_d = 0$ and $k_s = k_d = \infty$ only, because of the difficulty of evaluating the rotational stiffness introduced by the experimental equipment. For the limit cases considered, the stiffness coefficients β_0 and β_1 of the central beam (Figure 3.38) take the values (Bazant and Cedolin 1991):

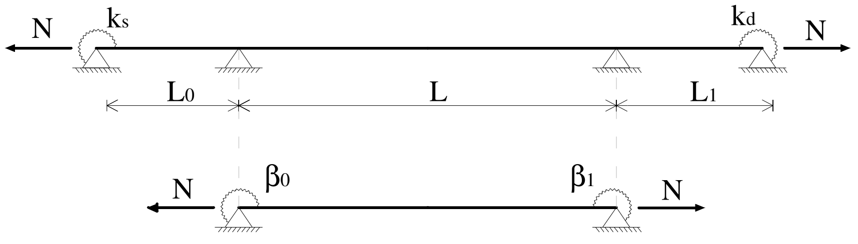

Figure 3.38 – Reference model for the analytical evaluation of the end stiffness coefficients

$$\beta_0 = \frac{3L}{L_0}\frac{1}{I_1(\alpha_s)} \quad \text{for } k_s = 0, \qquad \beta_0 = \frac{4L}{L_1}\frac{3I_1(\alpha_s)}{I_1^2(\alpha_s) - I_2^2(\alpha_s)} \quad \text{for } k_s = \infty \tag{3.83}$$

$$\beta_1 = \frac{3L}{L_1}\frac{1}{I_1(\alpha_0)} \quad \text{for } k_d = 0, \qquad \beta_1 = \frac{4L}{L_1}\frac{3I_1(\alpha_1)}{I_1^2(\alpha_1) - I_2^2(\alpha_1)} \quad \text{for } k_d = \infty \tag{3.84}$$

where $\alpha_0 = L_1/L\sqrt{n}$, $\alpha_1 = L_1/L\sqrt{n}$ and

$$I_1(\alpha) = -\frac{3}{\alpha}\left(\frac{1}{\alpha} - \frac{1}{\tanh\alpha}\right), \quad I_2(\alpha) = \frac{6}{\alpha}\left(\frac{1}{\sin\alpha} - \frac{1}{\alpha}\right) \quad \text{for } \alpha = \alpha_0, \alpha_1 \tag{3.85}$$

It is worth noting that, considering the equation of the dynamic condensation parameter of Section 1.5.4 and Section 1.5.2 and taking the limit for ω tending to zero, Eq. (1.88) and Eq. (1.82) reduce to Eq. (3.83) and (3.84).

Tables 3.21-3.22 and Figures 3.39-3.40 show, for each test, the comparison between the experimental estimation of β_0 and β_1 and their limit values derived from application of Eqs. (3.83) and (3.84). It can be noted that the experimental estimates of β_0 and β_1 are very scattered and do not match the expected region at all. Therefore, identification of boundary conditions are clearly ill conditioned.

TEST 7

N_x [kN]	β_0			β_1		
	Test 7.	$k_{s,d} = 0$	$k_{s,d} = \infty$	Test 7	$k_{s,d} = 0$	$k_{s,d} = \infty$
4.15	9.181	9.283	11.328	11.920	9.743	11.995
10.75	12.040	11.443	12.987	17.275	11.820	13.569
14.90	13.715	12.604	13.939	23.087	12.951	14.481
20.10	11.339	13.912	15.052	20.555	14.233	15.553
25.30	13.395	15.096	16.091	21.925	15.398	16.560
30.20	20.962	16.122	17.013	33.594	16.412	17.456
35.00	14.478	17.061	17.870	33.250	17.342	18.293
40.00	15.994	17.981	18.720	30.249	18.253	19.124

Table 3.21 – Average of the experimental parameters and analytical end stiffness, Test 7

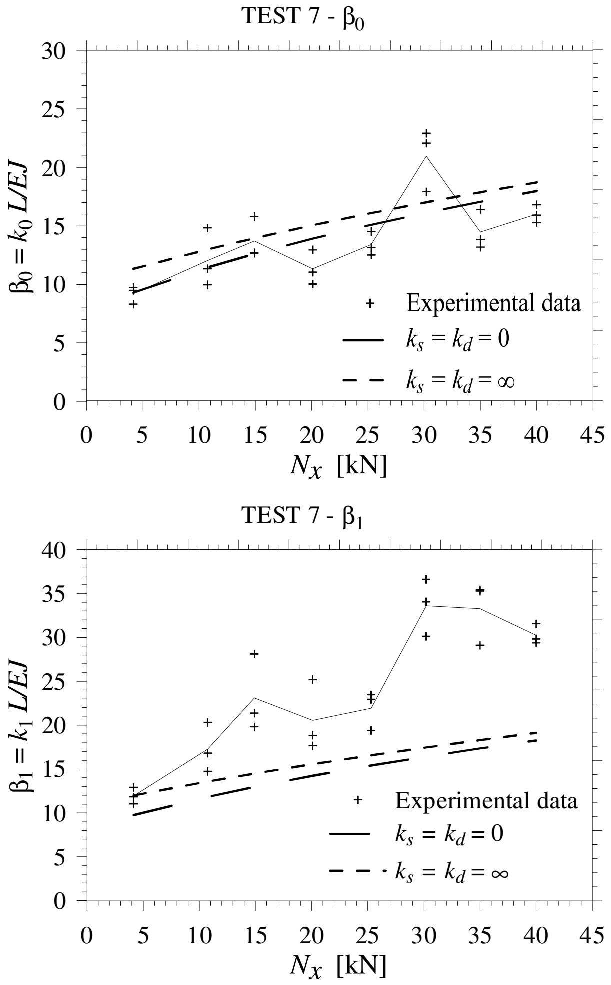

Figures 3.39 – End constraint stiffness of the central span vs. tensile force *N*. Test 7

TEST 8

N_x [kN]	β_0			β_1		
	Test 8.	$k_{s,d} = 0$	$k_{s,d} = \infty$	Test 8	$k_{s,d} = 0$	$k_{s,d} = \infty$
4.15	17.183	9.283	11.328	13.712	9.743	11.995
10.75	15.267	11.443	12.987	19.654	11.820	13.569
14.90	15.701	12.604	13.939	15.951	12.951	14.481
20.10	16.359	13.912	15.052	14.360	14.233	15.553
25.30	14.272	15.096	16.091	18.432	15.398	16.560
30.20	16.680	16.122	17.013	19.258	16.412	17.456
35.00	19.751	17.061	17.870	29.073	17.342	18.293
40.00	15.102	17.981	18.720	17.420	18.253	19.124

Table 3.22 – Average of the experimental parameters and analytical end stiffness, Test 8

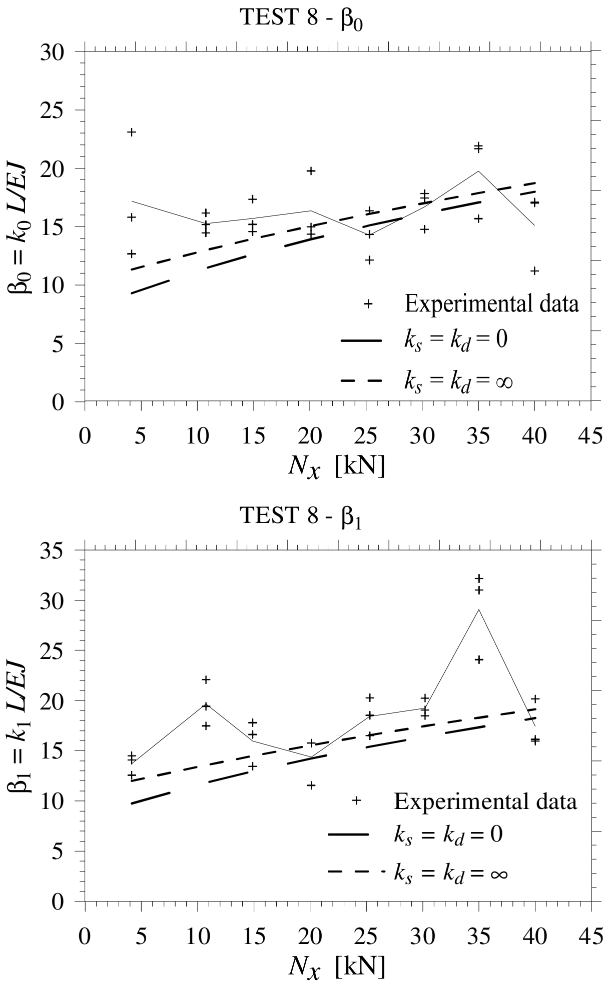

Figures 3.40 – End constraint stiffness of the central span vs. tensile force *N*. Test 8

3.4 Conclusions

A static and dynamic procedure were presented, which allows experimental procedures to evaluate the axial force in structural members which do not experiment translational displacements at the end sections.

The dynamic procedure follows the method outlined by Tullini and Laudiero (2008). Adopting Euler–Bernoulli beam model, if bending stiffness and mass per unit length of a beam with constant cross-section are known, the axial force and the flexural stiffness of the end constraints can be deduced by one vibration frequency and three amplitudes of corresponding modal shape. Indeed, analytical investigation showed that a transcendental equation, irrespective of boundary conditions, between mode shape displacements and axial force can be formulated.

The equipment of the dynamic procedure is constituted by an impact hammer, three piezoelectric accelerometers, a signal conditioner, and a PC for data acquisition. The inertance function evaluated at three instrumented sections allow to reduce the search of the modal parameters to the analysis of a single dof. In fact, it has been shown that peak pick method can be successfully adopted.

Laboratory tests showed excellent agreement between the estimated forces and the assigned values measured by load cells, with errors of about 1%. As for the end stiffness identification, comparisons between the experimental results and their theoretical values, obtained by means of exact dynamic condensation, as shown in Chapter 2, were performed. It was noted that at the beam end in front of the hydraulic jack, the estimation of the elastic parameter is quite reasonable. Vice versa, at the opposite end in front of the load cells, the estimation of the end stiffness is not satisfactory at all. Hence, identification of boundary conditions is clearly ill conditioned. Moreover, it was noted that the identification accuracy also depends on the distance between control points. Indeed, with greater distances between the control points the identification of axial loads and the end stiffness become more accurate.

A lot of in situ application to estimate axial force in tie beams of arches and vaults have already been successfully realized, as shown in Candela et al. (2004) and Bruschi et al. (2004).

As for static tests, a new procedure for the axial load identification of simply supported beam is presented. Adopting Euler-Bernoulli beam model, and knowing bending stiffness and mass per unit length, the axial force can be deduced by three displacements recorded at three instrumented section along the beam length, after the application of a vertical force. Experimental tests showed excellent agreement between the estimated forces and the assigned values measured by load cells, with errors of about 3% if the vertical load is applied in the beam midspan. Otherwise, if the vertical load is applied close to a support, the errors increase up to 9%.

As for the end stiffness identification, despite of the good results in the identification of axial load, scattered and unreliable results have been obtained.

4

Dynamic algorithms for axial load identification of frames on elastic supports

4.1 Introduction

The algorithms presented in Section 3.2 have shown that, if bending stiffness and mass per unit length of a beam with constant cross-section are known, the axial force and the flexural stiffness of the end constraints can be deduced by one vibration frequency and three components of the corresponding mode shape (Tullini and Laudiero, 2008). The method can be applied only to structures without transversal displacements at end sections. For generic structures, such as truss structures or beams whose length is unknown, the assumption of fix supports fails. Moreover, the knowledge of the effective length in exam is essential to correctly estimate the axial load.

The identification method proposed hereafter extends the algorithm presented in Chapter 3 to the more general problem of slender beam with elastic supports. Indeed, the dynamic behaviour of any structure can be represented by some substructure, provided that exact boundary conditions are assigned. In order to describe, the dynamic behaviour of a global structure with a substructure, by means of a finite element formulation, in Chapter 2 it has been shown how the boundary conditions are to be assigned in terms of exact dynamic stiffness matrix. For a typical beam the condensation parameter involves both translational and rotational end dofs and, as derived in Example 3 of Section 2.7, can be represented by means of a full 2x2 matrix. This condensation parameter matrix can be seen as a set of purely translational and rotational springs (diagonal elements), and two mixed springs (out-of-diagonal elements), which simulate coupling between vertical displacement and bending moment or rotation and shear force.

In this chapter it will be shown that axial force can be identified using one vibration frequency and five components of the corresponding mode shape. Moreover, if the modal shape is recorded at the quarter sections of the beam span, an explicit transcendental equation depending on axial force is obtained.

As for the end stiffness parameters, the method does not give a real estimation of the full condensation parameter matrix, but an estimate of diagonal terms only. The identification of the two mixed springs needs the use of two additional dynamic parameters, which have to be evaluated by experimental tests. Nonetheless, an algorithm based on 8 experimental measures could be significantly ill conditioned. Indeed, as shown in this chapter, the use of 5 modal shape records provides a decrease of the accuracy with respect to the axial load identification method of beam on rigid supports.

4.2 Identification of axial force

The beam governing equations have been presented in Section 1.3.1; the contribution of lumped mass-in-span and the end forces are neglected (Figure 4.1). Young's modulus *E*, mass per unit length *m* and cross-section second area moment *J* are assumed to be constant, and known as well.

In order to identify the axial load *N*, one vibration frequency and the corresponding mode shape at five locations coordinates x_0, x_1, x_2, x_3 and x_4 is required. In the following, the mode shape amplitudes at these points are indicate with the notation $v_i = v(x_i)$ for $x = 0,\ldots,4$.

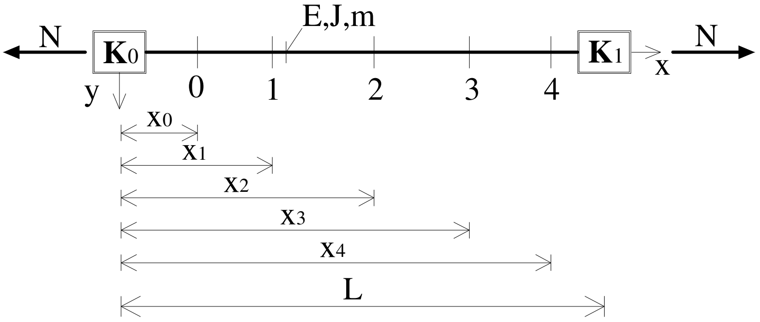

Figure 4.1 - Beam with location of the instrumented sections

With reference to Figure 4.1 and the non dimensional coordinate $z = x/L$, the constants $C_1 - C_4$ of the shape function in Eq. (1.38) can be determined considering the following system, which collects the five equations of the modal shape records:

$$\begin{bmatrix} \cos q_1 z_0 & \sin q_1 z_0 & \cosh q_2 z_0 & \sinh q_2 z_0 \\ \cos q_1 z_1 & \sin q_1 z_1 & \cosh q_2 z_1 & \sinh q_2 z_1 \\ \cos q_1 z_2 & \sin q_1 z_2 & \cosh q_2 z_2 & \sinh q_2 z_2 \\ \cos q_1 z_3 & \sin q_1 z_3 & \cosh q_2 z_3 & \sinh q_2 z_3 \\ \cos q_1 z_4 & \sin q_1 z_4 & \cosh q_2 z_4 & \sinh q_2 z_4 \end{bmatrix} \begin{bmatrix} C_1 \\ C_2 \\ C_3 \\ C_4 \end{bmatrix} = \begin{bmatrix} v_0 \\ v_1 \\ v_2 \\ v_3 \\ v_4 \end{bmatrix} \tag{4.1}$$

Coefficients C_1-C_4 are linear functions of the five (experimental) amplitudes v_0, v_1, v_2, v_3, v_4, and depend on the unknown parameter n and on constant λ through coefficient q_1 and q_2 reported in Eqs. (1.39). In its turn, λ depends on the experimental circular frequency ω. The system (4.1) is overdetermined, but for assigned value of n and considering only the first four equations

$$\begin{bmatrix} \cos q_1 z_0 & \sin q_1 z_0 & \cosh q_2 z_0 & \sinh q_2 z_0 \\ \cos q_1 z_1 & \sin q_1 z_1 & \cosh q_2 z_1 & \sinh q_2 z_1 \\ \cos q_1 z_2 & \sin q_1 z_2 & \cosh q_2 z_2 & \sinh q_2 z_2 \\ \cos q_1 z_3 & \sin q_1 z_3 & \cosh q_2 z_3 & \sinh q_2 z_3 \end{bmatrix} \begin{bmatrix} C_1(n,\lambda) \\ C_2(n,\lambda) \\ C_3(n,\lambda) \\ C_4(n,\lambda) \end{bmatrix} = \begin{bmatrix} v_0 \\ v_1 \\ v_2 \\ v_3 \end{bmatrix} \tag{4.2}$$

it can be seen as a liner system in the unknown C_1-C_4, which has an unique solution. Hence, the sought parameter n is such that the constants C_1-C_4, derived from the solution of system (4.2), satisfy the last equation of the system (4.1), neglected by the system (4.2):

$$C_1(n,\lambda)\cos q_1 z_4 + C_2(n,\lambda)\sin q_1 z_4 + C_3(n,\lambda)\cosh q_2 z_4 + C_4(n,\lambda)\sinh q_2 z_4 = v_4 \tag{4.3}$$

Once n and the constants C_1-C_4 are known, the modal shape function Eq. (1.38) is completely defined.,

The above formulation can be simplified if control points are assumed at sections having nondimensional coordinates $x_0 = 0$, $x_1 = 1/4$, $x_2 = 1/2$, $x_3 = 3/4$ and $x_4 = 1.$, i.e. at the end sections of the beam and the other three at the quarters of the span. In this case, if the mid-section does not coincide with a node of the assumed mode shape, i.e.. if $v_2 = 0$, Eqs. (4.3) yields

$$\frac{v_1 + v_3}{v_2} = \frac{\dfrac{v_0 + v_4}{2v_2} + 1 + 2\cos(q_1/4)\cosh(q_2/4)}{\cos(q_1/4) + \cosh(q_2/4)} \tag{4.4}$$

Equation (4.4) is similar to Eq. (3.12), deduced for the problem of a beam on rigid supports. Indeed, by setting $v_0 = v_4 = 0$ in Eq. (4.4), Eq. (3.12) is recovered.

The most important application of Eq. (4.4) or Eq. (4.3) is the axial load identification of a beam belonging to a complex structure, where its end sections can rotate or translate and its structural length is uncertain (Figure 4.2). Indeed, the connecting devices of the beam under investigation with the other structural members have a finite length that made the vibration length of the substructure indeterminate. Since the identification algorithms depends crucially on this parameter, it is possible to overcome the problem by assuming as substructure a portion of the beam. If the progressive numbers 0,..,4 indicate the location of the instrumented sections along the beam, the length of the beam considered is simply the distance between the first position (No. 0) and the last one (No. 4).

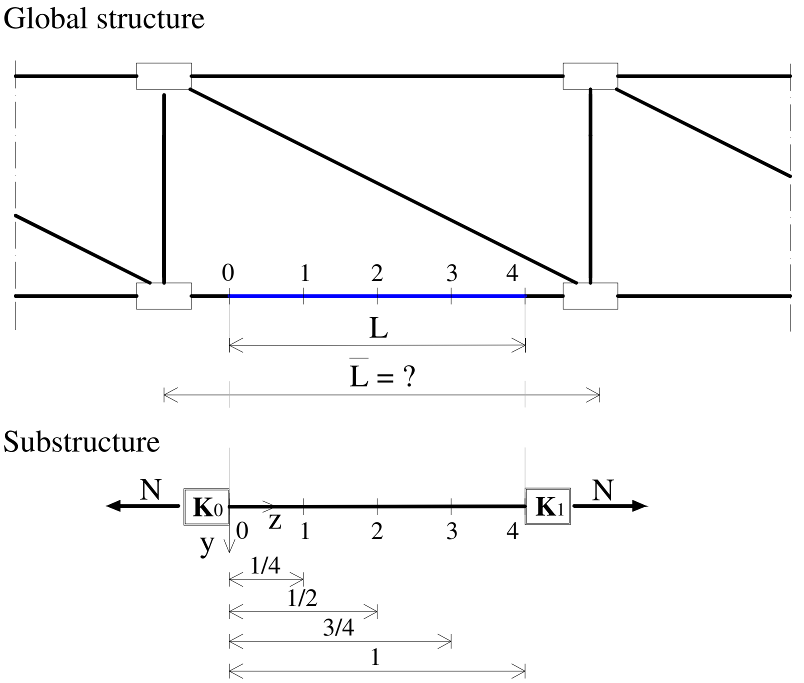

Figure 4.2 – Application of the procedure to a member of a truss structure

4.3 Governing equations with the reduced boundary conditions

In this section, the reference model is constituted by a prismatic beam of length L, constrained by four end elastic-springs with k_0 and k_1 flexural stiffness, h_0 and h_1 translational stiffness, and subjected to an axial resultant N (positive sign is assigned to tensile forces), Figure 4.3.

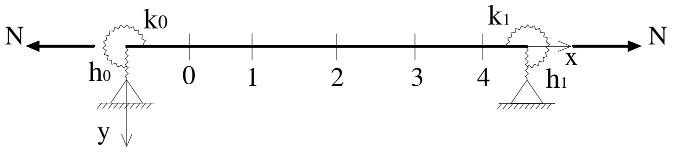

Figure 4.3 – Beam with flexural and translation constraints

The model is a particular case of the more general problem presented in Section 1.3.1: the contribution of lumped mass in-span and of end forces are not considered, and the condensation parameter matrices reduce to diagonal:

$$\mathbf{K}_0 = \begin{bmatrix} k_v^0 & k_{v\varphi}^0 \\ k_{v\varphi}^0 & k_\varphi^0 \end{bmatrix} = \begin{bmatrix} h_0 & 0 \\ 0 & k_0 \end{bmatrix} \qquad \mathbf{K}_1 = \begin{bmatrix} k_v^1 & k_{v\varphi}^1 \\ k_{v\varphi}^1 & k_\varphi^1 \end{bmatrix} = \begin{bmatrix} h_1 & 0 \\ 0 & k_1 \end{bmatrix} \tag{4.5}$$

Making use of the non dimensional coordinate $z = x/L$ and neglecting both rotary inertia and shear deformation, circular frequencies ω and mode shape $v(z)$ are ruled by the eigenvalue problem just presented in Eq. (1.33) with the boundary conditions (1.43) specified for this model ($k_{v\varphi}^{0,1} = \varsigma_{0,1} = 0$) (Maurizi and Bellés, 1991)

$$v''''(z) - nv''(z) - \lambda^4 v(z) = 0 \tag{4.6}$$

$$\begin{cases} v'''(0) + \eta_0 v(0) + nv'(0) = 0 \\ v''(0) - \beta_0 v'(0) = 0 \\ v'''(1) - \eta_1 v(1) + nv'(1) = 0 \\ v''(1) + \beta_1 v'(1) = 0 \end{cases} \tag{4.7}$$

where prime mean derivation with respect to z and

$$\eta_{0,1} = \frac{k_v^{0,1} L^3}{EJ} \qquad \beta_{0,1} = \frac{k_\varphi^{0,1} L}{EJ} \qquad n = \frac{NL^2}{EJ} \qquad \lambda^4 = \frac{\omega^2 m L^4}{EJ} \tag{4.8}$$

Solution of Eqs. (4.6) and (4.7) are given by Eq. (1.38).

Application of boundary conditions leads to a system of homogeneous algebraic equations in the in unknowns C_1-C_4. Since the solution must be non-trivial, the vanishing of the determinant of the coefficient matrix gives the following frequency equation (Maurizi and Bellés, 1991)

$$
\begin{aligned}
&\alpha_0\tau_0\alpha_1\tau_1\Big\{(\cos R\cosh M-1)\Big[2M^5R^5+4U\left(M^3R^5-M^5R^3\right)-8U^2M^3R^3\Big]\\
&+\sin R\sinh M\Big[\left(M^4R^6-M^6R^4\right)-8UM^4R^4+4U^2\left(M^4R^2-M^2R^4\right)\Big]\Big\}\\
&+(\alpha_0\tau_0\tau_1+\alpha_1\tau_0\tau_1)\Big\{\sin R\cosh M\Big[\left(M^5R^4+M^3R^6\right)-2U\left(M^5R^2+M^3R^4\right)\Big]\\
&+\cos R\sinh M\Big[\left(M^4R^5+M^6R^3\right)+2U\left(M^2R^5+M^4R^3\right)\Big]\Big\}+\tau_0\,\tau_1\sin R\sinh M\\
&\times\left(M^6q^2+M^2R^6+2M^4R^4\right)+(\alpha_0\,\alpha_1\tau_0+\alpha_0\,\alpha_1\tau_1)\Big\{\sin R\cosh M\Big[\left(M^5R^2+M^3R^4\right)\\
&+2U\left(M^3R^2+MR^4\right)\Big]-\cos R\sinh M\Big[\left(M^2R^5+M^4R^3\right)-2U\left(M^2R^3+M^4R\right)\Big]\Big\}\\
&-(\alpha_0\,\tau_1+\alpha_1\,\tau_0)\cos R\cosh M\Big[\left(M^5R+MR^5\right)+2M^3R^3\Big]-(\alpha_0\tau_0+\alpha_1\tau_1)\Big[\left(MR^5+M^5R\right)\\
&+2M^3R^3\cos R\cosh M-2U\left(MR^3-M^3R\right)(1-\cos R\cosh M)\\
&-\sin R\sinh M\left(M^4R^2-M^2R^4+4UM^2R^2\right)\Big]-(\tau_0+\tau_1)\Big[\left(M^3R^2+MR^4\right)\sin R\cosh M\\
&+\left(M^2R^3+M^4R\right)\cos R\sinh M\Big]-\alpha_0\alpha_1\sin R\sinh M\left(M^4+R^4+2M^2R^2\right)\\
&-(\alpha_0+\alpha_1)\Big[\left(M^3+MR^2\right)\sin R\cosh M-\left(R^3+M^2R\right)\cos R\sinh M\Big]\\
&+\Big[2MR(\cos R\cosh M-1)-\sin R\sinh M\left(M^2-R^2\right)\Big]=0
\end{aligned}
\tag{4.9}
$$

with the following notation:

$$
R^2=q_1^2\qquad M^2=q_2^2\qquad U=-\frac{n}{2}\qquad \Omega=\lambda^2\qquad \alpha_{0,1}=\frac{1}{\beta_{0,1}}\qquad \tau_{0,1}=\frac{1}{\eta_{0,1}}
\tag{4.10}
$$

For each particular set of value of the parameters n, β_0, η_0, β_1 and η_1 the equation gives infinite number of roots.

Once n and the constants $C_1 - C_4$ are known through Eqs. (4.4) and (4.2), the mode shape (1.38) is completely defined, and the end stiffness parameters are immediately derived from Eq. (4.7)

$$\begin{cases} \eta_0 = \dfrac{C_2\left(q_1^3 - nq_1\right) - C_4 q_2\left(n + q_2^2\right)}{C_1 + C_3} \\ \beta_0 = \dfrac{-C_1 q_1^2 + C_3 q_2^2}{C_2 q_1 + C_4 q_2} \\ \eta_1 = \dfrac{q_1\left(n - q_1^2\right)\left(C_2 \cos q_1 - C_1 \sin q_1\right) + q_2\left(n + q_2^2\right)\left(C_3 \sinh q_2 + C_4 \cosh q_2\right)}{C_1 \cos q_1 + C_2 \sin q_1 + C_3 \cosh q_2 + C_4 \sinh q_2} \\ \beta_1 = -\dfrac{q_1^2\left(C_1 \cos q_1 + C_2 \sin q_1\right) - q_2^2\left(C_3 \cosh q_2 + C_4 \sinh q_2\right)}{-C_1 q_1 \sin q_1 + C_2 q_1 \cos q_1 + C_3 q_2 \sinh q_2 + C_4 q_2 \cosh q_2} \end{cases} \tag{4.11}$$

The above formulation can be simplified if control points are assumed at sections having nondimensional coordinates $x_0 = 0$, $x_1 = 1/4$, $x_2 = 1/2$, $x_3 = 3/4$ and $x_4 = 1.$, i.e. at the end sections of the beam and the other three at the quarters of the span. In this case, Eqs. (4.11) yield

$$\begin{aligned} \beta_0 &= \frac{\left(q_1^2 + q_2^2\right)\left(a\dfrac{v_1}{v_2} - f\dfrac{v_4}{v_2} - b\right) - \left(q_1^2 e + q_2^2 g\right)\dfrac{v_0}{v_2}}{c\dfrac{v_1}{v_2} + h\dfrac{v_4}{v_2} - i\dfrac{v_0}{v_2} - d} \\ \beta_1 &= \frac{\left(q_1^2 + q_2^2\right)\left(a\dfrac{v_3}{v_2} - f\dfrac{v_0}{v_2} - b\right) - \left(q_1^2 e + q_2^2 g\right)\dfrac{v_4}{v_2}}{c\dfrac{v_3}{v_2} + h\dfrac{v_0}{v_2} - i\dfrac{v_4}{v_2} - d} \\ \eta_0 &= \frac{c'\dfrac{v_1}{v_2} + h'\dfrac{v_4}{v_2} - i'\dfrac{v_0}{v_2} - d'}{\dfrac{v_0}{v_2}\left(e + g\right)} \\ \eta_1 &= \frac{c'\dfrac{v_3}{v_2} + h'\dfrac{v_0}{v_2} - i'\dfrac{v_4}{v_2} - d'}{\dfrac{v_4}{v_2}\left(e + g\right)} \end{aligned} \tag{4.12}$$

where constants *a*, *b*, *c*, *d* are the same derived in Eqs. (3.14), and *e*, *f*, *g*, *h*, *i*, *c'*, *h'*, *d'*, *i'*, are given by the following relations:

$$\begin{aligned}
e &= \sin q_1 \sinh\frac{q_2}{4} + \sin\frac{q_1}{4}\sinh\frac{q_2}{2} - \sin\frac{q_1}{2}\sinh\frac{3q_2}{4} \\
f &= \sin\frac{q_1}{4}\sinh\frac{q_2}{2} - \sin\frac{q_1}{2}\sinh\frac{q_2}{4} \\
g &= \sin\frac{q_1}{2}\sinh\frac{q_2}{4} + \sin\frac{q_1}{4}\sinh q_2 - \sin\frac{3q_1}{2}\sinh\frac{q_2}{2} \\
h &= h_1 + h_2 \\
h_1 &= q_1\left(\sinh\frac{q_2}{4} + \cos\frac{q_1}{2}\sinh\frac{q_2}{4} - \cos\frac{q_1}{4}\sinh\frac{q_2}{2}\right) \\
h_2 &= q_2\left(\sin\frac{q_1}{4} - \sin\frac{q_1}{2}\cosh\frac{q_2}{4} + \sin\frac{q_1}{4}\cosh\frac{q_2}{2}\right) \\
i &= i_1 + i_2 \\
i_i &= q_1\left(\cos q_1 \sinh\frac{q_2}{4} + \cos\frac{q_1}{4}\sinh\frac{q_2}{2} - \cos\frac{q_1}{2}\sinh\frac{3q_2}{4}\right) \\
i_2 &= q_2\left(\sin\frac{q_1}{4}\cosh q_2 + \sin\frac{q_1}{2}\cosh\frac{q_2}{4} - \sin\frac{3q_1}{4}\cosh\frac{q_2}{2}\right)
\end{aligned} \tag{4.13}$$

$$\begin{aligned}
c' &= q_2^2 c_1 - q_1^2 c_2 \\
d &= q_2^2 d_1 - q_1^2 d_2 \\
h' &= q_2^2 h_1 - q_1^2 h_2 \\
i' &= q_2^2 i_1 - q_1^2 i_2
\end{aligned} \tag{4.14}$$

It is worth noting that amplitudes at the end sections, i.e. $v_0 = v_4 = 0$, Eqs. (4.12)c and (4.12)d yield to $\eta_0 = \eta_1 = \infty$ and Eqs. (3.13) are obtained.

4.4 Laboratory tests

In order to apply the analytical procedure derived in the previous section and to ascertain its accuracy, experimental tensile and tests have been performed, Figure 4.4. For tensile test, the same configurations of the laboratory tests of Section 3.2.4 were adopted, as well as the instrumentation used. In seek of convenience, few details are here recalled. The test specimen was a steel rod with 20 mm diameter, for which Young's modulus E = 206 GPa and density ρ = 7850 kg/m^3 were experimentally evaluated. The end supports were realized by means of the connection with hydraulic jack (right side) and load cells (left side), see Figures 3.5 - 3.8.

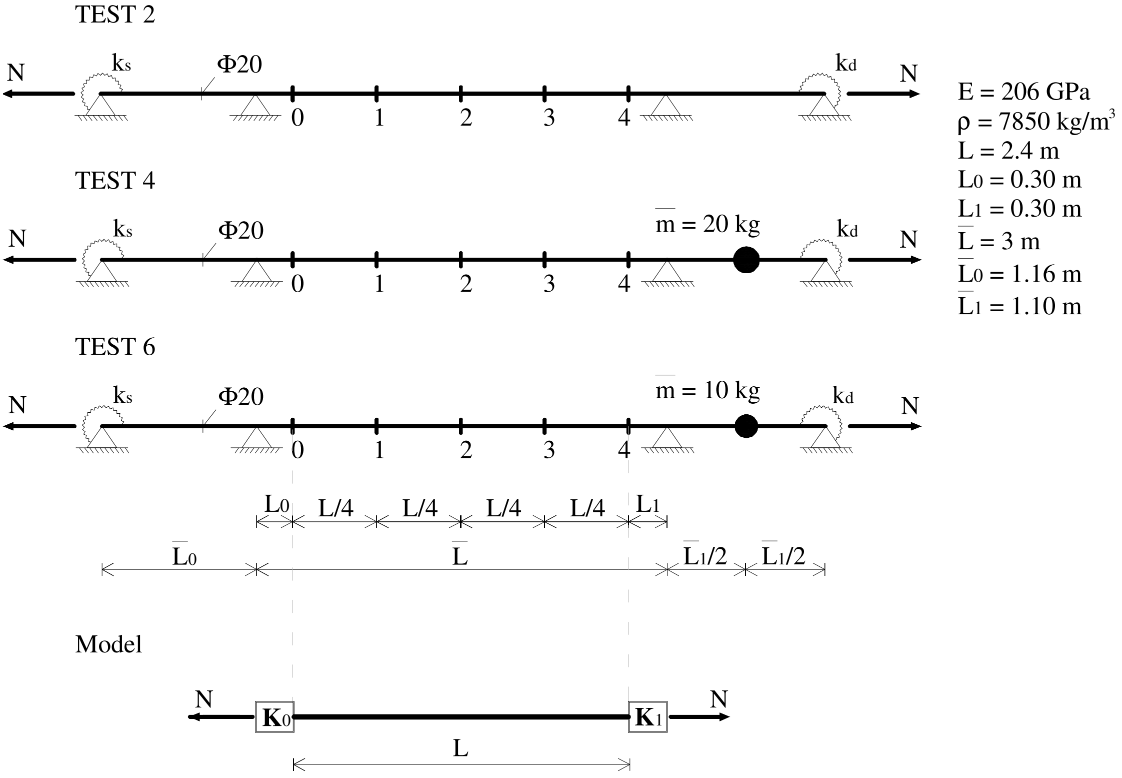

Figure 4.4 – Application of the procedure to a member continuous beam

Five piezoelectric accelerometers PCB/353B18, having sensitivity of 10 mV/g and weight of 1.8 g, were fastened in the central span, at equal distances, by means of metallic wrappers Figure 3.8a). In particular, the accelerometers were located at the quarter sections of a portion of the central beam, which was obtained neglecting the end pieces of length L_0 and L_1 (both 0.30 m). Hence, the instrumented sections define the model length of the beam L as the distance between the first accelerometer (Position No. 0) and the last one (Position No. 4). Therefore the beam length adopted in the analysis was 0.60 m less than that used in tests of Section 3, where $\overline{L}$ = 3 m.

Dynamic tests were performed, hitting the instrumented sections with an impact hammer PCB/086C04, able to measure a pulse up to 4.4 kN with sensitivity of 1.2 mV/N. All the instruments were connected to a signal conditioner and, finally, to a PC data acquisition system set with block size (*BS*) equal to 2^{16} and 5000 Hz as sampling rate (*SR*). For each value of axial load imposed by the actuator, the tests were performed hitting, three times, each of the five instrumented sections of the central span.

4.5 Results

4.5.1 Experimental data

Experimental modal analysis technique used in this section are those described in Section 3.2.5.

Figure 4.5 shows an example of experimental FRFs related to configuration No. 4 ($\overline{m}$ = 20 kg) for about 20 kN of axial load. It is worth noting that, analogously to tests described in Section 3.2.6.1, the first pick is detectable with trouble. Indeed, the presence of the lumped mass in the middle of the right span produces pick amplitudes too small for a good fit of the first modal frequency. Moreover, with increasing axial force, the phenomenon of switch between the first flexural vibration mode of the beam and the first translational vibration mode of the lumped mass, observed in Section 3.2.6.1, still occurs. All the observation made in Section 3.2.6.1 are still valid. Therefore, in order to overcome errors in the axial load identification using the first mode shape, the second vibration mode has been also used for test 4.

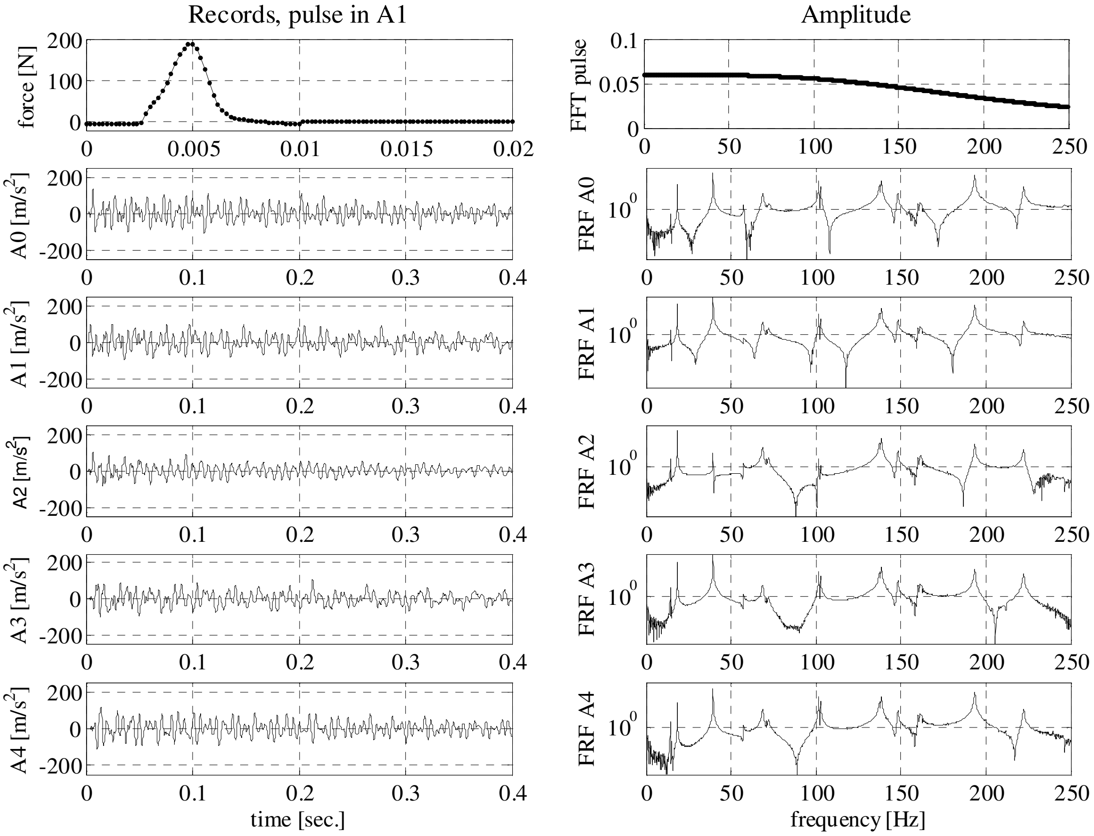

Figure 4.5 – Time history and frequency spectrum for the impact hammer and five instrumented sections (from test 4)

Notwithstanding the conclusion of Section 3.2.6.4, where the comparison between the two identification methods PPM and PRMI showed that PPM should be adopted for all tests realized, both methods have been employed again, in seek of a better accuracy: PPM for test 2 (configuration without lumped mass) and PRMI for tests 4 and 6.

Tables 4.1-4.4 show the average modal parameters for each axial load and for the three configurations tested.

Table 4.3 shows that, as expected, the second vibration mode of configuration with a 20 kg lumped mass (test No. 4) corresponds to the flexural vibration of the central span. Indeed the modal shape amplitude recorded at the middle section (v_2) is the greater for each load step, whereas for the first frequency the greater modal shape amplitude may be in section v_3 (Table 4.2).

TEST 2

N_a [kN]	f [Hz]	v_0	v_1	v_2	v_3	v_4	λ	$(v_1+v_3)/2v_2$	$(v_0+v_4)/2v_2$
4.502	10.834	0.2138	0.7371	1.0000	0.7684	0.2268	3.913	0.7527	0.2203
10.945	14.049	0.2216	0.7496	1.0000	0.7730	0.2310	4.455	0.7613	0.2263
15.108	15.747	0.2220	0.7541	1.0000	0.7737	0.2351	4.717	0.7639	0.2285
20.077	17.563	0.2268	0.7576	1.0000	0.7770	0.2384	4.982	0.7673	0.2326
24.749	19.109	0.2300	0.7632	1.0000	0.7790	0.2412	5.196	0.7711	0.2356
30.385	20.833	0.2348	0.7678	1.0000	0.7803	0.2420	5.426	0.7741	0.2384
34.871	22.069	0.2370	0.7693	1.0000	0.7821	0.2446	5.584	0.7757	0.2408
40.181	23.453	0.2397	0.7714	1.0000	0.7840	0.2471	5.757	0.7777	0.2434
45.696	24.811	0.2425	0.7733	1.0000	0.7851	0.2489	5.921	0.7792	0.2457
49.771	25.787	0.2453	0.7758	1.0000	0.7856	0.2493	6.036	0.7807	0.2473

Table 4.1 – Average of the experimental parameters at the first modal frequency, Test 2

TEST 4

N_a [kN]	f [Hz]	v_0	v_1	v_2	v_3	v_4	λ	$(v_1+v_3)/2v_2$	$(v_0+v_4)/2v_2$
4.879	10.224	0.1943	0.6967	1.0000	0.8561	0.3287	3.801	0.7764	0.2615
11.121	12.250	0.1814	0.6896	1.0000	0.9276	0.4268	4.160	0.8086	0.3041
16.192	13.331	0.1882	0.6679	1.0000	0.9775	0.5179	4.340	0.8227	0.3530
21.137	14.183	0.1798	0.6479	0.9784	1.0000	0.5846	4.477	0.8422	0.3907
25.632	15.209	0.1781	0.6624	0.9617	1.0000	0.6128	4.636	0.8641	0.4116
30.605	15.812	0.1844	0.6411	0.9594	1.0000	0.6447	4.727	0.8553	0.4321
36.189	16.549	0.1771	0.5814	0.9320	1.0000	0.6818	4.836	0.8485	0.4608
40.974	17.158	0.1799	0.5444	0.9353	1.0000	0.7109	4.924	0.8256	0.4763

Table 4.2 – Average of the experimental parameters at the first modal frequency, Test 4

TEST 4 – Second normal mode

N_a [kN]	f [Hz]	v_0	v_1	v_2	v_3	v_4	λ	(v_1+v_3) $/2v_2$	(v_0+v_4) $/2v_2$
4.879	12.560	0.2437	0.8129	1.0000	0.6210	0.0667	4.213	0.7170	0.1552
11.121	14.796	0.2343	0.7679	1.0000	0.7200	0.1658	4.572	0.7439	0.2001
16.192	16.757	0.2327	0.7763	1.0000	0.7299	0.1780	4.866	0.7531	0.2053
21.137	18.370	0.2348	0.7759	1.0000	0.7449	0.1954	5.095	0.7604	0.2151
25.632	19.741	0.2369	0.7755	1.0000	0.7538	0.2063	5.282	0.7646	0.2216
30.678	21.172	0.2390	0.7771	1.0000	0.7605	0.2148	5.470	0.7688	0.2269
36.204	22.670	0.2414	0.7782	1.0000	0.7659	0.2222	5.660	0.7720	0.2318
40.974	23.890	0.2438	0.7780	1.0000	0.7690	0.2262	5.810	0.7735	0.2350

Table 4.3 – Average of the experimental parameters at the second modal frequency, Test 4

TEST 6

N_a [kN]	f [Hz]	v_0	v_1	v_2	v_3	v_4	λ	(v_1+v_3) $/2v_2$	(v_0+v_4) $/2v_2$
4.229	10.545	0.2097	0.7265	1.0000	0.7941	0.2518	3.860	0.7603	0.2308
9.972	13.337	0.2157	0.7340	1.0000	0.8001	0.2629	4.341	0.7671	0.2393
14.710	15.195	0.2188	0.7394	1.0000	0.8095	0.2775	4.634	0.7745	0.2481
19.876	17.096	0.2227	0.7461	1.0000	0.8082	0.2791	4.915	0.7772	0.2509
25.094	18.675	0.2254	0.7472	1.0000	0.8170	0.2931	5.137	0.7821	0.2592
30.057	19.987	0.2278	0.7490	1.0000	0.8245	0.3064	5.314	0.7867	0.2671
34.753	21.178	0.2288	0.7482	1.0000	0.8340	0.3227	5.470	0.7911	0.2758
40.071	22.361	0.2305	0.7465	1.0000	0.8437	0.3402	5.621	0.7951	0.2853

Table 4.4 – Average of the experimental parameters at the first modal frequency, Test 6

The experimental terns [λ, $(v_1+v_3)/2v_2$, $(v_0+v_4)/2v_2$] stay in a 3D region between the limit curve for n tending to infinity and the curve corresponding to $n = -4\pi^2$, Eulerian critical load for a double clamped beam. The surface and the contour plot of Eq. (4.4) has been plotted for $n = -4\pi^2$ in Figure 4.6 and 4.7. Figure 4.8 shows the whole set of experimental couple [λ, $(v_1+v_3)/2v_2$], Eq. (4.4) has been represented for different values of $(v_0+v_4)/2v_2 = 0.20, 0.25, 0.35$.

As expected, from the scatter of the experimental points it can be noted that the identification of the modal parameters is very accurate, except for test No. 4, like test No. 3 of Section 3.2.6.1. Since the second mode shape is well identified for each axial load (Table 4.3), the experimental points (cross-symbol) are much more regular and the scatter vanishes.

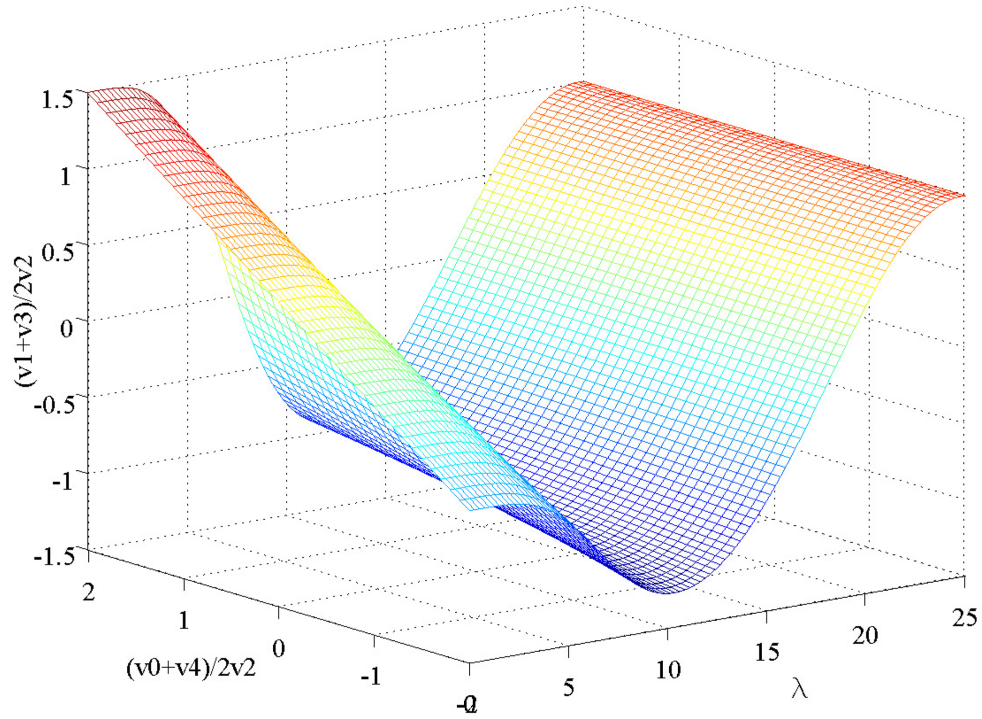

Figure 4.6 – Surface of Eq. (4.4), for $n = -4\pi^2$

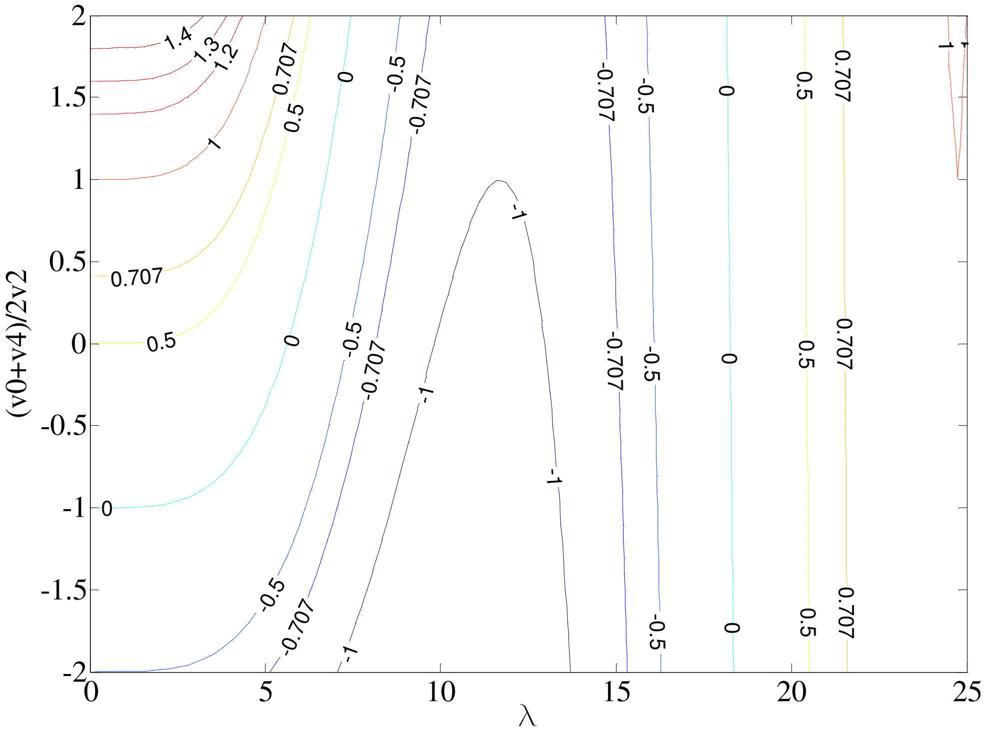

Figure 4.7 – Contour of Eq. (4.4), for $n = -4\pi^2$

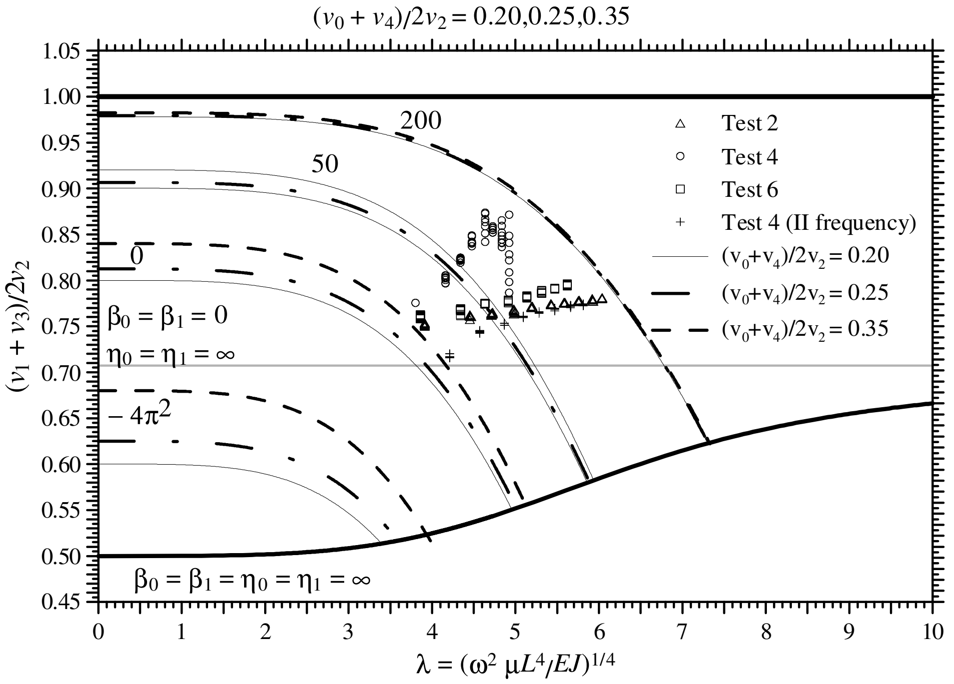

Figure 4.8 – Location of the experimental terns [λ, (v0+v4)/2v2, (v1+v3)/2v2]

4.5.2 Axial load identification

Estimated axial load N_a may be found by solving Eq. (3.12) for each couple of experimental data [λ, $(v_1+v_3)/2v_2$, $(v_0+v_4)/2v_2$] collected in Tables 4.1-4.4.

Figures 4.9-4.12 compare measured N_X and estimated N_a axial force for each configuration tested. Results for test 4 reported in Figure 4.10 derives from the use of the second flexural mode of the frame.

The graphs show very good agreement between measured and estimated mean parameters except for the test 4, where the first mode shape has been used. The scatter of the experimental points for axial load greater than about 20 kN, observed in Figure 4.8, is also evident in the axial load identification at the same load level (Figure 4.10). Nevertheless, using the second mode shape, the average percent errors Δ is about 2.5%.

It is worth noting that the relative errors of the identification is greater than that observed for the algorithm for axial load identification of beam on rigid supports, Section 3.2.6.2 ($\Delta \approx 1\%$). The difference in the identification accuracy of the two algorithms is due to the different number of control points, which have a crucial importance in the identification procedure. The use of multiple experimental measurements inevitably leads to more inaccuracies in the identification process. Nevertheless, the experimental tests show that the evaluation of the axial load with 5 control points is very good and the procedure can be safely adopted.

N_x [kN]	N_a [kN]	Δ [%]
4.508	4.162	-7.69
10.945	10.576	-3.37
15.117	14.576	-3.58
20.072	19.452	-3.09
24.749	24.114	-2.57
30.385	29.764	-2.04
34.871	34.080	-2.27
40.181	39.290	-2.22
45.696	44.651	-2.29
49.771	49.162	-1.85

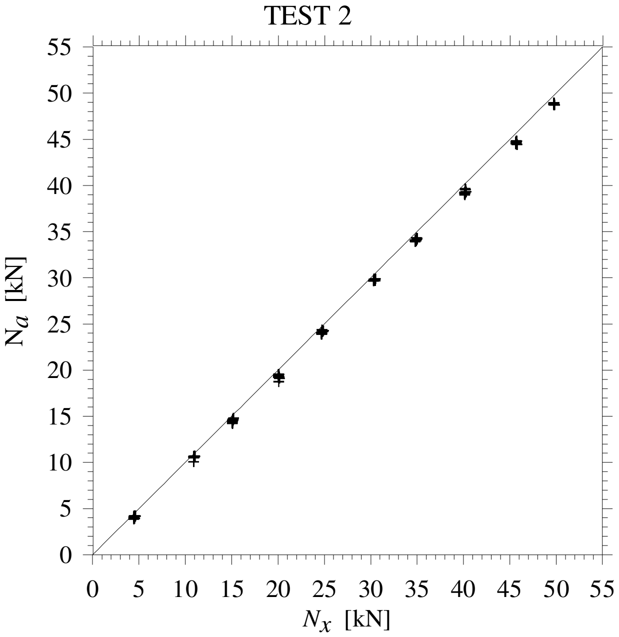

Figure 4.9 – Comparison between measured (N_x) and estimated (N_a) forces, Test 2

N_x [kN]	N_a [kN]	Δ [%]
4.879	4.723	-3.19
11.121	10.521	-5.34
16.192	15.410	-4.83
21.137	20.861	-1.30
25.632	31.654	23.39
30.605	28.799	-5.90
36.189	29.223	-19.25
40.974	25.964	-36.63

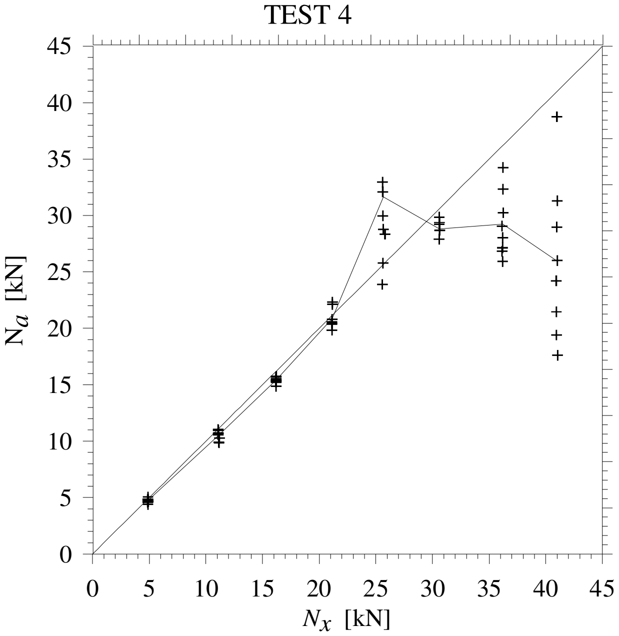

Figure 4.10 – Comparison between measured (N_x) and estimated (N_a) forces, Test 4

N_x [kN]	N_a [kN]	Δ [%]
4.970	4.879	1.86
10.811	11.121	-2.79
15.762	16.192	-2.65
20.637	21.137	-2.37
24.985	25.632	-2.52
29.940	30.605	-2.17
35.406	36.189	-2.16
39.940	40.974	-2.52

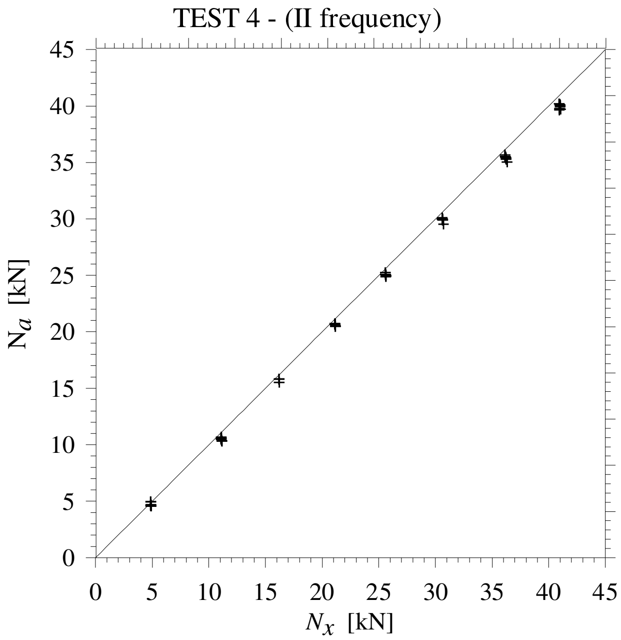

Figure 4.11 – Comparison between measured (N_x) and estimated (N_a) forces using the second mode shape, Test 4

N_x [kN]	N_a [kN]	Δ [%]
4.199	4.229	-0.72
9.720	9.966	-2.46
14.368	14.711	-2.33
19.397	19.876	-2.41
24.477	25.082	-2.41
29.266	29.883	-2.06
34.045	34.753	-2.04
39.129	40.071	-2.35

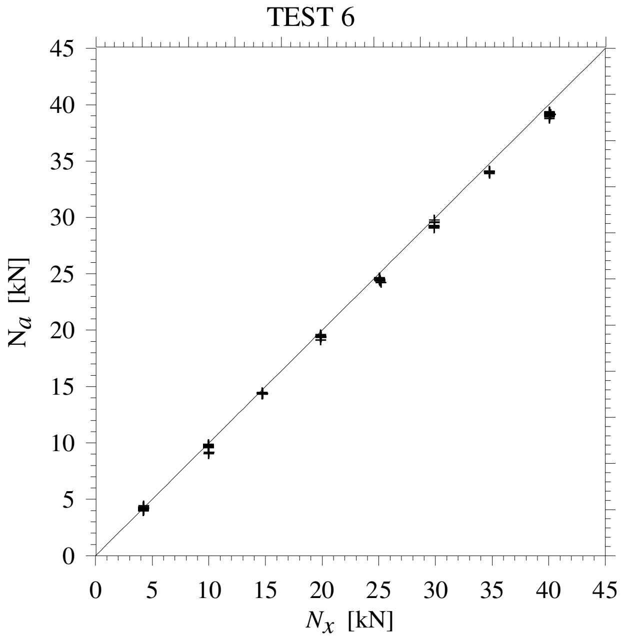

Figure 4.12 – Comparison between measured (N_x) and estimated (N_a) forces, Test 6

4.5.3 End stiffness identification

As for the end stiffness parameters, the method does not give a real estimation of the full condensation parameter matrix, but an estimate of diagonal terms only. In order to make a comparison between the stiffness parameter experimentally evaluated and the exact condensation parameter matrices, finite element analysis of the global structure are needed. With reference to Figure 4.13, for the limit situation of end sections simply supported ($k_s = k_d = 0$), a model with 5 finite element and 8 dofs is considered. The limit situation of clamped end sections ($k_s = k_d = \infty$) is obtained by placing $\theta_1 = \theta_6 = 0$.

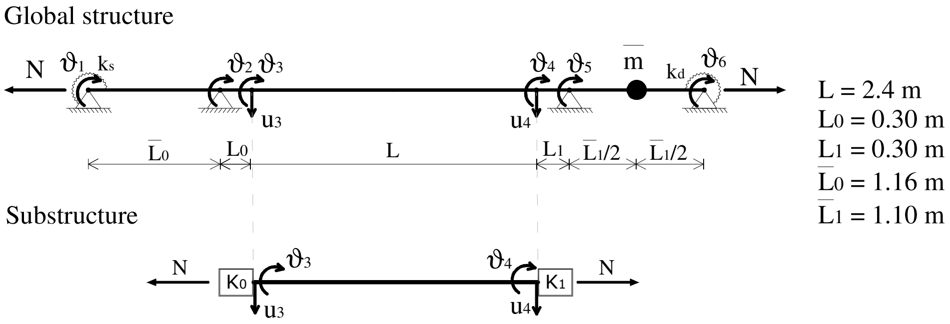

Figure 4.13 – Finite element model for the evaluation of the condensation parameter matrices ($\mathbf{K}_0$,$\mathbf{K}_1$) and visualization of the master dof in the substructure model

For each load step of test 2, the vanishing of the determinant of the dynamic stiffness matrix $\mathbf{D}(\omega)$ gives the first vibration frequency of the global structure:

$$\mathbf{D}(\omega) = \left[\begin{array}{c|c} \mathbf{D}_{\text{mm}} & \mathbf{D}_{\text{ms}} \\ \hline \mathbf{D}_{\text{sm}} & \mathbf{D}_{\text{ss}} \end{array}\right] \tag{4.15}$$

where $\mathbf{m} = [u_3, \theta_3, u_4, \theta_4,]$ states for the dofs of substructure (master dofs) and $\mathbf{s} = [\theta_1, \theta_2, \theta_5, \theta_6]$, slave dofs. As introduced in Example 3 in Section 2.7, the exact condensation parameter matrices $\mathbf{K}_0^{ex}$ and $\mathbf{K}_1^{ex}$, which simulate the stiffness and mass of the part of structure neglected by the substructure, are given by

$$\mathbf{D}_{\text{sub}}(\omega) = \mathbf{D}^*_{\text{mm}}(\omega) = \mathbf{D}_{\text{mm}} - \mathbf{D}_{\text{ms}}\mathbf{D}_{\text{ss}}^{-1}\mathbf{D}_{\text{sm}} \tag{4.16}$$

$$\mathbf{D}_{\text{sub}} - \mathbf{D}_0 = \left[\begin{array}{c|c} \mathbf{K}_0^{ex} & \mathbf{0} \\ \hline \mathbf{0} & \mathbf{K}_1^{ex} \end{array}\right] = \left[\begin{array}{cc|cc} \mathbf{K}_0^{ex}(1,1) & \mathbf{K}_0^{ex}(1,2) & 0 & 0 \\ \mathbf{K}_0^{ex}(2,1) & \mathbf{K}_0^{ex}(2,2) & 0 & 0 \\ \hline 0 & 0 & \mathbf{K}_1^{ex}(1,1) & \mathbf{K}_1^{ex}(1,2) \\ 0 & 0 & \mathbf{K}_1^{ex}(2,1) & \mathbf{K}_1^{ex}(2,2) \end{array}\right] \tag{4.17}$$

where $\mathbf{D}_{\text{sub}}$ is the dynamic stiffness matrix of the substructure obtained by condensing into the master dofs the dynamic stiffness matrix of the global structure, and $\mathbf{D}_0$ is the dynamic stiffness matrix of the simple beam. Making use of positions (1.45)a-b-c, the nondimensional elements of $\mathbf{K}_0^{ex}$, $\mathbf{K}_1^{ex}$ has been considered:

$$\mathbf{K}_0^{ex} = \begin{bmatrix} \eta_0^{ex} & \varsigma_0^{ex} \\ \varsigma_0^{ex} & \beta_0^{ex} \end{bmatrix} \qquad \mathbf{K}_1^{ex} = \begin{bmatrix} \eta_1^{ex} & \varsigma_1^{ex} \\ \varsigma_1^{ex} & \beta_1^{ex} \end{bmatrix} \tag{4.18}$$

Eqs. (4.12) give diagonal condensation parameters, which are obtained by ignoring off-diagonal terms, and the corresponding condensation matrices reduce to:

$$\mathbf{K}_0 = \begin{bmatrix} \eta_0 & 0 \\ 0 & \beta_0 \end{bmatrix} \qquad \mathbf{K}_1 = \begin{bmatrix} \eta_1 & 0 \\ 0 & \beta_1 \end{bmatrix} \tag{4.19}$$

An average of experimental evaluations of parameters and the exact condensation matrices for each limit situation and for each load step is presented in Tables 4.5 and 4.6.

It is worth noting that, as expected, the experimental results do not match the exact parameters at all. For the other tests, similar results are obtained. Hence, the diagonal condensation parameters evaluated by means of the present method do not represent a good estimate of the exact parameters. Consequently, they can not be used for any analysis of the end stiffness of the substructure.

N_x	$\mathbf{K}_0$	$\mathbf{K}_0^{ex}$	$\mathbf{K}_0^{ex}$
[kN]		$k_{s,d} = 0$	$k_{s,d} = \infty$
4.502	$\begin{bmatrix} 391.15 & 0 \\ 0 & 3.03 \end{bmatrix}$	$\begin{bmatrix} 2518.57 & -229.70 \\ -229.70 & 25.83 \end{bmatrix}$	$\begin{bmatrix} 2684.08 & -236.55 \\ -236.55 & 26.11 \end{bmatrix}$
10.945	$\begin{bmatrix} 636.95 & 0 \\ 0 & 2.77 \end{bmatrix}$	$\begin{bmatrix} 2859.49 & -238.92 \\ -238.92 & 26.57 \end{bmatrix}$	$\begin{bmatrix} 2984.11 & -244.01 \\ -244.01 & 26.78 \end{bmatrix}$
15.108	$\begin{bmatrix} 798.39 & 0 \\ 0 & 2.67 \end{bmatrix}$	$\begin{bmatrix} 3063.51 & -244.12 \\ -244.12 & 27.01 \end{bmatrix}$	$\begin{bmatrix} 3170.14 & -248.45 \\ -248.45 & 27.18 \end{bmatrix}$
20.077	$\begin{bmatrix} 975.70 & 0 \\ 0 & 2.85 \end{bmatrix}$	$\begin{bmatrix} 3295.24 & -249.79 \\ -249.79 & 27.51 \end{bmatrix}$	$\begin{bmatrix} 3385.72 & -253.43 \\ -253.43 & 27.65 \end{bmatrix}$

N_x [kN]	$\mathbf{K}_0$	$\mathbf{K}_0^{ex}$ $k_{s,d}=0$	$\mathbf{K}_0^{ex}$ $k_{s,d}=\infty$
24.749	$\begin{bmatrix} 1142.68 & 0 \\ 0 & 2.47 \end{bmatrix}$	$\begin{bmatrix} 3504.12 & -254.68 \\ -254.68 & 27.95 \end{bmatrix}$	$\begin{bmatrix} 3583.02 & -257.83 \\ -257.83 & 28.08 \end{bmatrix}$
30.385	$\begin{bmatrix} 1133.69 & 0 \\ 0 & 2.41 \end{bmatrix}$	$\begin{bmatrix} 3747.08 & -260.16 \\ -260.16 & 28.47 \end{bmatrix}$	$\begin{bmatrix} 3815.21 & -262.85 \\ -262.85 & 28.58 \end{bmatrix}$
34.871	$\begin{bmatrix} 1485.97 & 0 \\ 0 & 2.48 \end{bmatrix}$	$\begin{bmatrix} 3934.81 & -260.24 \\ -260.24 & 28.87 \end{bmatrix}$	$\begin{bmatrix} 3996.14 & -266.64 \\ -266.64 & 28.96 \end{bmatrix}$
40.181	$\begin{bmatrix} 1662.96 & 0 \\ 0 & 2.49 \end{bmatrix}$	$\begin{bmatrix} 4151.73 & -268.81 \\ -268.81 & 29.32 \end{bmatrix}$	$\begin{bmatrix} 4206.51 & -270.94 \\ -270.94 & 29.40 \end{bmatrix}$
45.696	$\begin{bmatrix} 1843.24 & 0 \\ 0 & 2.60 \end{bmatrix}$	$\begin{bmatrix} 4371.96 & -273.30 \\ -273.30 & 29.78 \end{bmatrix}$	$\begin{bmatrix} 4421.21 & -275.19 \\ -275.19 & 29.85 \end{bmatrix}$
49.771	$\begin{bmatrix} 1971.09 & 0 \\ 0 & 2.47 \end{bmatrix}$	$\begin{bmatrix} 4531.88 & -276.47 \\ -276.47 & 30.10 \end{bmatrix}$	$\begin{bmatrix} 4577.69 & -279.23 \\ -279.23 & 30.17 \end{bmatrix}$

Table 4.5 –Average of experimental end stiffness and exact condensation parameter matrices for each axial load of Test 2

N_x [kN]	$\mathbf{K}_1$	$\mathbf{K}_1^{ex}$ $k_{s,d}=0$	$\mathbf{K}_1^{ex}$ $k_{s,d}=\infty$
4.502	$\begin{bmatrix} 357.46 & 0 \\ 0 & 1.80 \end{bmatrix}$	$\begin{bmatrix} 2550.02 & 230.99 \\ 230.99 & 25.88 \end{bmatrix}$	$\begin{bmatrix} 2721.80 & 238.10 \\ 238.10 & 26.18 \end{bmatrix}$
10.945	$\begin{bmatrix} 599.49 & 0 \\ 0 & 1.59 \end{bmatrix}$	$\begin{bmatrix} 2855.33 & 239.97 \\ 239.97 & 26.61 \end{bmatrix}$	$\begin{bmatrix} 3016.55 & 245.34 \\ 245.34 & 26.83 \end{bmatrix}$
15.108	$\begin{bmatrix} 744.90 & 0 \\ 0 & 1.79 \end{bmatrix}$	$\begin{bmatrix} 3086.97 & 245.07 \\ 245.07 & 27.05 \end{bmatrix}$	$\begin{bmatrix} 3199.95 & 249.66 \\ 249.66 & 27.23 \end{bmatrix}$
20.077	$\begin{bmatrix} 917.35 & 0 \\ 0 & 1.73 \end{bmatrix}$	$\begin{bmatrix} 3316.59 & 250.64 \\ 250.64 & 27.54 \end{bmatrix}$	$\begin{bmatrix} 3412.95 & 254.52 \\ 254.52 & 27.70 \end{bmatrix}$
24.749	$\begin{bmatrix} 1079.65 & 0 \\ 0 & 1.60 \end{bmatrix}$	$\begin{bmatrix} 3253.95 & 255.47 \\ 255.47 & 27.99 \end{bmatrix}$	$\begin{bmatrix} 3608.26 & 258.84 \\ 258.84 & 28.12 \end{bmatrix}$
30.385	$\begin{bmatrix} 1284.21 & 0 \\ 0 & 1.50 \end{bmatrix}$	$\begin{bmatrix} 3765.47 & 260.88 \\ 260.88 & 28.50 \end{bmatrix}$	$\begin{bmatrix} 3838.47 & 263.77 \\ 263.77 & 28.61 \end{bmatrix}$

N_x [kN]	$\mathbf{K}_1$	$\mathbf{K}_1^{ex}$ $k_{s,d} = 0$	$\mathbf{K}_1^{ex}$ $k_{s,d} = \infty$
34.871	$\begin{bmatrix} 1429.29 & 0 \\ 0 & 1.48 \end{bmatrix}$	$\begin{bmatrix} 3952.26 & 264.92 \\ 264.92 & 28.89 \end{bmatrix}$	$\begin{bmatrix} 4018.08 & 267.50 \\ 267.50 & 28.99 \end{bmatrix}$
40.181	$\begin{bmatrix} 1601.82 & 0 \\ 0 & 1.41 \end{bmatrix}$	$\begin{bmatrix} 4168.25 & 269.45 \\ 269.45 & 29.34 \end{bmatrix}$	$\begin{bmatrix} 4227.10 & 271.73 \\ 271.73 & 29.43 \end{bmatrix}$
45.696	$\begin{bmatrix} 1782.99 & 0 \\ 0 & 1.42 \end{bmatrix}$	$\begin{bmatrix} 4387.67 & 273.90 \\ 273.90 & 29.80 \end{bmatrix}$	$\begin{bmatrix} 4440.62 & 275.94 \\ 275.94 & 29.88 \end{bmatrix}$
49.771	$\begin{bmatrix} 1927.37 & 0 \\ 0 & 1.30 \end{bmatrix}$	$\begin{bmatrix} 4547.07 & 277.05 \\ 277.05 & 30.13 \end{bmatrix}$	$\begin{bmatrix} 4596.32 & 278.94 \\ 278.94 & 30.20 \end{bmatrix}$

Table 4.6 –Average of experimental end stiffness and exact condensation parameter matrices for each axial load of Test 2

4.6 Conclusions

An algorithm for axial load identification of beam on elastic supports has been derived. It represents the extension of the procedure for beam on rigid supports, proposed by Tullini and Laudiero (2008), to the more general problem of slender beam. In fact, the algorithm here derived allows to identify the axial force irrespective of boundary conditions and its effective length. The input parameters are a vibration frequency and five components of the corresponding mode shape. Moreover, the algorithm gives an estimation of the diagonal terms of the condensation parameter matrices, which represent the full boundary conditions matrices of the substructure model.

In order to ascertain the accuracy of the analytical procedure, experimental tensile tests configurations have been performed. The elaboration of data analysis showed very good agreement between measured and estimated mean parameters, with an average error of about 2.5%. Hence, the identification accuracy is lower than that observed for the tests for beam on rigid support, which was about 1% (Section 3.2). Nonetheless, the results are very close to each other, giving a highly reliable average value for the axial force.

As for the end stiffness identification, as expected, the experimental results do not match the exact parameters at all. In fact, the method does not give a real estimation of the full condensation parameter matrix, but an estimate of diagonal terms only. Consequently, the experimental results can not be used for any analysis of the end stiffness of the substructure.

References

Amabili M., Carra S., Collini L. Garziera R., Panno A. (2010). Estimation of tensile force in tie-rods using a frequency-based identification method. *Journal of Sound and Vibration*, 329, 2057-2067.

Bahra A.S., Greening P.D. (2009). Identifying axial load patterns using space frame FEMs and measured vibration data. *Mechanical Systems and Signal Processing*, 23, 1282-1297.

Bahra A.S, Greening P.D. (2011). Identifying multiple axial load patterns using measured vibration data. *Journal of Sound and Vibration*, in press

Balmés E. (1997). Structural Dynamics Toolbox. *Scientific Software*.

Bazant Z.P., Cedolin L., (1991). *Stability of Structures. Elastic, Inelastic, Fracture, and Damage Theory*. Oxford University Press, Oxford.

Beconcini M. L. (1996). Un metodo pratico per la determinazione del tiro nelle catene *Costruire in laterizio* 54/96, 299-301.

Bendat J.S. & Piersol. A.G. (1993). *Engineering application of correlation and spectral analysis.* New York; John Wiley & Sons.

Bokaian A. (1988). Natural frequencies of beams under compressive axial loads. *Journal of sound and vibration.* 126(1), 49-65.

Bokaian A. (1990). Natural frequencies of beams under tensile axial loads. *Journal of Sound and Vibration.* 142(3), 481.

Briccoli Bati S., Tonietti U. (2001). Experimental methods for estimating in situ tensile force in tie-rods. *Journal of engineering mechanics*. 1275-1283.

Bronson R., Costa G.B. (2006). *Differential equations, Third Edition*. McGraw Hill.

Bruschi G., Nardoni G., Lanza L., Laudiero F., Tullini N., Mezzadri G., Tralli S. (2004). Experimental stress analysis of historical forged tie beams of archeological museum of Spina in Ferrara, Italy. In Modena, C., Lourenço, P. B. and Roca P. (Eds.), *Proceedings of the Structural Analysis of Historical Construction.* Vol.1, Taylor & Francis, London, 489-497.

Caironi. M., Gambarova P., Tattoni S. (1999). *Teoria e tecnica delle costruzioni.* Ed. Paravia /Scriptorium.

Candela M., Lanza L., Tullini N. Mezzadri G. (2004). Identificazione dello stato di tensione nelle catene storiche a supporto di due interventi di consolidamento di edifici monumentali. *Dalla conoscenza e dalla caratterizzazione dei materiali e degli elementi dell'edilizia storica in muratura ai provvedimenti compatibili di consolidamento.* Workshop at DIS – Politecnico di Milano.

Ceballos M.A., Prato C.A. (2008). Determination of the axial force on stay cables accounting for their bending stiffness and rotational end restraints by free vibration tests. *Journal of Sound and Vibration*, 317, 127-141.

Chen S.-E., Petro S. (2005). Nondestructive bridge cable tension assessment using laser vibrometry. *Experimental Techinques*, March/April, 29-32.

Cheng. F. Y. (2001). *Matrix Analysis of Structural Dynamics*. Marcel Dekker, Inc.

Corradi dell'Acqua L. (1994). *Meccanica delle strutture.* Vol. 3. McGraw Hill.

De Rosa M.A., Franciosi C., Maurizi M.J. (1996). On the dynamic behaviour of slender beams with elastic ends carrying a concentrated mass. *Computers & Structures.* Vol. 58, N. 6, 1145-1159.

Ewins D.J. (1984). *Modal testing: Theory and Practice*. New York: John Wiley & Sons.

Farghaly S.H. (1992). Comments on "The general equation of frequencies for vibrating uniform one-span beams under compressive axial loads". *Journal of Sound and Vibration* (1993) 161(1), 181.

Geier R., De Roeck G., Flesch R. (2006). Accurate cable force determination using ambient vibration measurements. *Structure and Infrastructure Engineering*, Vol. , No.1, 43-52.

Gentile C. (2010). Deflection measurement on vibrating stay cables by non-contact microwave interferometer. *NDT&E International,* 43, 231-240.

Graff K.F. (1975). *Wave Motion in Elastic Solids*, Oxford Univeristy Press.

Greening P.D., Lieven N.A.J. (2003). Identification and updating of loading in framework using dynamic measurement, *Journal of Sound and Vibration*, 260, (1), 101-115.

Guyan J. (1964). Reduction of Stiffness and Mass Matrices. *AIAA Journal*. Vol. 3, NO. 2, 380.

Hassanpour P.A., Cleghorm W.L., Mills J.K. and Esmailzadeh, E. (2007). Exact solution of the oscillatory behaviour under axial force of a beam with a concetraded mass within its interval. *Journal of vibration and control*. 13, 1723-1739.

Hatch M.R. (2001). *Vibration simulation using Matlab and Ansys.* Chapman & Hall/CRC.

Karnovsky I.A., Lebed O.I. (2000). *Formulas for structural dynamics.* McGraw Hill.

Kim B.H., Park T. (2007). Estimation of cable tension force using frequency-based system identification method. *Journal of Sound and Vibration*, 304, 660-676.

Kjell G., Johnson, E. (2009). Measuring axial forces in rail by forced vibrations: experiences from a full –scale laboratory experiments. *Proc. IMechE*, Vol 223 Part F. Rail and Rapid Transit.

Kolousek V. (1973). *Dynamics in engineering structures*. Butterworths London.

Lagomarsino S., Calderini C. (2005). The dynamical identification of the tensile force in ancient tie-rods. *Engineering structures* 27 (6) 846-856.

Leung A.Y.T. (1978). An accurate method of dynamic condensation in structural analysis. *International journal for numerical methods in engineering.* Vol. 12, 1705-1715.

Leung A.Y.T. (1979). An accurate method of dynamic substructuring with simplified computation. *International journal for numerical methods in engineering.* Vol. 14, 1241-1256.

Leung A.Y.T. (1993). *Dynamic Stiffness and Substructures*. Springer – Verlag.

Low. K.H. (1999). Comparison of experimental and numerical frequencies for classical beams carrying a mass in span. *International Journal of Mechanical Science*. 41, 1515-1531

Maurizi M.J. and Bellés P.M. (1991). General equation of frequencies for vibrating uniform one-span beams under compressive axial load. *Journal of sound and* vibration. 145(2), 345 -347.

McConnell K.G. (1995). *Vibrating testing theory and practice.* New York: John Wiley & Sons.

Paz M. (1990). *Structural Dynamics Theory and Computation*, 3rd Edn. Van Nostrand Reinhold, New York.

Piersol A.G., Paez L.T. (2009). *Harri's Shock and Vibration Handbook*. 5th Edn. McGraw Hill.

Reddy J.N. (1997). On locking-free shear deformable beam finite elements. *Computer methods in Applied Mechanics and Engineering.* 149, 113-132.

Reddy J.N. (2002). *Energy principles and variational methods in applied mechanics.* John Wiley & Sons.

Reddy J.N. (2006). *An Introduction to the Finite Element Method.* 3rd Edn. McGraw Hill.

Ren W.X., Liu H.L., Chen G. (2008). Determination of cable tensions based on frequency differences. *Engineering Computation: International Journal for Computer-Aided Engineering and Software.* Vol 25, No.2, 172-189.

Richards T.H., Leung A.Y.T. (1977). An accurate method in structural vibration analysis. *Journal of sound and vibration.* 55(3), 363-376.

Simpson A. (1984). On the solution of $S(\omega)x = 0$ by a Newtonian procedure. *Journal of Sound and Vibration* 97, 153-164.

Sotiropoulos G.H. (1984). Comment on the substructure synthesis method. *Journal of sound and vibration*, 94(1), 150-153.

Tullini N., Laudiero F. (2003) Valutazione dello sforzo normale in travi prismatiche tramite parametri modali flessionali. *Proceeding of AIMETA: Applied Mechanics.*

Tullini N., Laudiero F. (2004). Valutazione sperimentale del tiro nelle catene mediante prove dinamiche. *Proceeding of 11th ANIDIS*, Genova, Italy.

Tullini N., Laudiero F. (2008). Dynamic identification of beam using one flexural mode shape. *Journal of sound and vibration.* 318, 131-147.

Urbano C. (1967). Sulla determinazione del tiro nelle catene degli archi. *Costruzioni metalliche* 5.

Vincenzi L. (2007). Identificazione dinamica delle caratteristiche modali e delle proprietà meccaniche di strutture mediante algoritmi di ottimizzazione. *PhD. Thesis*. DISTART, Università di Bologna, Italy.